NONLINEAR SEISMIC GROUND RESPONSE OF SHALLOW SAND SITES

by

Graeme McAllister

B.A.Sc., The University of British Columbia, 2010

A THESIS SUBMITTED IN PARTIAL FULFILLMENT OF
THE REQUIREMENTS FOR THE DEGREE OF

MASTER OF APPLIED SCIENCE
in
THE FACULTY OF GRADUATE AND POSTDOCTORAL STUDIES
(Civil Engineering)

THE UNIVERSITY OF BRITISH COLUMBIA
(Vancouver)

August 2015

Abstract

Predicting the ground response to the propagation of seismic waves is one of the most important aspects of geotechnical engineering. Advanced soil constitutive models provide significant opportunity to improve the understanding of nonlinear ground response during a seismic event, and offer the capability of simulating complex nonlinear soil behaviour which is not captured by means of traditional ground response analyses in geotechnical engineering. Moreover, observations of distinctive nonlinear soil behaviour during recent large earthquake events such as the 2011 Tohoku earthquake point towards the need to more reliably simulate realistic soil behaviour in order to understand the complex dynamic response of soils.

The intent of this thesis is to utilize the SANISAND bounding surface plasticity model based on the work of Dafalias and Manzari (2004) to simulate the response of shallow sand deposits to a number of earthquake motions, with the aim of evaluating the ability of the model to simulate relatively complex nonlinear soil behaviour. Furthermore, both total and effective stress analysis techniques are carried out in order to highlight the importance of modeling the interaction between the pore fluid phase and the soil solid. For this purpose, two sites are analyzed, including a case history of a real downhole seismograph array and a generic site. The capability of the SANISAND model to simulate the phenomenon of high frequency dilation pulses is also explored.

The SANISAND constitutive model is shown to adequately simulate the seismic ground response of a shallow sand soil column at a real downhole seismic array in Sendai, Japan by comparison to surface seismograph recordings for several earthquake events on the east coast of Japan. Soil permeability in the effective stress analyses is influential in the dynamic response of the soil to earthquake motions. Furthermore, modeling the pore fluid – soil solid interaction in an effective stress analysis is shown to be important for shallow medium dense sand sites subjected to cyclic mobility and strain stiffening. High frequency ground motion during the seismic response of a generic 10 m deep sand site is suggested to be caused by acceleration pulses as a result of soil dilation.

Preface

This thesis describes research carried out at the University of British Columbia between January 2014 and August 2015. Dr. Mahdi Taiebat was the supervisor for this research and all analytical work and numerical analyses were completed under his review. Chapter 3 and 4 of this thesis were developed in part based on the University of British Columbia's involvement with the PRENOLIN Project, an international collaboration studying nonlinear ground response analysis. The numerical codes for carrying out the analyses completed were developed in collaboration with Dr. Pedro Arduino and Alborz Ghofrani of the University of Washington.

I was the primary contributor to the development of the concept of this thesis, and was responsible for preparing all six chapters, including the presented data and analyses. A version of Chapter 5 of this thesis has been accepted for publication: McAllister, G., Taiebat, T., Arduino, P., Ghofrani, A., and Chen, L. (2015). "Nonlinear Site Response Analyses and High Frequency Dilation Pulses", Proceedings of the 68th Canadian Geotechnical Conference, September 20-23, 2015, Quebec City, Quebec, Manuscript Number: PAP447, 8 pages. I developed the paper concept, carried out all the numerical analyses and wrote the first draft of the paper. Dr. Mahdi Taiebat, Dr. Pedro Arduino and Alborz Ghofrani made revisions to the manuscript.

Table of Contents

List of Tables

List of Figures

Acknowledgements

The research work presented in this thesis was made possible by the efforts of a number of individuals. I extend my sincerest thanks and appreciation to all of those who have contributed in some way to making this research possible.

First, I extend my sincerest gratitude to my supervisor Dr. Mahdi Taiebat who has provided tireless support and guidance in carrying out this research. His proficiency and enthusiasm for the area of geotechnical earthquake engineering were the inspiration for me to explore the topic of ground response analysis. The success of this research is largely a result of the time and effort he has contributed to this work. Thanks also go to Dr. John Howie for his thoughtful suggestions and insight regarding the topic of small strain shear modulus.

My sincere thanks are extended to Dr. Pedro Arduino, Alborz Ghofrani and Long Chen at the University of Washington, whose technical knowledge has greatly contributed to this work.

Financial support which made this research possible was provided by the Natural Science and Engineering Research Council of Canada (NSERC) and Levelton Consultants Ltd. Particular thanks go to Doug Wallis at Levelton Consultants for his ongoing support and technical input, as well as to Randy Hillaby and Kenny Ko for their support in completing this work.

Last and most importantly, special thanks are owed to my wife Aimee. Without her patience and support none of this would have been possible.

Chapter 1: Introduction

The term ground response analysis is a general expression which in part refers to the task of predicting seismic ground motions and evaluating the dynamic stresses and strains which develop over the depth of a site (Kramer, 1996). Ground response analyses of a seismic event are one of the most important and most challenging tasks in geotechnical engineering. The difficulty begins with adequately characterizing the subsurface geometry and conditions of a site, and continues through to laboratory testing methods and analytical techniques. There is no end to the complexity that the geotechnical engineer may consider, depending on the requirements of the project at hand.

Given the tremendous difficulty in developing a model which captures all of the different aspects of a real site subjected to earthquake motions, it has been out of necessity that geotechnical engineers have developed simplified techniques which have been shown to provide adequate estimates of how the ground will respond when subjected to seismic motion. One of the most commonly used simplified methods of carrying out ground response analyses is the equivalent-linear method first developed in the program SHAKE (Schnabel et al., 1972). However, with the advent of high-performance computational platforms, advanced soil constitutive models, which provide more realistic representation of soil behavior, have become more widely available in the recent years. One such advanced soil constitutive model for the representation of the nonlinear behaviour of sand soil is the two-surface plasticity model originally developed by Manzari and Dafalias (1997). Extensions of the Manzari and Dafalias (1997) model were developed by Dafalias and Manzari (2004), Dafalias et al. (2004), Taiebat and Dafalias (2008) and Li and Dafalias (2012), and are collectively named SANISAND models.

The objective of this thesis is to utilize the SANISAND bounding surface constitutive model based on the work of Dafalias and Manzari (2004) recently implemented in the finite element program OpenSees (McKenna and Fenves, 2001), for the purpose of evaluating the ability of the model to reliably simulate the response of relatively shallow sand sites to seismic ground motions. To this end, this work will analyze both a real site downhole array in Sendai, Japan

– which is part of a strong-motion observation network operated by the Port and Airport Research Institute of Japan, and a generic site with an assumed soil profile.

Specifically, the important objectives of this thesis include the following:

- Perform SANISAND model calibration based on conventional laboratory tests and in situ field measurements and identify key considerations for model calibration.
- Explore the analytical procedures for carrying out a ground response analyses with the SANISAND model in OpenSees, highlighting the important analysis considerations and protocols for future users of the model.
- Analyze the ability of SANISAND model to reproduce a case history developed based on a conventional geotechnical investigation.
- Carry out analyses using both total and effective stress techniques and compare the relative difference between the techniques. In doing so, highlight the importance of adequately modeling the interaction between the pore fluid and soil solid.
- Investigate the capability of the SANISAND model to simulate complex soil behaviour during seismic motion, including high frequency dilation pulses.

This thesis is presented beginning with a review in Chapter 2 of how soil behaviour has conventionally been modeled in ground response analyses. Chapter 2 also includes a section describing the SANISAND model of Dafalias and Manzari (2004). Chapter 3 describes the numerical platform, continuum model and analysis procedures used for the ground response analyses presented in this thesis. The Sendai downhole array case study is presented in Chapter 4 and includes detailed description of the SANISAND model calibration, along with the results of the ground response simulations compared to the motions recorded at the site seismographs. Further evaluation of the SANISAND model and its capability to simulate complex soil behaviour such as soil dilation during seismic motion is presented in Chapter 5. Finally, Chapter 6 presents the conclusions of this thesis along with recommendations for future work.

Chapter 2: Modeling Soil Behaviour in Seismic Ground Response Analyses

2.1 Introduction

A completely comprehensive seismic ground response analysis would model all aspects of seismic propagation, including earthquake fault rupture, the propagation of seismic waves from the source to the site in question, and the response of the soil and rock to the propagation of seismic waves through the site and up to the ground surface (Kramer, 1996). However, such a model is beyond the reality of engineering practice. Consequently, seismic ground response analyses tend focus on the propagation of seismic waves up from the bedrock, through the site soils and to the ground surface.

As the seismic ground motions move through a site, they will be influenced by the local soil conditions. Soils can change the frequency content of seismic motion, amplify or attenuate the motion, and also change the duration of the motion. Moreover, the site stratigraphy and layering can complicate the propagation of the seismic waves.

A number of techniques have been proposed to carry seismic ground response analyses in order to approximate the nonlinear hysteretic stress-strain response of soil during earthquake loading. These analyses may be in one-, two-, or three-dimensional space and are further categorized according to the how the nonlinear behaviour of the soil is characterized, and whether or not the interaction of the soil-solid and pore water is considered.

Geotechnical engineering practice has developed three broad classes of soil models to represent cyclic soil behaviour: equivalent linear models, cyclic nonlinear models and advanced constitutive models (Kramer, 1996). Depending on the problem at hand, each of these three models may represent a useful characterization of soil behaviour for many practical problems. However, it is important to understand that each model is only a simplification of reality. Nonetheless, with an appreciation of the origin and applicability of the model, the user can manage the model uncertainty with engineering judgment and evaluate whether or not the model is useful for the problem (Muir Wood, 2000).

This chapter endeavors to briefly describe the methods and procedures used for seismic ground response analyses in geotechnical engineering practice, and in doing so attempts to provide some general insight into the geotechnical models used for this purpose. Following a general description of nonlinear soil behaviour, the equivalent linear and advanced constitutive models for describing soil behaviour are presented in the following sections.

2.2 Simplified General Nonlinear Soil Behaviour

General nonlinear soil behaviour involves multi-directional shearing and rotating principal stresses in three-dimensions (Yamazaki et al., 1985). Three-dimensional soil behaviour considers multi-direction loading and initial shear stress applied to the soil, which in turn effects the nonlinear soil behaviour. A discussion on multi-directional nonlinear soil behaviour is beyond the scope of this thesis. In this section, a brief overview of the simplified methods conventionally used in geotechnical engineering practice to characterize general nonlinear behaviour is presented. Simplified nonlinear soil behaviour is presented in the context of shear modulus and damping ratio – two parameters that have received much attention in the field of geotechnical earthquake engineering.

2.2.1 Secant and Tangent Shear Moduli

Soil strain in response to the application of stress is known to be highly nonlinear. As such, a single value does not describe the stiffness behaviour of soil, but rather, soil stiffness is a function of strain. The typical cyclic shear stress-strain response of an element of soil is a hysteresis loop which illustrates the reduction of soil stiffness with strain (Ishihara, 1996). Soil stiffness is defined here as the ratio of the change in shear stress with strain, and can be quantified as either the tangent shear modulus, G_{tan}, or secant shear modulus, G_{sec}. The tangent and secant shear moduli, and their relation to a hysteretic stress-strain loop for soil is illustrated in Figure 2-1.

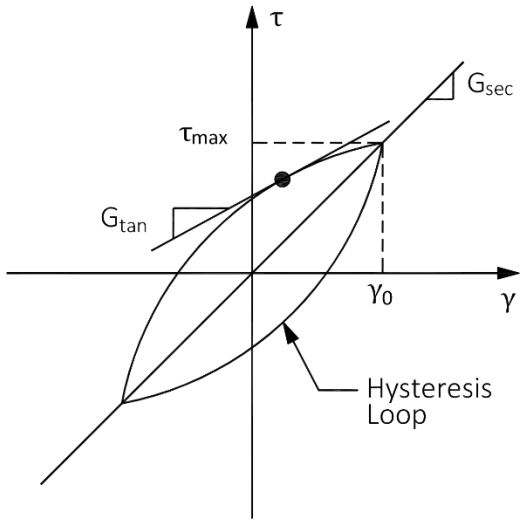

Figure 2-1: Typical hysteresis stress-strain response of soil

As shown in Figure 2-1, the tangent slope of the hysteresis loop at a point defines the tangent shear modulus, while the average shear modulus of the entire loop is the secant shear modulus, as given in the following equations,

$$G_{tan} = \frac{d\tau}{d\gamma} \tag{2.1}$$

$$G_{sec} = \frac{\gamma_0}{\tau_{max}} \tag{2.2}$$

where τ and γ are the shear stress and strain at any point on the hysteresis curve, respectively, and γ_0 is the shear strain amplitude of the hysteresis loop corresponding to the shear stress amplitude, τ_{max}.

The shear modulus at very small shear strain, where the soil behavior is nearly linear, defines the maximum shear modulus, G_{max}.

2.2.2 Shear Modulus Reduction

An increase in cyclic shear strain amplitude results in a corresponding reduction of a soil element's secant shear modulus. Accordingly, at small strain, the secant modulus is highest and decreases with increasing cyclic shear strain amplitude. This decrease in secant shear modulus with strain amplitude can be described by a backbone curve, which is a line that connects a set of hysteresis curves corresponding to different levels of shear strain or shear stress and a certain number of loading cycles. The backbone curve has its origin at zero strain and connects the loci of maximum shear strain and stress corresponding to each hysteresis curve in the set. A typical backbone curve is illustrated in Figure 2-2.

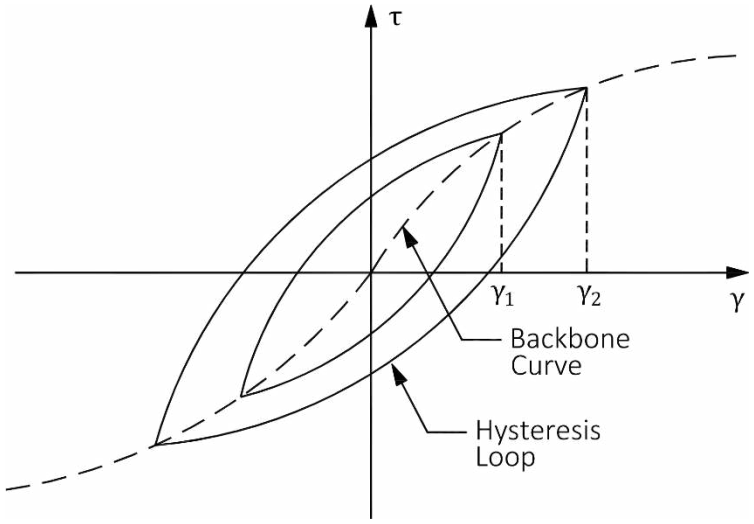

Figure 2-2: Backbone curve representing the decrease in secant modulus with shear strain

The shape of the backbone curve describes the reduction of soil stiffness with repetitive loading and is specific to the number of cycles being considered. For example, the backbone curve that is developed from a cyclic triaxial test which is run for ten different levels of shear stress may correspond to the secant shear modulus determined for the fifth cycle of loading for each level of stress. Accordingly, the hysteresis loops shown in Figure 2-2 would be developed from the fifth load cycle, and γ_1 and γ_2 would be the maximum shear strain of the fifth cycle of consecutive load stages.

It is common in geotechnical earthquake engineering practice to represent the decrease of secant shear modulus with shear strain as a shear modulus reduction curve, which is the ratio of secant and maximum shear modulus G_{sec}/G_{max} plotted against shear strain. To be consistent with conventional geotechnical engineering practice, the secant term can be dropped and the shear modulus reduction curve is designated simply as G/G_{max}.

To develop a shear modulus reduction curve it is necessary to have information about the soil maximum shear modulus and how the ratio G/G_{max} varies with cyclic shear strain and other parameters; including void ratio, mean principal effective stress, plasticity index, overconsolidation ratio, and number of loading cycles (Kramer, 1996). A typical shear modulus reduction curve is presented in Figure 2-3.

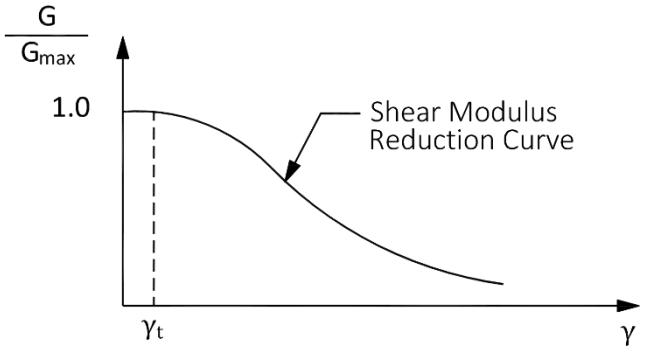

Figure 2-3: Typical shear modulus reduction curve for soil

As illustrated in Figure 2-3, the shear modulus reduction curve decreases from a maximum value of 1.0 to values less than 1.0 with increasing shear strain. Strain along the plateau of the curve before a threshold shear strain γ_t where the ratio of G/G_{max} drops below 1.0 can be classified as being in the "very small strain" region (Atkinson, 2000). The threshold strain may occur near $1.0 \times 10^{-4}\%$; after which, the modulus reduction curve enters the "small strain" region, which covers shear strains between the threshold strain and 0.1%. "Large strains" occur at shear strains greater than 0.1% (Atkinson, 2000).

Considering that the maximum shear modulus corresponds to shear strain values approximately less than $1.0 \times 10^{-4}\%$, and that the small strain properties of soil are very sensitive to disturbance during sampling for laboratory tests, it is best to determine G_{max} by

measuring the in situ shear wave velocity V_s using geophysical techniques. In geotechnical engineering practice it is common to measure the down-hole soil V_s while advancing a seismic cone penetration test (SCPT) by inducing shear strains less than 1.0 x 10^{-4}% (Howie and Campanella, 2005). Based on the theory of wave propagation through an elastic medium, the maximum shear modulus can then be determined using the following equation,

$$G_{max} = \rho V_s^2 \quad \textbf{(2.3)}$$

where ρ is the total mass density of the soil.

2.2.3 Damping Ratio

The area encompassed by a stress-strain hysteresis loop is related to the dissipation of energy during a single loop. This dissipation of energy can be described by the damping ratio ξ. Damping is smallest at small strains and, similar to the secant shear modulus, the damping ratio is a function of shear strain amplitude, increasing above the threshold strain γ_t with strain amplitude, as shown in Figure 2-4.

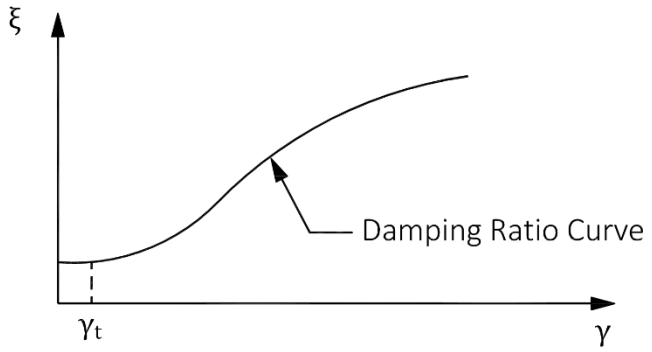

Figure 2-4: Typical damping ratio curve

The increase in damping ratio with increasing strain is exhibited as an increase in the breadth of the hysteresis loops during cyclic loading (Kramer, 1996). For a given hysteresis loop, the damping ratio can be calculated using the following equation,

$$\xi = \frac{\Delta W_{cyc}}{4\pi W_s} \tag{2.4}$$

where ΔW_{cyc} is the energy dissipated in a single hysteresis loop and W_s is the cycle maximum strain energy given by the following equation,

$$Ws = \frac{1}{2} G_{sec} \gamma_0^2 \tag{2.5}$$

Figure 2-5 presents the estimation of damping ratio during cyclic loading as described above.

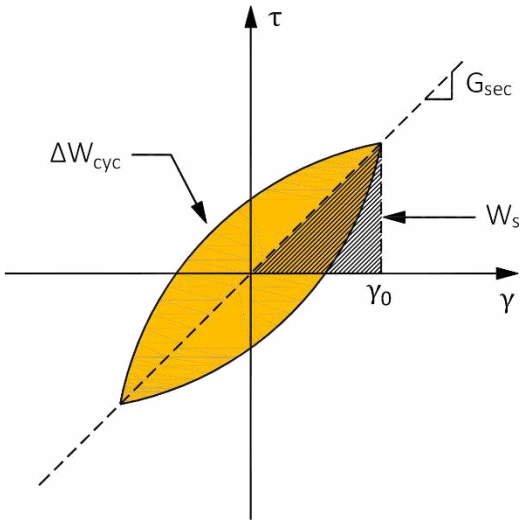

Figure 2-5: Damping ratio during cyclic loading

2.3 Models of Nonlinear Soil Behaviour

A brief description of equivalent linear and advanced constitutive models to represent the nonlinear behavior of soil is presented in the following sections. The equivalent linear model is discussed as it is frequently used to complete seismic ground response analyses in geotechnical engineering practice; however, the equivalent linear model is not the focus of the research herein.

2.3.1 Equivalent Linear Model

The equivalent linear soil model treats the soil as a linear viscoelastic material and establishes the dynamic strain-dependent secant shear modulus and damping ratio to approximate nonlinear soil behaviour during an earthquake. This is accomplished through an iterative process where the shear modulus and damping ratio of the soil are updated to correspond to the level of strain induced in each soil layer (Bardet et al., 2000). This model was first developed in the computer program SHAKE (Schnabel et al., 1972), which remains to be one of the most commonly used methods of conducting seismic ground response analyses.

To determine the dynamic properties of the soil deposit using the equivalent linear procedure, it is common in geotechnical engineering practice to establish the shear modulus and damping ratio within each soil layer with empirical G/G_{max} and damping ratio curves for a given soil type. Empirical relations to represent the curve of G/G_{max} and damping ratio against shear strain have been developed for a number of soil types (Hardin and Drnevich, 1970; Seed and Idriss, 1970; Darendeli, 2001).

As an alternative to using empirical relations of G/G_{max} and damping ratio, an investigation and laboratory testing program can be performed to establish site-specific shear modulus and damping curves for the site. A site-specific set of shear modulus and damping curves may be important for cases where no empirical relation has been established for the soil to be modeled.

It is important to note that because equivalent linear models treat the soil as a linear viscoelastic material, the results obtained from such methods cannot be used for problems involving permanent strain or failure (Kramer, 1996). For strains over approximately 0.5%, soil nonlinearity will govern the ground response and the equivalent linear method will cease to be appropriate for capturing the seismic ground response.

2.3.2 Advanced Constitutive Models

Advanced constitutive soil models use the principles of plasticity to describe general soil behavior and how strain will occur in response to a given stress increment. In general, constitutive models require a yield surface, hardening law and flow rule. The yield surface

defines the limits of elastic soil behavior and the hardening surface describes how the yield surface will change once plastic strain occurs (Kramer, 1996). The flow rule describes how the plastic strains will evolve with deformation. The advanced constitutive model used for the research presented herein is a version of SANISAND constitutive model developed by Dafalias and Manzari (2004). This model falls within the class of effective stress soil constitutive models and characterizes the response of sand soils to cyclic loading, including both cyclic mobility and liquefaction. Further description of the SANISAND model is provided in Section 2.3.3.

2.3.3 The SANISAND Model

SANISAND is the name for a class of Simple ANIsotropic SAND constitutive models extended from the original two-surface plasticity model developed by Manazari and Dafalias (1997). The SANISAND class includes the models developed by the work Dafalias and Manzari (2004), Dafalias et al. (2004), Taiebat and Dafalias (2008) and Li and Dafalias (2012). The work by Manzari and Dafalias (1997) represents the core of the constitutive model and the above-referenced subsequent works build into the model different constitutive features which can be added to the original model framework. The work of Dafalias and Manzari (2004) used to model soil behavior in this thesis accounted for fabric change effects of the soil under dilation which were not initially included in the model formulation of Manzari and Dafalias (1997).

The SANISAND model is based on the concept of a two-surface plasticity formulation, which includes both yield and bounding surfaces, in addition to the state parameter proposed by Been and Jefferies (1985). The state parameter incorporates into the model the framework of Critical State Soil Mechanics (Manazari and Dafalias, 1997).

The model constitutive formulation is presented in detail in both triaxial and multiaxial spaces in Manzari and Dafalias (1997) and Dafalias and Manzari (2004). A brief review of the general constitutive formulation is presented in triaxial space in the section below; however, the constitutive formulation is fully compatible with multiaxial space. Calibration of the model

parameters in triaxial space leads to the correct multiaxial implementation (Dafalias and Manzari, 2004).

2.3.3.1.1 Basic Model Concepts

The framework of Critical State Soil Mechanics and stress ratio η form the basis of the two-surface model developed by Manazari and Dafalias (1997), and the subsequently extended SANISAND class of models. Stress ratio is defined as following relation,

$$\eta = \frac{p}{q} \tag{2.6}$$

where p and q are the mean effective stress and deviatoric stress, respectively, given by the following equation in triaxial stress space,

$$p = \frac{\sigma_1 + 2\sigma_3}{3} \tag{2.7}$$

$$q = \sigma_1 - \sigma_3 \tag{2.8}$$

where σ_1 and σ_3 are the major and minor principal stress quantities in triaxial space.

The strain quantities are also the standard triaxial quantities described by the following equations,

$$\varepsilon_v = \varepsilon_1 + 2\varepsilon_3 \tag{2.9}$$

$$\varepsilon_q = \frac{2(\varepsilon_1 - \varepsilon_3)}{3} \tag{2.10}$$

where ε_v and ε_q are the volumetric and deviatoric strain, and ε_1 and ε_3 are the major and minor principal strain quantities in triaxial space, respectively. Herein, the subscripts v and q represent the volumetric and deviatoric parts of strain.

It should be noted that in triaxial stress space that $\sigma_2 = \sigma_3$ and $\varepsilon_2 = \varepsilon_3$. In this thesis, the stress components are considered to be effective unless otherwise noted, and the stress and strain components are positive in compression.

2.3.3.1.2 Yield Surface

The yield surface bounds the region wherein stress ratio increments induce only elastic strain and is represented by the following expression,

$$f = |\eta - \alpha| - m = 0 \tag{2.11}$$

where α is the slope of the line bisecting the wedge-shaped yield surface in triaxial p-q space and m defines the opening of the wedge as 2mp. The yield surface is shown in Figure 2-6.

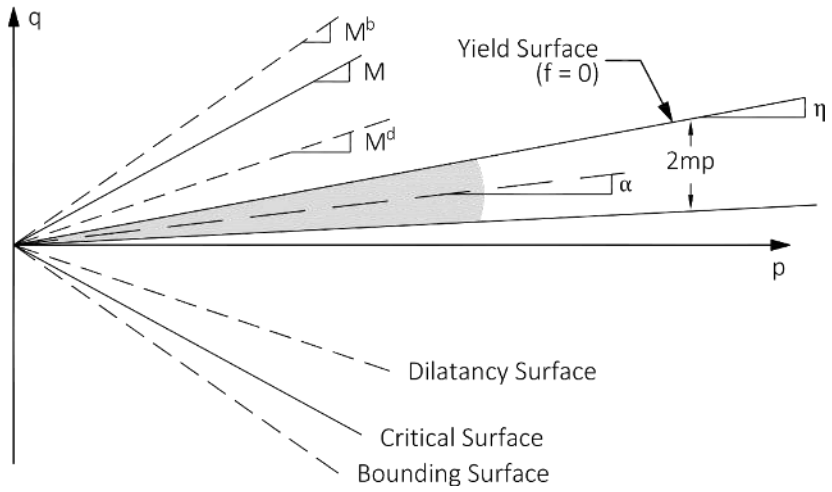

Figure 2-6: SANISAND model schematic in triaxial p-q space (adapted from Dafalias and Manzari, 2004)

No plastic deformation will occur if the mean and deviatoric stress increase at a constant η, as the stress path will not intersect the elastic yield surface (Manzari and Dafalias, 1997). If η satisfies Equation (2.11) such that f = 0, $\dot{\eta}$ points outward from the yield surface and plastic deformation occurs. To maintain f = 0 while η is on yield surface, α changes (the yield surface rotates) and m (the size of the yield surface) may also change. A change in α, or rotation of the yield surface, corresponds to kinematic hardening whereas a change in m, or widening of the yield surface, is isotropic hardening.

2.3.3.1.3 Critical State Soil Mechanics in SANISAND

The critical state is defined as the stress ratio at which soil deformation continues with zero volumetric strain rate (Schofield and Wroth, 1968). The stress ratio at critical state is defined as $M = q_c/p_c$, where q_c and p_c are the deviatoric and mean effective stress at critical state, respectively. The stress ratio M is shown as a solid line in triaxial p-q space in Figure 2-6.

At critical state, the critical state void ratio e_c is attained and is defined by the following power relation based on the findings of Li and Wang (1998),

$$e_c = e_0 - \lambda_c \left(p_c / p_{at}\right)^{\xi} \quad \textbf{(2.12)}$$

where e_0 is the void ratio at $p_c = 0$, λ_c is the slope of the critical state line, p_{at} is atmospheric pressure, and ξ is a constant. The constant ξ may be assumed to be 0.7 for sands (Li and Wang, 2008).

The state parameter ψ introduced by Been and Jefferies (1985) defines the distance between the critical state void ratio and the current void ratio e, and is given by the following relation,

$$\psi = e - e_c \quad \textbf{(2.13)}$$

2.3.3.1.4 Dilatancy and Bounding Surfaces

The volumetric response of sands will be either dilative or contractive, depending on the stress ratio and whether ψ is positive or negative (i.e. the soil is dense of critical or loose of critical). A dilatancy surface represented by the dashed line M^d in Figure 2-6 is used in the SANISAND model to control the volumetric response of soil. For $\eta < M^d$, the soil response is contractive, and for $\eta > M^d$ the soil response is dilative. The dilatancy surface is equivalent to the phase transformation line proposed by Ishihara (1975).

The slope of M^d is variable and approaches critical stress ratio M as the current void ratio approaches e_c. If M^d were to remain constant, unlimited dilation would occur when the stress

ratio of dilative soils reach M, which is not realistic (Manzari and Dafalias, 1997). The state parameter ψ relates the dilatancy surface to the critical state stress ratio M by the following equation,

$$M^d = M \exp(\eta^d \psi) \tag{2.14}$$

where n^d is a positive material constant.

Sands may soften prior to reaching critical stress ratio. For example, a sand which is dense of critical and subjected to a drained constant-p triaxial compression tests will first consolidated and then dilate to critical state. The dilation is associated with a softening response which is accounted for in the SANISAND model by the peak stress ratio shown as the bounding surface M^b in Figure 2-6. Similar to the dilatancy surface, the bounding surface will approach the critical stress ratio M as the current void ratio approaches e_c. The bounding surface is related to the critical stress ratio with the state parameter ψ by the following relation,

$$M^b = M \exp(-\eta^b \psi) \tag{2.15}$$

where n^b is a positive material constant.

Following the logic of Equation (2.15) and (2.16), for $\psi < 0$: $M^d < M < M^b$; for $\psi > 0$: $M^b < M < M^d$, and $M^b = M = M^d$ when $\psi = 0$ (Dafalias and Manzari, 2004). This means that M^d and M^b will approach M as ψ approaches zero, and will overlie M at critical state.

2.3.3.1.5 Stress-Strain Relations

The SANISAND model decomposes the rate of total strain into its elastic and plastic strain rates, and rate of total strain can be expressed as,

$$\dot{\varepsilon} = \dot{\varepsilon}^e + \dot{\varepsilon}^p \tag{2.16}$$

where ε represents the strain tensor and the superscripts e and p denote the elastic and plastic parts of the strain rate, respectively. The superposed dot denotes the rate or time derivative.

The SANISAND model elastic and plastic rates of strains are represented by the following relations,

$$\dot{\varepsilon}_q^e = \frac{\dot{q}}{3G} \qquad \dot{\varepsilon}_v^e = \frac{\dot{p}}{K} \tag{2.17}$$

$$\dot{\varepsilon}_q^p = \frac{\dot{\eta}}{H} \qquad \dot{\varepsilon}_v^p = d\left|\dot{\varepsilon}_q^p\right| \tag{2.18}$$

where G and K are the incremental elastic shear and bulk moduli, respectively; H is the plastic hardening modulus; and *d* is the dilatancy parameter after Rowe's dilatancy theory (Rowe, 1962).

Based on the work of Richart et al. (1970) and Li and Dafalias (2000), the mean effective stress and current void ratio e determine the incremental G, which can be expressed as,

$$G = G_0 p_{at} \frac{(2.97 - e)^2}{1 + e} \left(\frac{p}{p_{at}}\right)^{1/2} \tag{2.19}$$

where G_0 is a constant and p_{at} is the atmospheric pressure for normalization. The incremental K is determined using the conventional elastic relation,

$$K = \frac{2(1 + \nu)}{3(1 - 2\nu)} G \tag{2.20}$$

where ν is the Poisson's ratio. The Poisson's ratio represents the response in the very small pure elastic range of the model. Beyond this range the response is governed by the combined elastic and plastic parts. Because of this, the elastic Poisson's ratio presented in this class of model may not take on typical Poisson's ratio values for sands, but rather has been shown to be in the order of ν = 0.05 for Toyoura and Nevada sand (Taiebat et al., 2010). However, a

larger Poisson's ratio should be applied when establishing the in situ static self-weight and elastic stiffness of the soil column using purely an elastic response. After simulation of the representative in situ stress has reached equilibrium, the elasto-plastic response of the model can be initialized.

2.3.3.1.6 Plastic Modulus

The plastic hardening modulus H is defined by the distance between M^b and η, and controls the rate of deviatoric plastic strain based on Equation (2.18). In triaxial p-q space H is defined by the following relation,

$$H = h(M^b - \eta) \tag{2.21}$$

where h is a positive function of the state variables, given by the expressions,

$$h = \frac{b_0}{|\eta - \eta_{in}|} \qquad b_0 = G_0 h_0 (1 - c_h e) \left(\frac{p}{p_{at}}\right)^{-1/2} \tag{2.22}$$

where h_0 and c_h are scalar parameters, and η_{in} is the initial stress ratio when loading commences.

2.3.3.1.7 Dilatancy

The dilatancy parameter *d* in Equation (2.18) is controlled by the distance between the current stress ratio and the dilatancy surface M^d as shown in the following relation,

$$d = A_d(M^d - \eta) \tag{2.23}$$

where A_d is a function of the state variables and is given by the following equation,

$$A_d = A_0(1 + \langle sz \rangle) \tag{2.24}$$

where A_0 is a constant, s = ± 1 depending on whether η = α + m (top of the yield surface) or η = α − m (bottom of the yield surface) and z is the fabric-dilatancy internal variable, which changes as described in the following relation,

$$\dot{z} = -c_z\langle -\dot{\varepsilon}_v^p \rangle (s z_{max} + z) \tag{2.25}$$

The MacCauley brackets ⟨ ⟩ are defined such that ⟨x⟩ = x if x > 0 and ⟨x⟩ = 0 if x ≤ 0.

The fabric-dilatancy variable z was incorporated into the SANISAND model by Dafalias and Manzari (2004) and was not included in the original description of the model in Manzari and Dafalias (1997). The fabric-dilatancy parameter *z* was included to overcome early stabilization of undrained stress path loops during cyclic loading using the model of Manzari and Dafalias (1997). The z parameter avoids this early stabilization problem and allows for continued cyclic undrained loading to lead to very low mean effective pressure p, which causes liquefaction and is an important consideration when modeling the ground response to earthquakes (Dafalias and Manzari, 2004).

The parameters c_z and z_{max} are empirical and need to be determined on a trial basis during calibration to laboratory data.

2.4 Seismic Ground Response Analysis Using the Finite Element Method

Seismic ground response analyses are often carried out as one-dimensional soil columns in geotechnical engineering practice. However, one-dimensional models are only representative of only a limited number of real situations. A typical one-dimensional seismic ground response analysis includes a soil column with level ground and parallel stratigraphic boundaries subjected to an input motion applied horizontally in one direction at the base of the column. For more complex site geometries, two- and three-dimensional seismic ground response analyses can be completed. Two- and three-dimensional analyses have the advantage of more realistically simulating site geometries which include sloping sites or dipping subsurface soil and bedrock layers. Two- and three-dimensional analyses can also incorporate volumetric soil

response and more than one direction of earthquake input motion, including horizontal and vertical motion, a technique which may more realistically simulate an earthquake event.

The continuum model which represents the site to be studied during a seismic ground response analysis can be defined by an assemblage of finite elements. Finite elements characterize seismic ground response by the response at the nodal points of the elements. The material behaviour of a finite element can be defined by an advanced constitutive model. Finite elements can represent one-, two-, or three-dimensional site conditions.

Finite element formulations can represent soil conditions as a single-phase medium, such as a soil mass where the response of pore water is ignored during analysis, or as a two-phase medium, such as a saturated soil-skeleton where the interaction between the pore water and soil-skeleton is modeled. Simulation of a soil mass where the interaction of the pore water and soil-skeleton is not considered can be referred to as a total stress analysis, whereas an analysis which considers the interaction between the pore water and soil-skeleton can be referred to as an effective stress analysis.

Biot (1941) first proposed equations describing the interaction of pore fluid and soil. This work and subsequent extensions (Biot, 1956; Biot, 1962) formed the basis of alternative formulations for simulation of transient dynamic soil-pore water interaction developed by Zienkiewicz and Shiomi (1984), who proposed three general approaches including u-p, u-U and u-p-U, where u is solid displacement, p is pore pressure and U is fluid displacement.

Seismic ground response analyses using a finite element continuum with material behaviour defined by a constitutive model are commonly completed by integrating the equations of motion using direct numerical integration in the time domain. Using numerical integration, the soil stress-strain relation for each time step are determined by the constitutive model and nonlinear soil behaviour is established by carrying out the analyses over a series of small incremental steps (Kramer, 1996).

Chapter 3: Numerical Model for Seismic Ground Response Analyses within OpenSees

3.1 Introduction

This chapter describes the numerical continuum model utilized to complete the seismic ground response analyses for a real site downhole array in Sendai, Japan presented in Chapter 4, and a generic site with an assumed soil profile presented in Chapter 5. The continuum model was developed and analyses were completed within the finite element numerical platform OpenSees (Open System for Earthquake Engineering Simulation) developed by McKenna and Fenves (2001). Further description of the continuum model within the OpenSees numerical platform is provided herein.

3.2 OpenSees Numerical Platform

The OpenSees finite element program is open-source software which contains a large number of independent libraries of elements, constitutive models, solution algorithms, equation solvers and integrators. OpenSees is an object-oriented framework and includes a set of modules which create the finite element domain, specify analysis procedures, monitor quantities during analysis, and provide the results (Mazzoni et. al. 2007). Using the programming language Tcl the user builds up the different components of the numerical model, including the model dimensions and configuration, element type, constitutive material behaviour, boundary conditions, loading pattern and equation solvers.

3.3 General Description of the Continuum Models

The seismic ground response analyses completed for this research consider one-dimensional total and effective stress model configurations. The analyses all consider a shallow surficial layer of sand overlying bedrock. The seismic ground response models were adapted from examples of total and effective stress ground response analyses prepared by McGann and Arduino (2011a) and McGann and Arduino (2011b), available as open-source files on the OpenSees website (opensees.berkeley.edu).

The effective and total stress analyses were completed using the same model dimensions, configuration, constitutive material, loading pattern and equation solver. Boundary conditions applied to the two models were also the same for the displacement degrees-of-freedom, as further discussed in Section 3.5. Different element types were used in the total and effective stress analyses, as well as different mass densities for establishing the in situ at rest stress conditions, as discussed in Section 3.4 and 3.8, respectively.

The in situ stress conditions prior to the onset of earthquake motion in the effective stress analyses were established using a body force in the vertical direction based on the total mass density and porewater pressures developed from the location of the water table. As there is no water table in the total stress analyses, the in situ stress conditions prior to the onset of earthquake motion were established by using a body force in the vertical direction based on the submerged soil mass density below the water table. This way, the total and effective stress analyses simulate the same in situ stress conditions prior to the onset of earthquake loading. The effective and total stress analyses both use the total mass density of the soil material as an input parameter to the SANISAND model for the simulation of the dynamic response of the soil column.

Additional description of the total and effective stress seismic ground response models is provided in the sections that follow.

3.4 Geometry of Model and Soil Elements

The maximum element size for numerical seismic ground response analyses can be determined based on the concept that a shear wave propagating through the soil should be well resolved for a minimum wavelength in order to capture the important effects of the input motion. To achieve this, a minimum number of elements are required over one wavelength propagating at the maximum frequency which is to be well-resolved in the seismic ground response analyses, called the cutoff frequency f_{max}. The minimum wavelength which is to be well-resolved λ_{min} can be determined using the relation,

$$\lambda_{min} = \frac{V_{s-min}}{f_{max}} \quad \textbf{(3.1)}$$

where $V_{s\text{-}min}$ is the minimum shear wave velocity of the soil profile.

The maximum element size in the numerical analysis is established using the following equation,

$$\Delta_y = \frac{\lambda_{min}}{n_{min}} \quad \textbf{(3.2)}$$

where Δ_y is the element size in the vertical direction, and n_{min} is the minimum number of elements required to define the minimum wavelength.

When establishing maximum element size required to capture the minimum wavelength which is to be well-resolved during analyses, it is important to also consider the concept of soil softening during earthquake loading. As a soil softens, the shear modulus can degrade and the shear wave velocity of the soil will reduce, sometimes significantly. As a result, the minimum wavelength to be well resolved and propagating at the cutoff frequency will reduce; which in turn can turn can require smaller elements to properly capture the propagation of the motion. Therefore, the dependency of the mesh size on shear modulus degradation during dynamic shaking should be carefully considered with respect to the expected behaviour of the soil column.

Four-node SSPquad and SSPquadUP elements with plane strain formulations were used for the total and effective stress analyses, respectively. Both element types have a single integration point located at the centre of the element. These elements prevent instability at the incompressible-impermeable limit with a single integration point by using physical hourglass stabilization techniques (McGann et al., 2012). An extension of the work of Biot (1941; 1956; 1962) by Zienkiewicz and Shiomi (1984) is used for the mixed displacement-pressure (u-p) formulation to predict the development of pore water pressures in the SSPquadUP element

(McGann et al., 2012). A sketch of the SSPquad and SSPquadUP elements are shown in Figure 3-1.

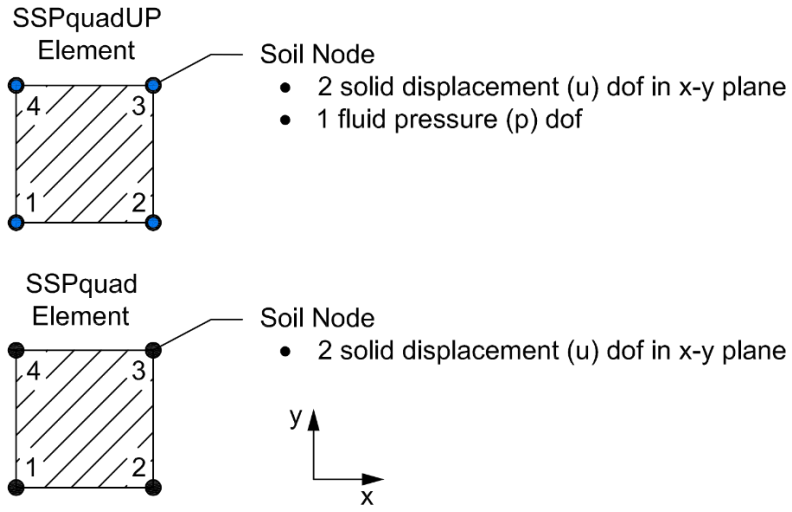

Figure 3-1: SSPquadUP and SSPquad elements

Pore pressure development during simulation with the SSPquadUP elements requires definition of the horizontal and vertical soil permeability as element input parameters. Horizontal and vertical permeability were assigned to be equal and constant throughout the soil column after establishing the in situ static stress condition.

3.5 Boundary Conditions

Boundary conditions on the displacement and fluid pore pressure degrees-of-freedom in the OpenSees continuum model are applied to the element nodes. The same boundary conditions were applied to the displacement degrees-of-freedom for the effective and total stress models. The fluid pressure degree-of-freedom in the effective stress analyses was fixed above the water table to prevent the variation of pore water pressure. Below the water table the fluid pressure degree-of-freedom was free to allow for the generation and/or dissipation of power water pressure.

The nodes at the base of the soil column are fixed against displacement in the vertical direction but are free to move in the horizontal direction. All other nodes above the base of the model

and at the same elevation along the soil profile are tied together in order to enforce equal displacements in the horizontal and vertical directions using the OpenSees EqualDOF command. The EqualDOF command was not applied to the pore pressure degree-of-freedom. The boundary conditions applied to displacement and pore pressure degrees-of-freedom are shown in Figure 3-2.

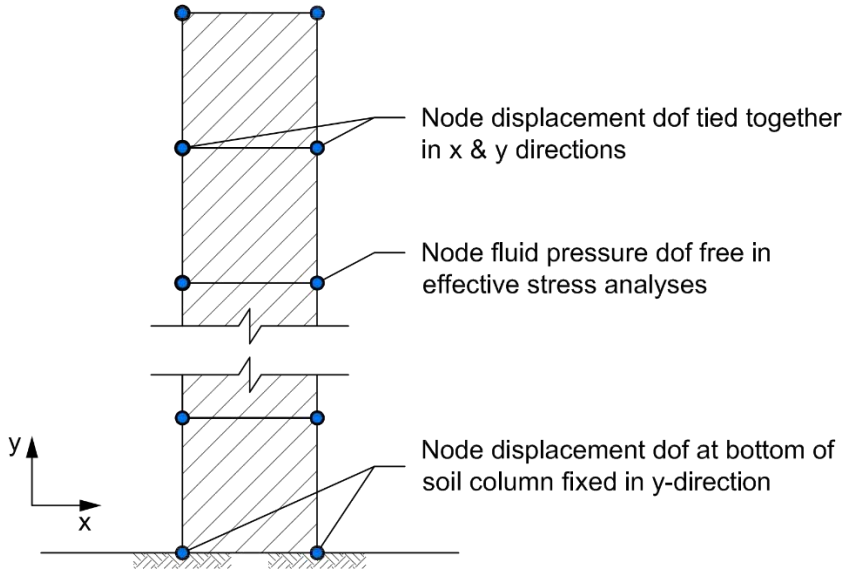

Figure 3-2: Boundary conditions for displacement and pore pressure degrees-of-freedom

3.6 Soil Constitutive Model

The SANISAND model (Dafalias and Manzari, 2004) was used to represent the sand soils in the seismic ground response analyses. The SANISAND model allows for the soil response to include volume change due to shearing, which is typically not considered in conventional one-dimensional seismic ground response analyses. Analyses for the real site case study (the Sendai site) presented in Chapter 4 also include an elastic isotropic material to simulate bedrock at the base of the model, which requires the definition of the elastic modulus, Poisson's ratio and mass density.

3.7 Lysmer-Kuhlemeyer Dashpot

To model the elastic half-space underlying the sand soil, a Lysmer and Kuhlemeyer (1969) dashpot is used at the base of the model and defined by a viscous uniaxial constitutive material and a zeroLength element type connected to a single node at the base of the column. The

viscous uniaxial material requires a dashpot coefficient c to be defined as the single material parameter. The dashpot coefficient c is determined in accordance with the recommendations of Joyner and Chen (1975) using the following equation,

$$c = \rho V_s \tag{3.3}$$

where ρ and V_s are the mass density and shear wave velocity of the underlying medium.

The earthquake motions which were used in the seismic ground response analyses were recorded at downhole array seismographs. Therefore, the input and simulated output motion at the base of the soil column should match closely. To achieve this match, it is necessary to use a very high shear wave velocity in the calculation of the Lysmer – Kuhlemeyer dashpot coefficient in order to achieve a better match between the input and output motion at the base of the column. As an example, Figure 3-3 compares simulated output acceleration response spectra at the base of an 8 m deep soil column based on Lysmer – Kuhlemeyer dashpot coefficients calculated with Vs = 500 m/s and Vs= 5000 m/s.

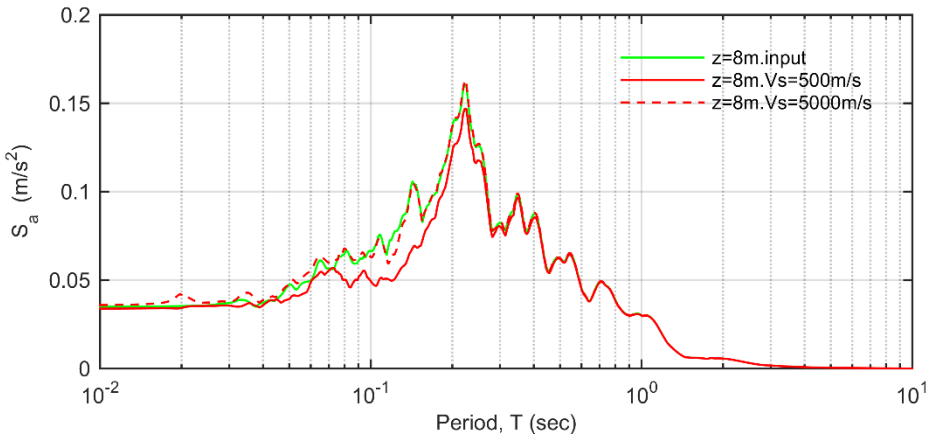

Figure 3-3: Comparison of Vs for Lysmer-Kuhlemeyer dashpot at base of column (z=8m) – input motion shown in green, output motion shown in red

As can be observed from Figure 3-3, the simulation with the dashpot coefficient determined using a Vs = 5000 m/s provides a better match to the input motion than the simulation with the dashpot coefficient determined using a Vs = 500 m/s.

3.8 Analysis Procedure

The seismic ground response analyses are completed in three stages, with the first and second stages being static analyses and the third stage being a transient dynamic nonlinear analysis, as described below:

- Stage 1 of the analysis applies the self-weight of the soil column using large time steps and a purely elastic material behavior. To achieve this, the material modulus matrix of the SANISAND model is set to model only elastic stiffness. Also during this stage the Poisson's ratio of the SANISAND constitutive model is set to establish the correct horizontal to vertical stress ratio k_0 within the soil column, as previously discussed in Section 2.3.3.

  Stage 1 comprises 250 time steps at 1.0 seconds each to apply the initial gravity forces to the soil column. After this, the SANISAND constitutive model Poisson's ratio is updated based on the model calibration.

- Stage 2 of the analysis updates the material modulus matrix to bring the system to equilibrium with elasto-plastic soil parameters for an additional 250 time steps at 1 second each.

- Stage 3 of the analysis (the final stage) applies a force time history at the base of the soil column with time steps of 0.01 s during the transient dynamic nonlinear analysis.

Model equilibrium was determined by reviewing the in situ changes of stress with time through the soil column during Stage 1 and 2. Based on this review, the number of time steps to reach equilibrium was adjusted as required until the correct in situ stress state stabilized. The number of time steps to achieve equilibrium is dependent on the continuum model and a different soil profile may require more / less or larger / smaller time steps to reach equilibrium.

For the effective stress analyses only, just prior to performing the Stage 3 dynamic analysis, the permeability of the SSPquadUP elements is updated to the value representing the

permeability of the soil to be modeled. Prior to this, a very large permeability of 1.0 m/s is applied for the Stage 1 and 2 analyses in order to prevent the build-up of excess pore pressure during the static analyses, and to simulate hydrostatic groundwater conditions.

The system solver SparseGeneral is used to solve the system of equations in the analyses and each analysis step must reach a normalized displacement increment of 0.001 within a maximum of 20 iterations during the dynamic analyses. The constraint equations of the analyses are enforced with the penalty method. During the Stage 1 and 2 static analyses, the Newmark time-stepping method is used to integrate the equations of motion with the parameters $\gamma = 0.83$ and $\beta = 0.44$. These parameters are selected to add numerical damping in order to quickly bring the model to static stability. During the Stage 3 dynamic analysis, the Newmark parameters are updated to $\gamma = 0.5$ and $\beta = 0.25$ and add no numerical damping to the simulation.

Rayleigh damping is applied during both the static and dynamic stages of the analysis. Target frequencies are selected to bound the range of dynamic response which is of interest for the seismic ground response analysis. The target Rayleigh damping ξ_r is matched at the specified target frequencies. The full Rayleigh damping formulation is used in OpenSees, meaning that the damping formulation takes the viscous damping matrix [C] originally proposed by Rayleigh and Lindsay (1945) below,

$$[C] = a_0[M] + a_1[K] \tag{3.4}$$

where [M] and [K] are the mass and stiffness matrices of the system, respectively, and a_1 and a_0 are the Rayleigh damping coefficients given by,

$$a_0 = \frac{4\pi\xi_r}{T_1 + T_2} \tag{3.5}$$

$$a_1 = \frac{T_1 T_2 \xi_r}{\pi(T_1 + T_2)} \tag{3.6}$$

where T_1 and T_2 are the periods of oscillation of the first and second target frequencies.

Chapter 4: Sendai Site Case Study

4.1 Introduction

The nonlinear seismic ground response analyses presented in this chapter was initially completed as part of the PRENOLIN (Improvement of PREdiction of soil NOn-LINear effects caused by strong seismic motion) project, which is a collaboration between research groups from North America, Europe and Asia, with the purpose of benchmarking numerical simulations of nonlinear seismic ground response analyses. However, the mandate of the PRENOLIN project was to focus primarily on total stress analyses. As such, the research presented in this thesis extended beyond the scope of the PRENOLIN project to investigate also effective one-dimensional nonlinear seismic ground response analyses.

The PRENOLIN project included both verification and validation phases. Verification and validation are the principal means concerning numerical analysis of assessing the reliability of the model implementation and computational simulation, respectively (Oberkampf et al., 2003). Specifically, verification identifies and quantifies errors in computer programming and numerical errors, and has no relation to the real world; whereas validation compares numerical simulations with conditions representative of a real scenario, such a case history or experimental data (Oberkampf et al., 2003; Tasiopoulou et al., 2015).

The verification phase of PRENOLIN was carried out to check the implementation of the numerical model by analyzing ideal, or unrealistically simple soil columns. The focus of the research presented in this chapter pertains to the validation phase of PRENOLIN, which comprised simulation of the Sendai downhole seismograph array in Japan.

The Sendai site is an instrumented site which is part of a strong-motion observation network operated by the Port and Airport Research Institute of Japan. The nonlinear analyses to assess the propagation of nine input motions through the Sendai site were carried out using the computational platform OpenSees (Open System for Earthquake Engineering Simulation) developed by McKenna and Fenves (2001). As discussed in Chapter 3, the bounding surface plasticity model SANISAND as proposed by Dafalias and Manzari (2004) was used to model

the hysteretic nonlinear stress-strain behaviour of the sand soils. Further information on the site location, soil stratigraphy and properties, available laboratory data and earthquake motions used in the seismic ground responses analyses are provided in the following sections.

4.2 Site Location and Investigation

The instrumented site which is the focus of this case study is located in the City of Tagajo of the Sendai District in Japan. A soils investigation report prepared by the OYO Corporation (2014) documents the field investigation and laboratory testing program carried out to characterize the soil properties at the site.

The site investigation carried out by the OYO Corporation included two mud rotary boreholes advanced adjacent to each other. One borehole was advanced for the purpose of logging the subsurface soil conditions with Standard Penetration Tests (SPTs) every 1 m over the depth of the hole. The SPTs provide the N-value of the soil, which is the number of blows required to advance a split-spoon sampler through the soil a distance of 300 mm, and gives an indication of the in situ relative density of the soil. However, the SPT data was not used in the analyses of this research. The second borehole completed by the OYO Corporation was advanced to collect relatively undisturbed samples of the sand soils which were dehydrated and frozen at the time of sampling (OYO, 2014). These samples were collected with a triple-tubed walled sampler. The elastic p-wave and s-wave velocities of the soil were determined using the down-hole method of PS logging.

4.3 Laboratory Program

As part of the OYO Corporation soil investigation, a laboratory testing program was completed to analyze the soil properties of the Sendai site. The program included a series of tests to determine the index and strength properties of the Sendai site soils. The index tests include analysis of soil particle size distribution, Atterberg limits and relative density. Other tests included drained monotonic triaxial compression tests and undrained cyclic triaxial tests. All tests were reported to have been completed in accordance with the recommended procedures of the Japanese Industrial Standards for Laboratory Tests on Soils (JIS) and the Japanese Geotechnical Society (JGS).

Of particular importance to the calibration of the SANISAND constitutive model are the monotonic and cyclic triaxial tests completed as part of the OYO Corporation (2014) laboratory program. A summary of the triaxial testing program carried out by the OYO Corporation is presented in Table 4-1.

Table 4-1: Summary of triaxial testing program

Sample Name	Depth (m)	Test Completed
T2-2	2.8 – 3.8	CUT
T2-4	4.9 – 5.9	MDT
		CUT

In Table 4-1 MDT corresponds to drained monotonic triaxial compression tests and CUT corresponds to the cyclic undrained triaxial tests.

Three drained monotonic triaxial tests were reported for soil specimens collected from a depth between 4.9 and 5.9 m below the surface (Specimen No. T2-4). Each test was loaded to a different effective consolidation pressure before shearing. A summary of the monotonic triaxial tests is provided in Table 4-2.

Table 4-2: Summary of monotonic triaxial tests

Specimen No.	Effective Consolidation Pressure, p_{in}' (kPa)	Back Pressure (kPa)	Void ratio post-consolidation, e_{in}
T2-4(1)	50	200	0.72
T2-4(2)	100	200	0.64
T2-4(3)	200	200	0.57

Undrained cyclic triaxial tests were stress-controlled and reported for two soil specimens, one collected from a soil sample between 2.8 and 3.8 m depth (Specimen No. T2-2), and one from a soil sample between 4.9 and 5.9 m depth (Specimen No. T2-4). Each soil specimen was

loaded to different effective consolidation pressures before shearing. Following consolidation, the soil specimens were subjected to cyclic load stages where increasing magnitudes of deviatoric stress were applied during each load stage. Each load stage included ten cycles (OYO Corporation, 2014). The cyclic triaxial tests are summarized in Table 4-3.

Table 4-3: Summary of undrained cyclic triaxial tests

Specimen	Void ratio post-consolidation, e_{in}	Mean Effective Post-Consolidation Stress, $p_{in}{}'$	Loading Frequency (Hz)	No. of Loading Stages
T2-2	0.697	44	0.25	8
T2-4	0.595	64	0.25	10

The half-amplitude of axial stress was reported for each load stage of the cyclic triaxial tests. The OYO Corporation (2014) reports peak-to-peak amplitude. Therefore, the half-amplitude axial stress is equivalent to the deviatoric stress, which is reported for each load stage in Table 4-4. Likewise, amplitude when referenced with respect to strain reported by the OYO Corporation (2014) is peak-to-peak amplitude.

Table 4-4: Summary of cyclic triaxial loading stage deviatoric stress

Load Stage	Deviatoric Stress, q (kPa)	
	T2-2	**T2-4**
1	±1.0	±1.7
2	±1.5	±2.5
3	±2.4	±3.8
4	±3.9	±5.9
5	±6.3	±9.5
6	±9.9	±15.2
7	±14.3	±22.8
8	±19.4	±32.0
9	N/A	±40.4
10	N/A	±51.4

4.4 Site Stratigraphy and Soil Properties for Seismic Ground Response Analyses

Based on the findings of OYO Corporation (2014), site stratigraphy and soil properties were assigned by the PRENOLIN organizing team to eliminate differences in soil data interpretation between the different research groups participating in the PRENOLIN project. The Sendai site stratigraphy was defined as 7 m of sandy soils overtop of slate rock, as reported by the OYO Corporation (2014). The water table was reported to be at 1.45 m below the surface. The soil properties provided by the PRENOLIN organizing team which are relevant to the analyses completed for this research are summarized in Table 4-5.

Table 4-5: General soil properties of the Sendai site

Depth (m)	V_s (m/s)	ρ (kg/m^3)	G/G_{max} & ξ Curve
1	120	1850	Specimen T2-2
2	170	1850	Specimen T2-2
3	200	1850	Specimen T2-2
4	230	1890	Specimen T2-4
5	260	1890	Specimen T2-4
6	280	1890	Specimen T2-4
7	300	1890	Specimen T2-4
8	550	2480	N/A

In Table 4-5 V_s is the shear wave velocity, ρ is the mass density, and G/G_{max} & ξ Curve refers to the shear modulus reduction and damping curves to be considered for calibration of the soil constitutive model, as discussed further below. These curves were established from cyclic triaxial testing on either Specimen T2-2 or T2-4. The modeled site stratigraphy is illustrated in Figure 4-1.

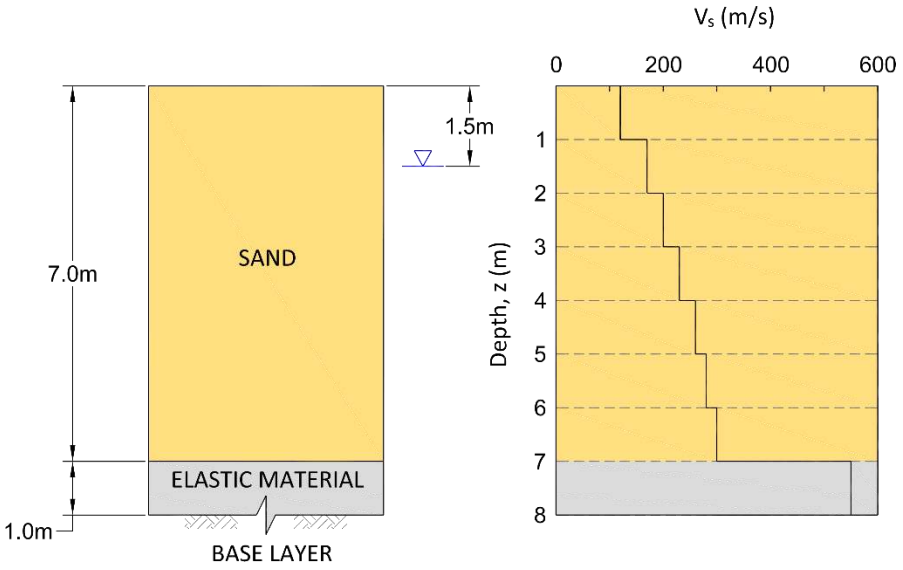

Figure 4-1: Sendai site stratigraphy, shear wave velocity and mass density with depth

The shear modulus reduction and damping curves for Specimen T2-2 and T2-4 referenced in Table 4-5 and provided for the calibration of the constitutive model are presented in Figure 4-2 and Figure 4-3.

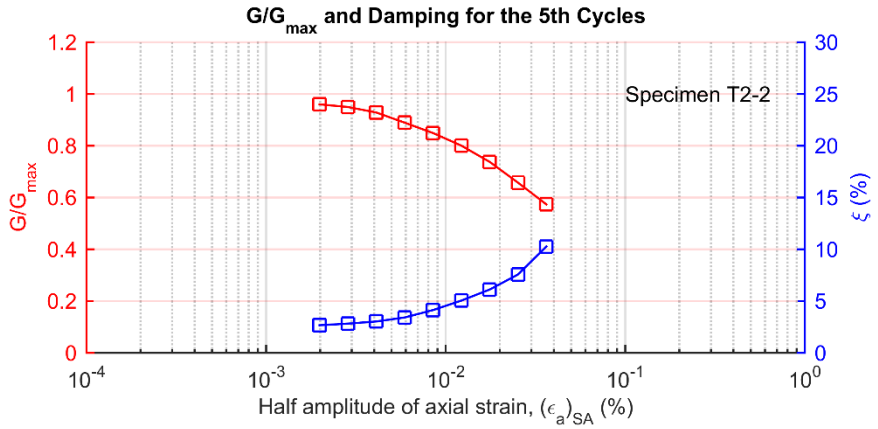

Figure 4-2: Specimen T2-2 G/G_{max} and Damping Curves from Cyclic Triaxial Tests

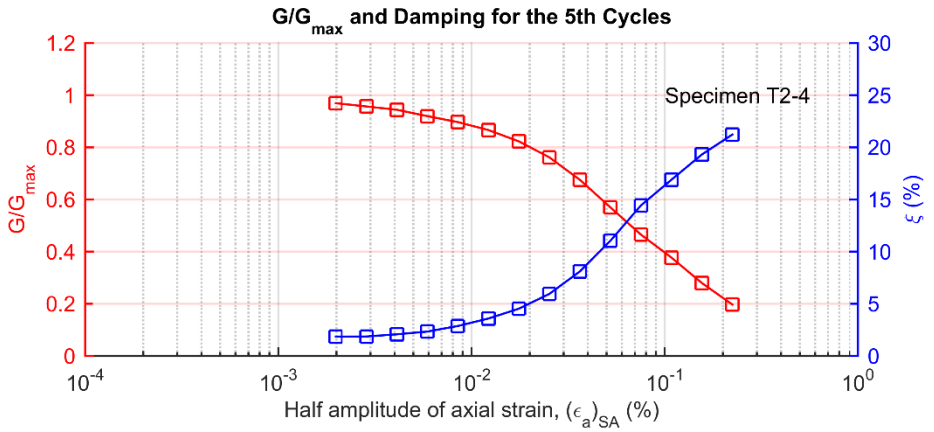

Figure 4-3: Specimen T2-4 G/G_{max} and Damping Curves from Cyclic Triaxial Tests

The secant shear modulus to establish the shear modulus reduction curves in Figure 4-2 and Figure 4-3 was determined for the fifth cycle of each load stage of the cyclic triaxial tests. The maximum shear modulus values for normalization of the laboratory shear modulus reduction curves were determined using the Hardin-Drnevich relation (Hardin and Drnevich, 1972) to estimate the small-strain elastic modulus at an axial strain of $1 \times 10^{-4}\%$ (OYO, 2014). The maximum laboratory shear modulus was then calculated from the small-strain elastic modulus using the following relation,

$$G = \frac{E}{2(1+\nu)} \quad \textbf{(4.1)}$$

where ν is the Poisson's ratio of the soil. In the case of undrained cyclic triaxial testing the Poisson's ratio is equal to 0.5, as the undrained loading condition results in zero elastic volumetric strains occurring. Further discussion on the selection of shear modulus values for simulation is provided in Section 4.7.4.

Based on the results of the consolidated drained monotonic triaxial test carried out by the OYO Corporation (2014), an effective internal friction angle (φ') of approximately 44° was adopted for the sand soils by the PRENOLIN organizing team. Using this value for internal friction angle, the coefficient of at rest lateral earth pressure K_0 for the sand was determined to be 0.31 using the following equation proposed by Jaky (1944),

$$k_0 = 1 - sin\varphi' \quad \textbf{(4.2)}$$

The approximate fundamental period of vibration T_s for the site was calculated to be 0.12 s based on the relation

$$T_s = \frac{4H}{V_{s-avg}} \quad \textbf{(4.3)}$$

where H is the height of the site and $V_{s\text{-}avg}$ is the average shear wave velocity of the site.

The effective stress analyses require the additional parameter of soil permeability, k, which in absence of such data was selected to be $k = 10^{-5}$ m/s based on the soil description in the OYO Corporation report (2014) and soil permeability values referenced in Terzaghi and Peck (1967).

4.5 Earthquake Input Motions

Nine earthquake motions recorded at the Sendai site downhole seismograph were used as input motions for the nonlinear seismic ground response analyses. The seismograph was reported by the PRENOLIN organizing team to be located within the bedrock layer, at a depth of 10.4 m below the site surface. Input time histories of acceleration, velocity and displacement were obtained from the PRENOLIN organizing team for the analyses.

The nine motions were selected based on the peak ground acceleration (PGA) and central frequency content of the motion. A summary of the earthquake motion time series and their moment magnitude M_w, epicentral distance from the Sendai site, and depth is provided in Table 4-6.

Table 4-6: Summary of earthquake time series (adapted from Marot, 2015)

Time Series	M_w	Epicentral Distance (km)	Depth (km)	Duration (sec)	PGA (g)
TS1	9.0	162.7	23.7	312	0.251
TS2	7.1	81.3	72.0	137	0.063
TS3	6.4	19.1	11.9	106	0.062
TS4	6.8	169.4	108.1	141	0.025
TS5	5.9	96.4	30.7	111	0.026
TS6	7.2	83.4	7.8	156	0.036
TS7	5.9	94.7	41.2	78	0.012
TS8	6.4	208.0	34.5	78	0.005
TS9	5.8	175.9	47.0	78	0.003

The acceleration time history and spectral acceleration (Sa) response spectrum for each input motion are provided at the same scale in Figure 4-4 through Figure 4-12. The spectral acceleration response spectrum plots have a damping ratio of 5%.

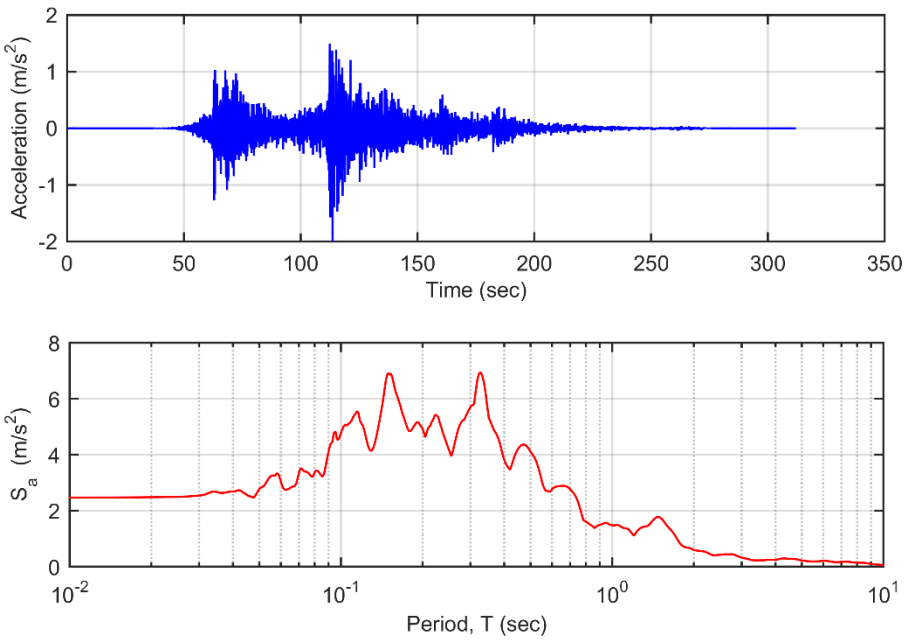

Figure 4-4: Input motion TS1 acceleration time history and acceleration response spectra (for a 5 percent damping)

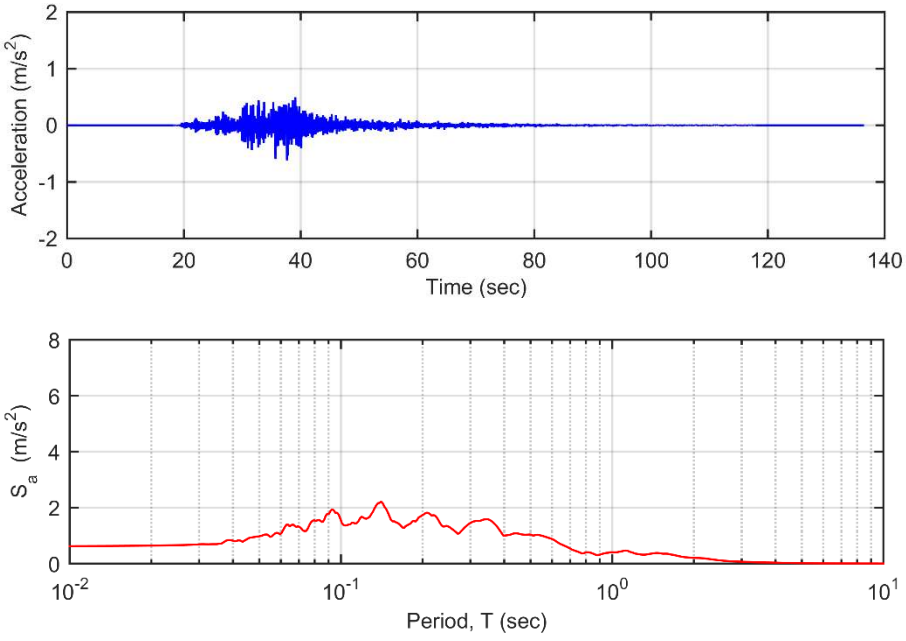

Figure 4-5: Input motion TS2 acceleration time history and acceleration response spectra (for 5 percent damping)

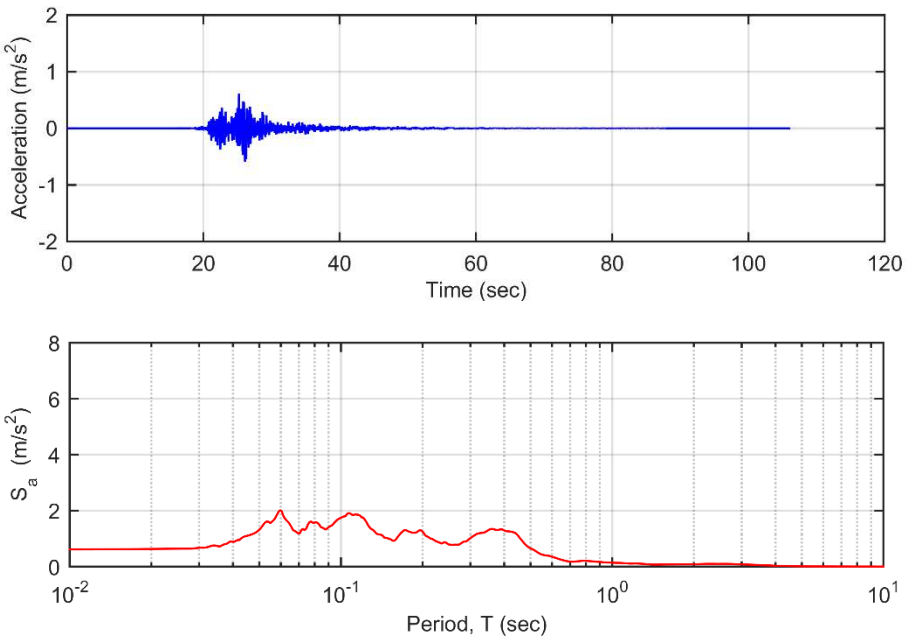

Figure 4-6: Input motion TS3 acceleration time history and acceleration response spectra (for 5 percent damping)

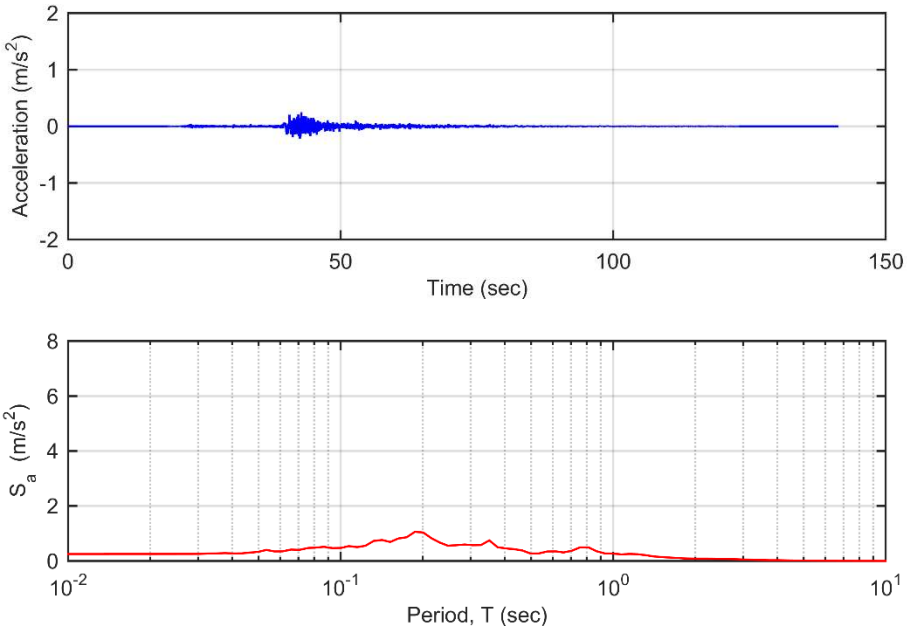

Figure 4-7: Input motion TS4 acceleration time history and acceleration response spectra (for 5 percent damping)

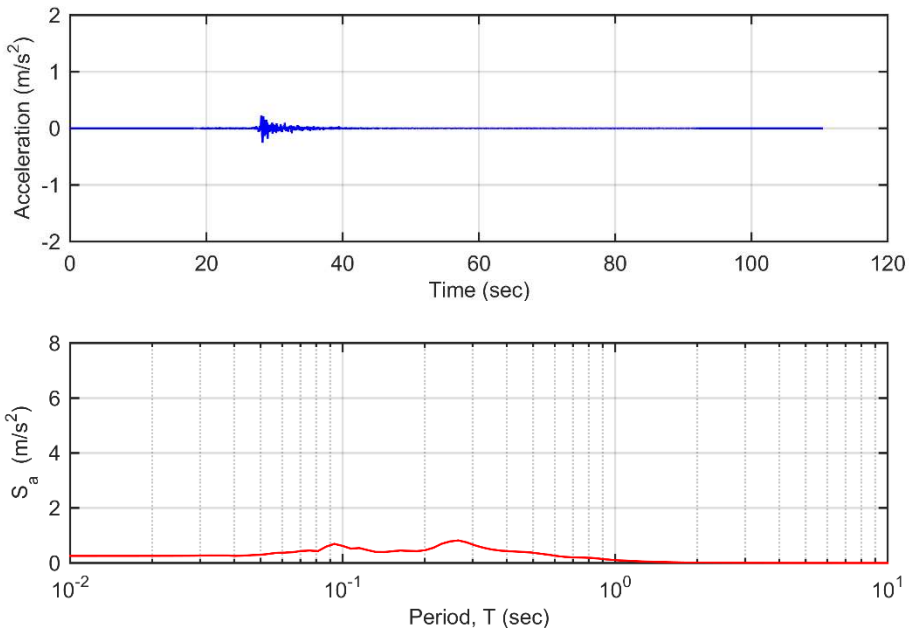

Figure 4-8: Input motion TS5 acceleration time history and acceleration response spectra (for 5 percent damping)

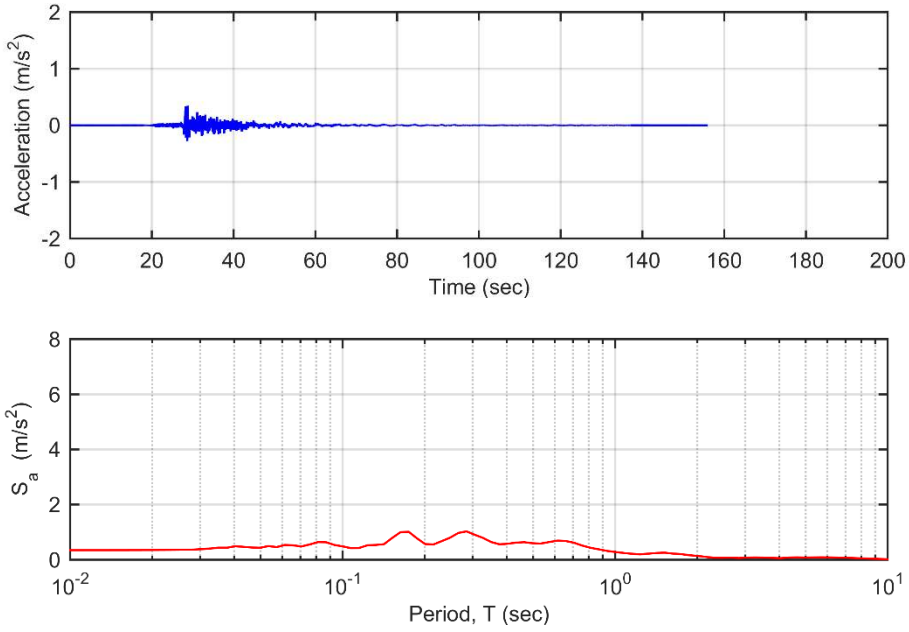

Figure 4-9: Input motion TS6 acceleration time history and acceleration response spectra (for 5 percent damping)

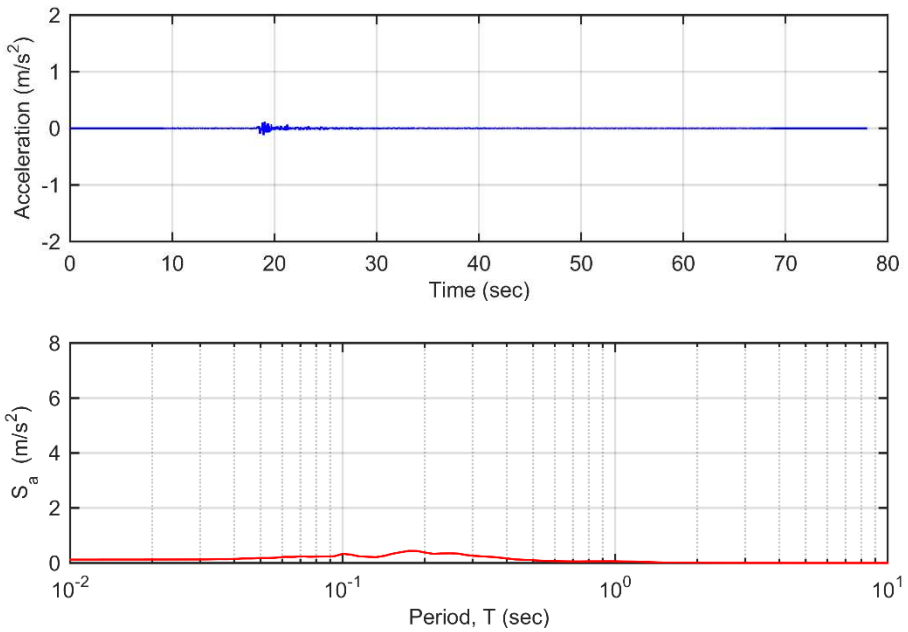

Figure 4-10: Input motion TS7 acceleration time history and acceleration response spectra (for 5 percent damping)

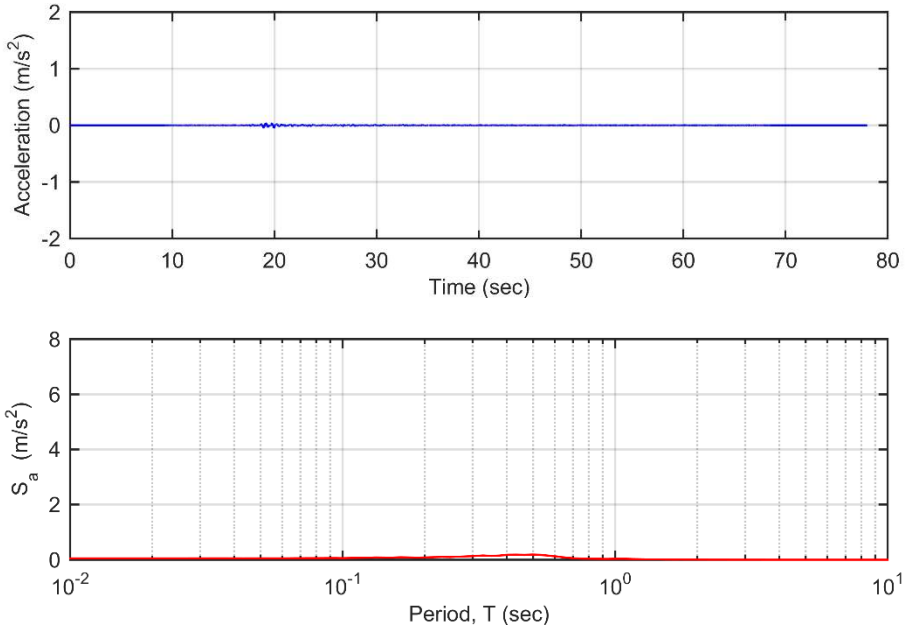

Figure 4-11: Input motion TS8 acceleration time history and acceleration response spectra (for 5 percent damping)

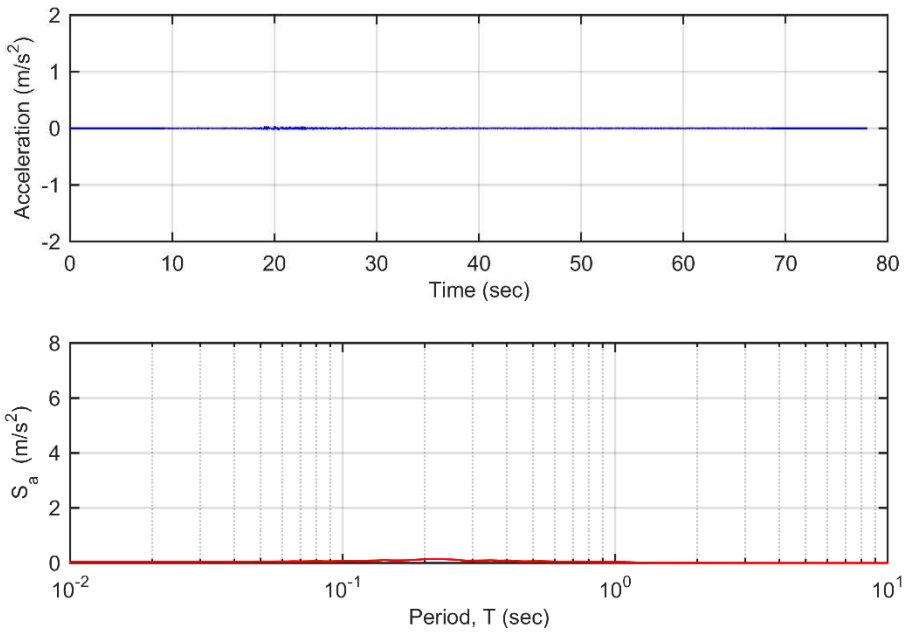

Figure 4-12: Input motion TS9 acceleration time history and acceleration response spectra (for 5 percent damping)

It is apparent from Figure 4-4 through Figure 4-12 that most of the motions used in the analyses are relatively weak, with the acceleration time history and response spectrum for time series TS7, TS8 and TS9 being difficult to discern when plotted at the same vertical scale as time series TS1 through TS6. In order to more clearly illustrate the motion characteristics, the acceleration time histories and 5% damping response spectrums for motions TS2 through TS9 are re-plotted at different scales in Figure 4-13 through Figure 4-20. TS1 is not re-plotted as its time history and response spectrum is clear in Figure 4-4.

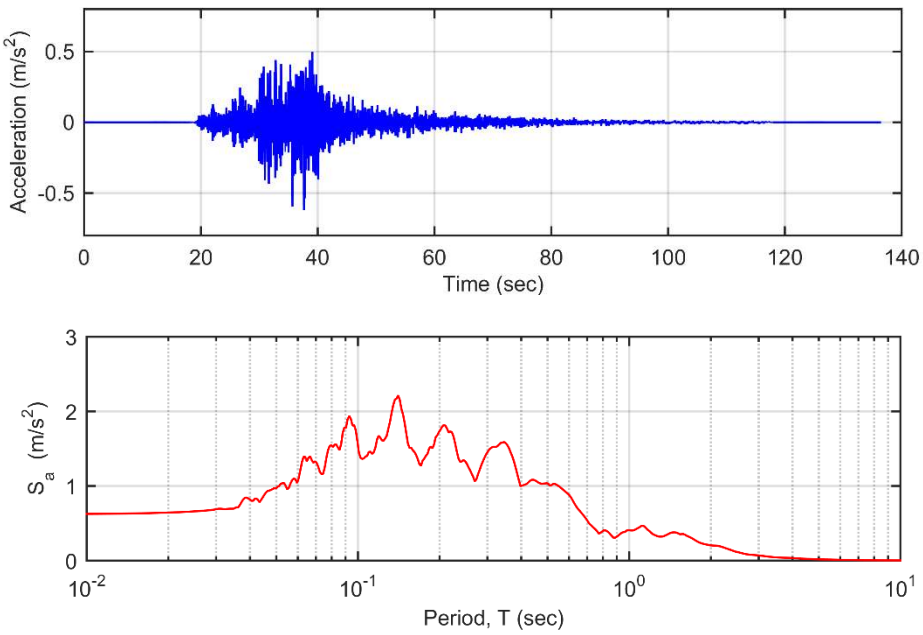

Figure 4-13: Input motion TS2 acceleration time history and acceleration response spectra (for 5 percent damping) re-plotted at large scale

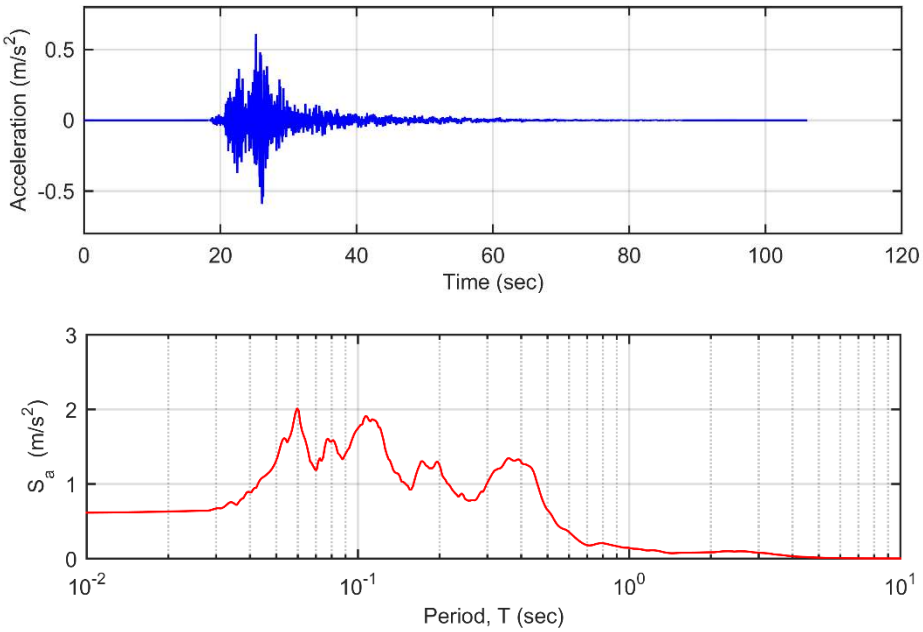

Figure 4-14: Input motion TS3 acceleration time history and acceleration response spectra (for 5 percent damping) re-plotted at large scale

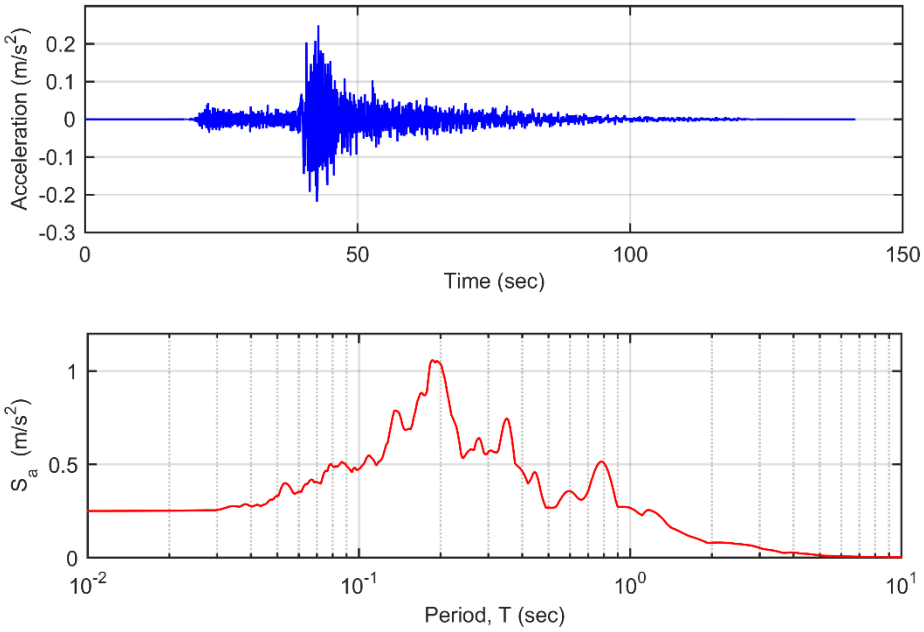

Figure 4-15: Input motion TS4 acceleration time history and acceleration response spectra (for 5 percent damping) re-plotted at large scale

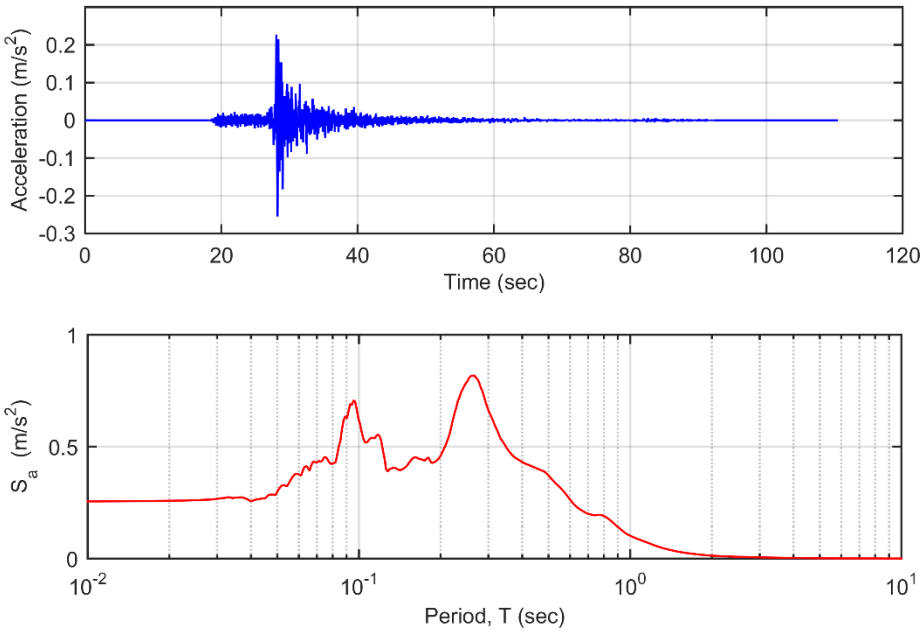

Figure 4-16: Input motion TS5 acceleration time history and acceleration response spectra (for 5 percent damping) re-plotted at large scale

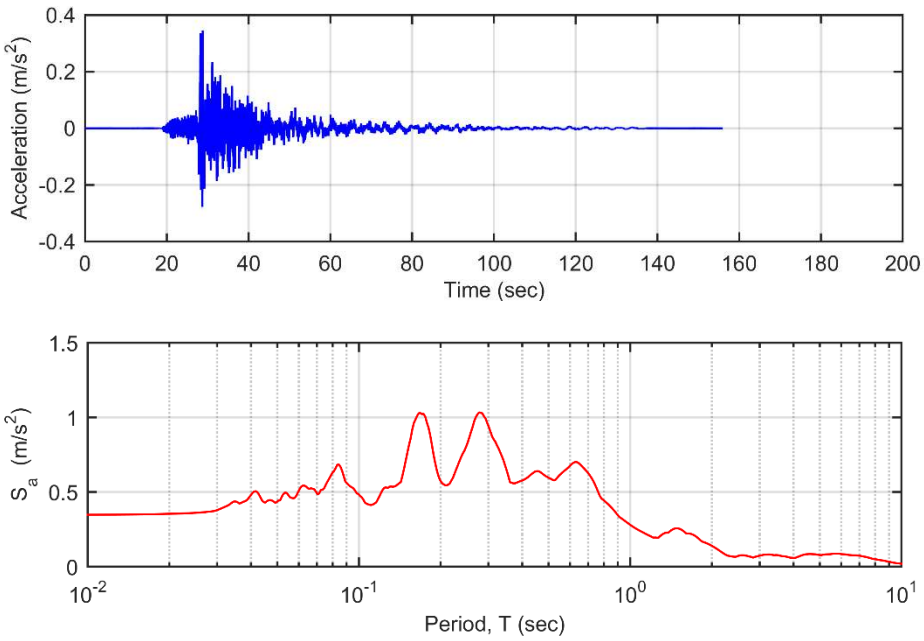

Figure 4-17: Input motion TS6 acceleration time history and acceleration response spectra (for 5 percent damping) re-plotted at large scale

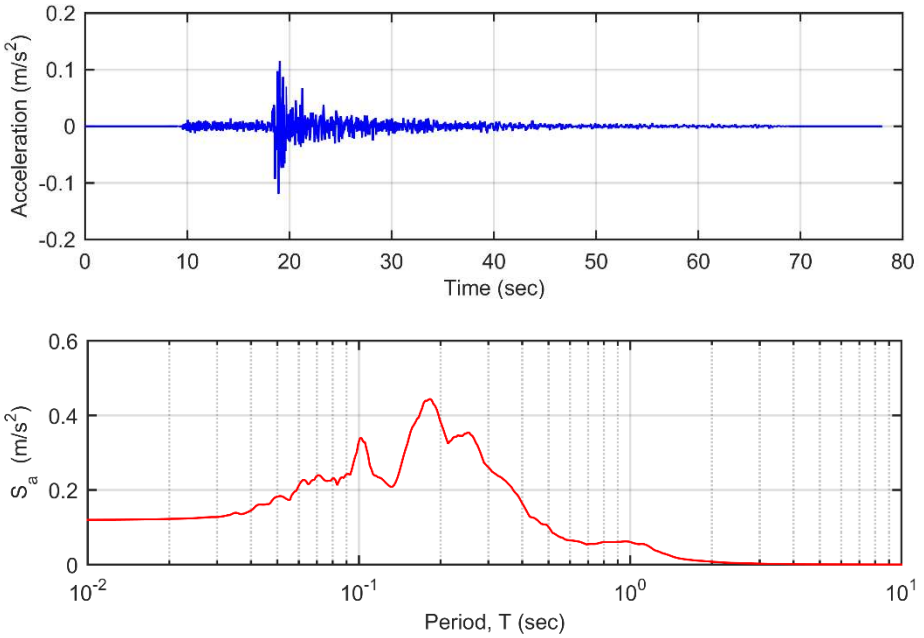

Figure 4-18: Input motion TS7 acceleration time history and acceleration response spectra (for 5 percent damping) re-plotted at large scale

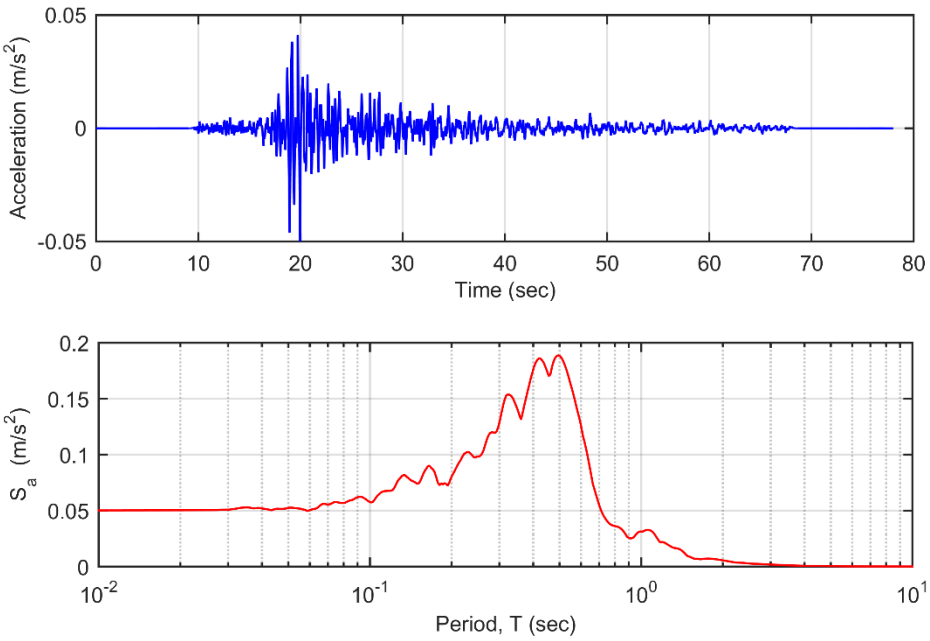

Figure 4-19: Input motion TS8 acceleration time history and acceleration response spectra (for 5 percent damping) re-plotted at large scale

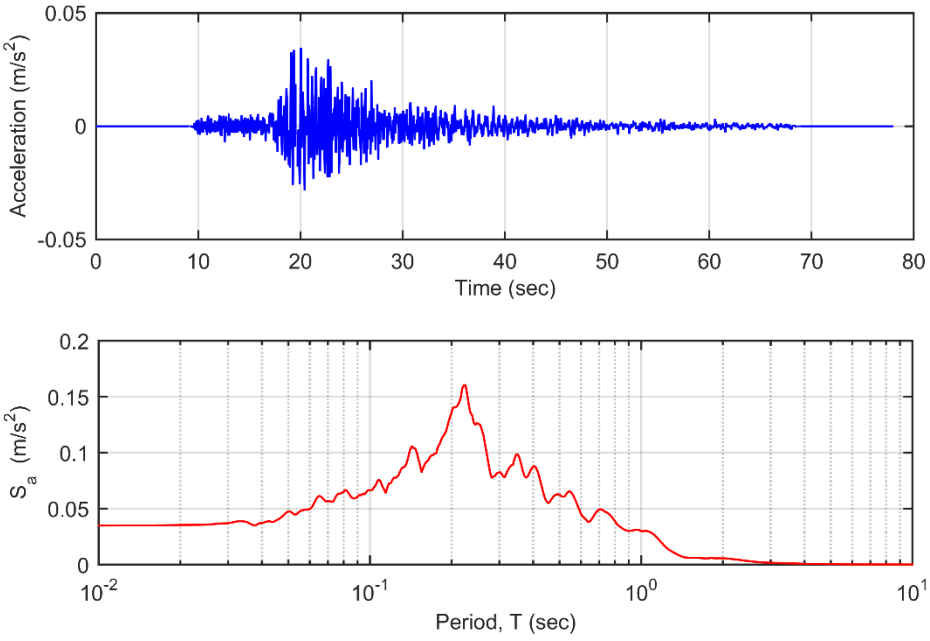

Figure 4-20: Input motion TS9 acceleration time history and acceleration response spectra (for 5 percent damping) re-plotted at large scale

4.6 Description of Continuum Model

The continuum models for the seismic ground response analyses, including the model geometry, soil elements and boundary conditions are generally described in Chapter 3. Additional details of the continuum model which are specific to the Sendai site are presented in this section.

The analyses of the Sendai site all consider an 8 m deep site, with a 7 m thick layer of sand soil overlying 1 m of isotropic elastic material. The groundwater table in the model is located at 1.5 m below the surface. General schematics of the total and effective stress continuum models are presented in Figure 4-21 and Figure 4-22.

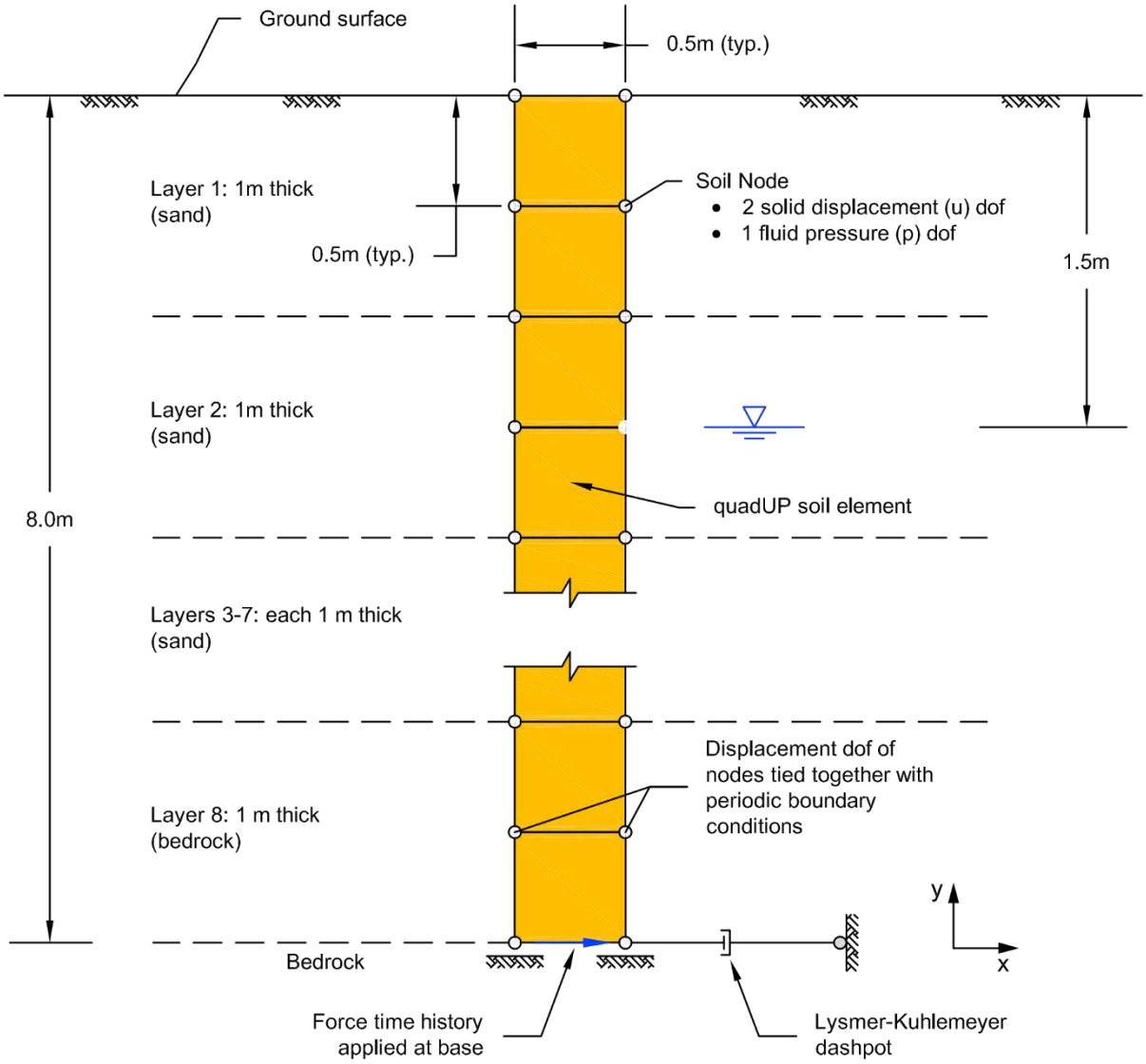

Figure 4-21: Effective stress continuum model for the Sendai site

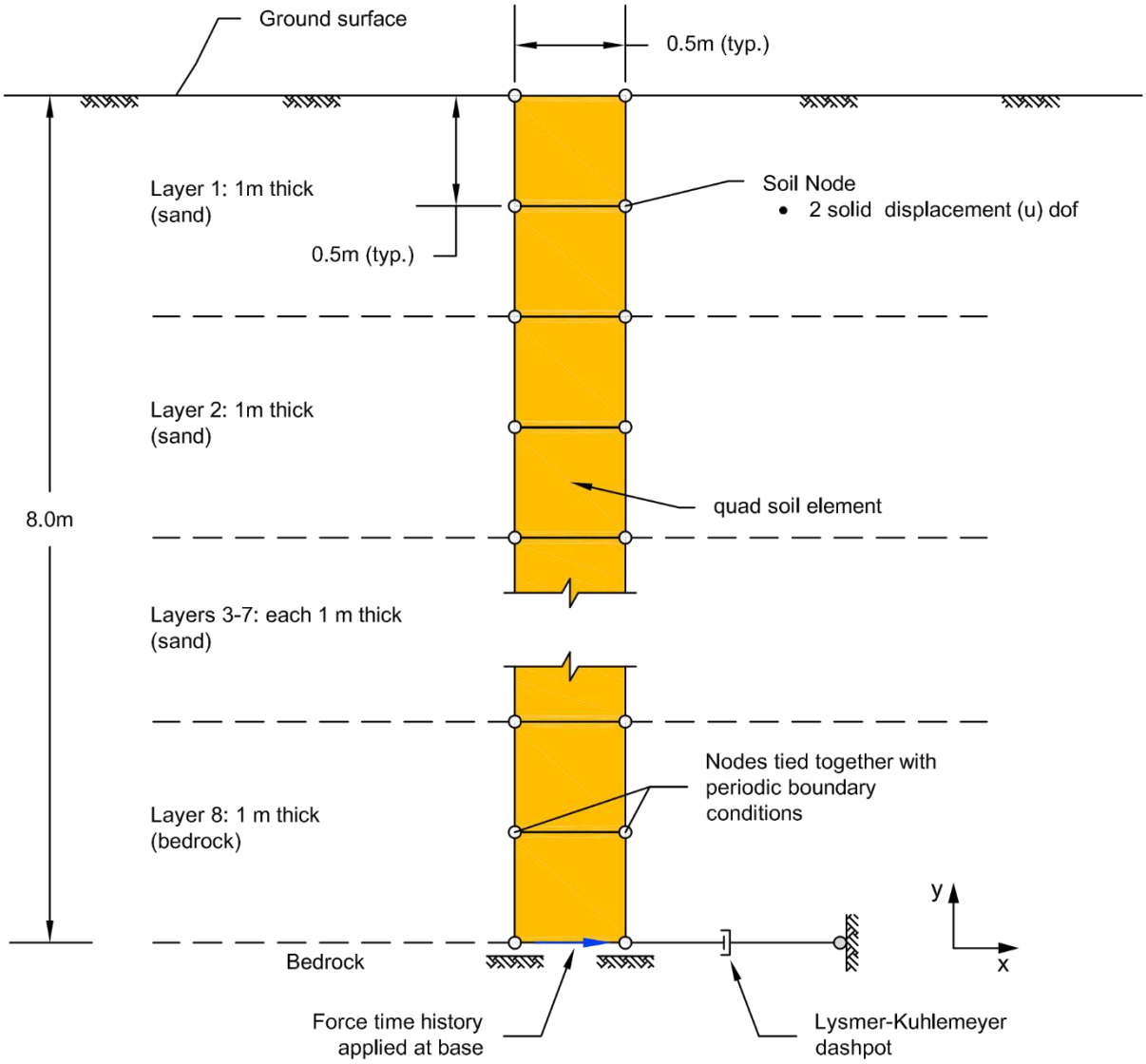

Figure 4-22: Total stress continuum model for the Sendai site

The cutoff frequency considered for the analyses was selected to be 25 Hz. On this basis, the minimum element size required to allocate eight elements to a wavelength propagating with a maximum frequency of f_{max} = 25 Hz. through soil with a $V_{s\text{-}min}$ = 120 m/s was determined to be Δ_y = 0.5 m. The element size in the horizontal direction was set equal to the vertical direction.

The SANISAND model parameters were selected based on calibration procedures discussed in Section 4.7. For the elastic isotropic material underlying the sand, the shear modulus was

750 MPa, based on the reported values of shear wave velocity and mass density. The mass density of the elastic material was $\rho = 2480$ kg/m^3 as per Table 4-5.

The Poisson's ratio to develop the model stresses under static conditions was selected in order to establish $K_0 = 0.31$, based on an effective internal friction angle of approximately 44° and Equation (4.2).

The mass density for calculation of the Lysmer-Kuhlemeyer dashpot coefficient was taken to be the same as the mass density of the elastic material between 7 and 8 m depth. A shear wave velocity of $V_s = 5000$ m/s was used for the calculation of the dashpot coefficient as it provided a close match between the recorded input and simulated output motions at the base of the continuum model.

The target Rayleigh damping was selected as $\xi = 2\%$ to match the level of damping observed at small strain during cyclic triaxial testing carried out by OYO Corporation (2014). The target frequencies for Rayleigh damping were selected to be 0.1 and 10 Hz. These target frequencies were selected to approximately bound the range of frequency where the ground response was of interest.

4.7 Calibration of the SANISAND Model

The calibration of the SANISAND constitutive model to develop the model parameters which were used in the seismic ground response analyses of the Sendai site is presented in this section.

The input parameters for the SANISAND soil constitutive model were calibrated to the laboratory test data and then adjusted to the in-situ measurements of G_{max} (based on shear wave velocity) that were provided with the OYO Corporation report (2014). The calibration procedure and results are presented in this section.

4.7.1 Calibration to Monotonic Consolidated-Drained Triaxial Test Data

Monotonic triaxial tests that approach critical state are required to calibrate the critical state parameters of the SANISAND model (M, λ, e_0). For the purpose of calibration, it is preferable to have undrained and drain monotonic triaxial tests on samples which are dense and loose of the critical state line. This way, when the soil is sheared, the recorded test data approaches the critical state line from both the loose and dense of critical conditions, which enables a more accurate representation of the critical state line. Such a set of data is reproduced from Taiebat et al. (2010) in Figure 4-23.

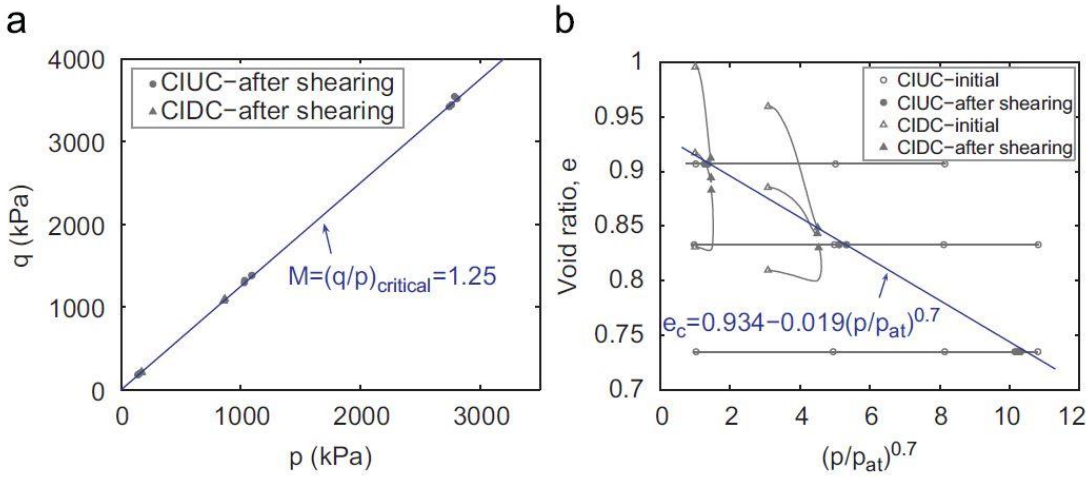

Figure 4-23: Monotonic triaxial data for calibration of SANISAND critical state parameters (Taiebat et al., 2010)

The monotonic triaxial tests carried out by the OYO Corporation (2014) and used for calibration of the SANISAND model were all drained triaxial tests completed on a soil sample collected from the Sendai at a depth between 4.9 – 5.9 m below the site surface (Specimen No. T2-4). The three specimens tested were loaded to effective consolidation pressures p_i of 50 kPa, 100 kPa and 200 kPa, respectively, before shearing (OYO, 2014).

The results of the monotonic triaxial tests which show the change in deviator stress q and volumetric strain ε_v with increasing axial strain ε_a are presented in Figure 4-24.

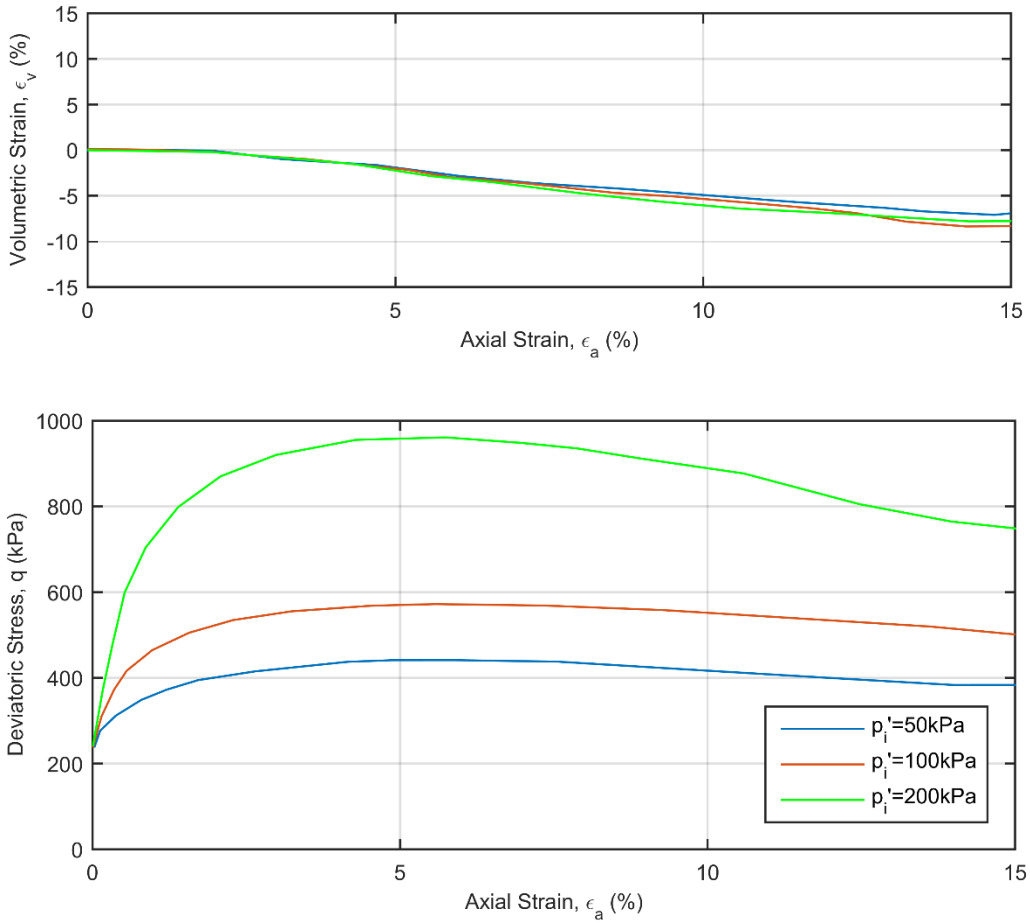

Figure 4-24: Monotonic triaxial test results on sample Sendai T2-4 (adapted from OYO, 2014)

All monotonic triaxial tests were completed on tests which were dense of critical state, as can be inferred from the negative volumetric strain which occurred within increasing strain in Figure 4-24.

Ishihara (1996) showed that samples of Toyoura sand exhibited critical state behavior at axial strains as large as 25%. Review of the data presented in Figure 4-24 indicates that the soil specimens likely had not reached critical state at the end of testing at 15% axial strain for the two tests completed at effective consolidation pressures of 100 and 200 kPa, and possibly also for the test at an effective consolidation pressure of 50 kPa. As the samples tested were all dense of critical state, it is possible that shear bands developed within the samples during the tests. The shear bands may have reached critical state but the overall sample response is not representative of a sample being at critical state.

For the calibration of the critical state parameters of the SANISAND constitutive model, it is required to estimate the mean and deviatoric effective stress and volumetric strain at critical state. For this purpose, it was necessary to extrapolate the test data in Figure 4-24 beyond 15% axial strain in order to estimate these values at critical state. Table 4-7 provides a summary of the mean and deviatoric effective stress and volumetric strain at critical state, estimated by extrapolating the monotonic triaxial data past 15% axial strain to an interpreted critical state condition.

Table 4-7: Monotonic triaxial results by extrapolation to assumed critical state

Effective Consolidation Pressure, $p_{in}{}'$ (kPa)	Deviatoric stress at critical state, q_c (kPa)	Mean effective stress at critical state, $p_c{}'$ (kPa)	Volumetric strain at critical state, ε_{v-c} (%)	Void ratio post-consolidation, e_{in}	Void ratio at critical state, e_c
50	95	82	-7.9	0.72	0.86
100	235	177	-8.7	0.64	0.78
200	514	371	-7.1	0.57	0.68

The void ratio at critical state as presented in Table 4-7 was determined using the expressions,

$$e_c = e_0 - \Delta e \tag{4.4}$$

$$\Delta e = (1 + e_0)\varepsilon_{v-cs} \tag{4.5}$$

The critical state stress ratio M and the parameters λ, e_0, and ξ which define the critical state line of Equation (2.12) in e-p space can be determined by fitting these parameters as plotted in Figure 4-25.

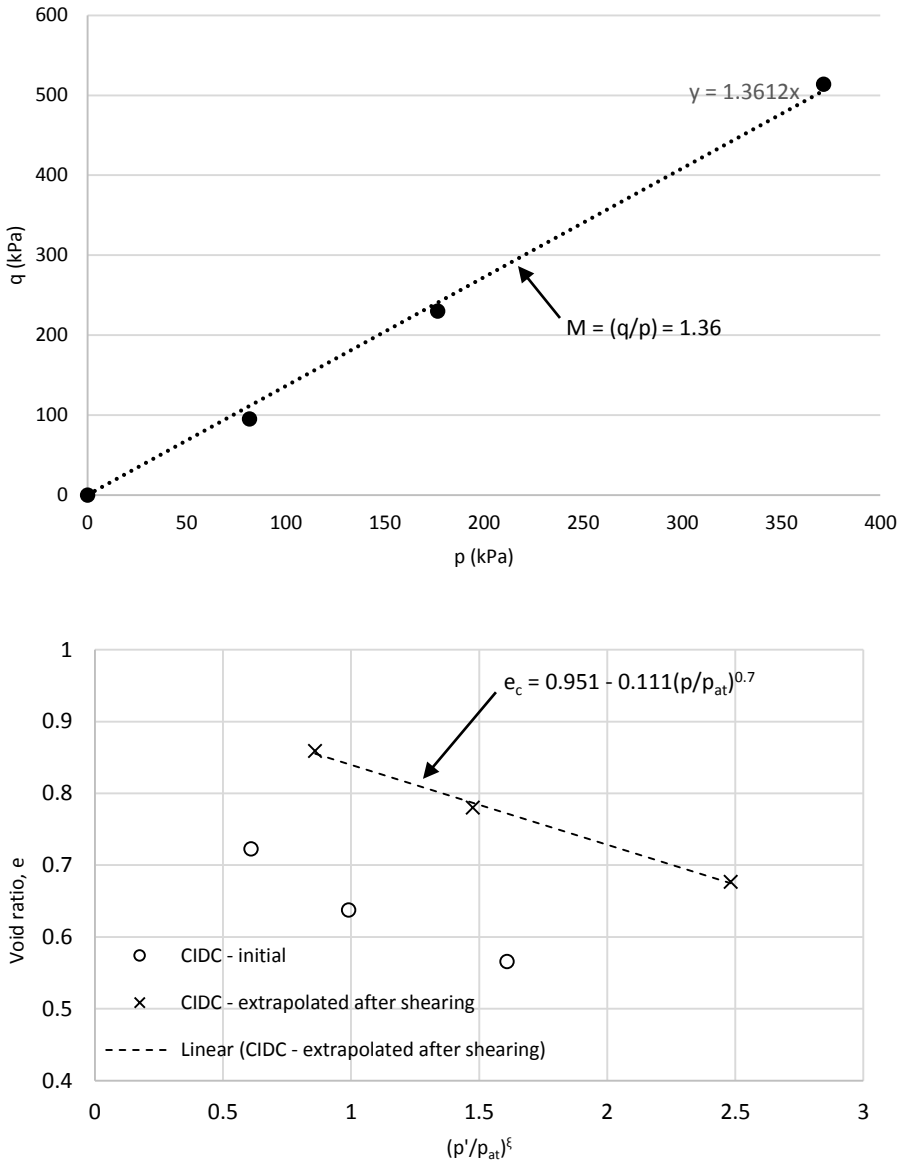

Figure 4-25: Calibration plots for critical state parameters

The material parameter ξ was selected as the default value of 0.7 for sands, as per the recommendations of Li and Wang (1998).

4.7.2 Calibration to Consolidated-Undrained Cyclic Triaxial Test Data

The undrained cyclic triaxial tests carried out by the OYO Corporation (2014) were used to calibrate the elasticity (G_0, ν), dilatancy (n^d, A_0), plastic modulus (n^b, h_0, c_h), and fabric

dilatancy (z_{max}, c_z) parameters of the SANISAND model. The calibration was completed by numerically simulating with the SANISAND constitutive model the cyclic triaxial tests carried out by the OYO Corporation (2014), and comparing the results of the simulations to the laboratory data. The simulations were carried out using the implemented SANISAND model in a general-purpose constitutive driver prepared in MATLAB framework by Taiebat (2008).

The cyclic triaxial simulations were completed iteratively to find a suitable set of SANISAND model parameters to fit the laboratory data. Model parameter values were initially selected based on the calibration to drained monotonic triaxial tests, and the typical range of parameter values reported in previous research by Dafalias and Manzari (2004) and Taiebat et al. (2010). After each iteration of a cyclic triaxial simulation, a series of plots which compared the simulated versus experimental stress-strain response and G/G_{max} and damping curves were developed. These plots formed the basis for evaluating the fit of the model simulation to the laboratory data and establishing the model parameters.

The simulated shear modulus reduction curves developed from the MATLAB constitutive driver for the SANISAND model were normalized with a maximum shear modulus value which was calculated using the relation,

$$G_{max} = \frac{\tau_{avg}}{\gamma_{avg}} \tag{4.6}$$

where G_{max} is the undrained simulated cyclic triaxial maximum shear modulus for the fifth cycle of the first loading stage, and τ_{avg} and γ_{avg} are the simulated average shear stress and strain for the fifth cycle of the first loading stage, respectively. The parameters τ_{avg} and γ_{avg} are determined by the following expressions,

$$\tau_{avg} = \frac{\tau_{max} - \tau_{min}}{2} \tag{4.7}$$

$$\gamma_{avg} = \frac{\gamma_{max} - \gamma_{min}}{2} \tag{4.8}$$

Figure 4-26 illustrates the concepts of Equation (4.6) through Equation (4.8).

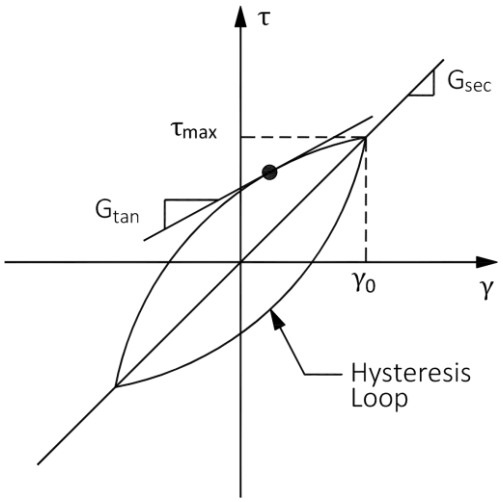

Figure 4-26: Method for determining simulated shear modulus

To develop conventional G/G_{max} degradation curves from cyclic triaxial test data, it is necessary to relate the axial strain, ε_a, applied during the cyclic triaxial test to shear strain, γ. This can be accomplished by equating the second invariant J_2 of the stress tensors for the cyclic triaxial test and simple shear test[1]. The stress tensor for an undrained cyclic triaxial test $\boldsymbol{\varepsilon}_{tx}$ is given by,

$$\boldsymbol{\varepsilon}_{tx} = \begin{bmatrix} \varepsilon_a & 0 & 0 \\ 0 & -\varepsilon_a/2 & 0 \\ 0 & 0 & -\varepsilon_a/2 \end{bmatrix} \tag{4.9}$$

The stress tensor for an undrained simple shear test $\boldsymbol{\varepsilon}_{ss}$ is given by,

$$\boldsymbol{\varepsilon}_{ss} = \begin{bmatrix} 0 & \varepsilon_{xy} & 0 \\ \varepsilon_{xy} & 0 & 0 \\ 0 & 0 & 0 \end{bmatrix} = \begin{bmatrix} 0 & \gamma/2 & 0 \\ \gamma/2 & 0 & 0 \\ 0 & 0 & 0 \end{bmatrix} \tag{4.10}$$

The second invariant for the cyclic triaxial test stress tensor, $(J_2)_{tx}$ is given by,

[1] Personal communication with A. Ghofrani, August 2015.

$$(J_2)_{tx} = \frac{1}{2}\boldsymbol{\varepsilon}_{tx}:\boldsymbol{\varepsilon}_{tx} = \frac{3}{4}{\varepsilon_a}^2 \quad \textbf{(4.11)}$$

where the colon indicates the trace of the product of adjacent tensors. The second invariant for the simple shear test stress tensor, $(J_2)_{ss}$ is given by,

$$(J_2)_{ss} = \frac{1}{2}\boldsymbol{\varepsilon}_{ss}:\boldsymbol{\varepsilon}_{ss} = {\varepsilon_{xy}}^2 = \frac{\gamma^2}{4} \quad \textbf{(4.12)}$$

If $(J_2)_{tx}$ is set as equivalent to $(J_2)_{ss}$, it can be shown that γ is equal to $\sqrt{3}\,\varepsilon_a$.

The simulated damping curves were determined for the fifth cycle of the simulated undrained cyclic triaxial test in accordance with the concept presented in Figure 2-5.

The calibrated experimental and simulated stress-strain response and stress path for each loading stage of the undrained cyclic triaxial tests on Specimen No. T2-2 and T2-4 are shown in Figure 4-27 through Figure 4-30. The plots of stress-strain response and stress path are shown for five cycles of cyclic triaxial loading.

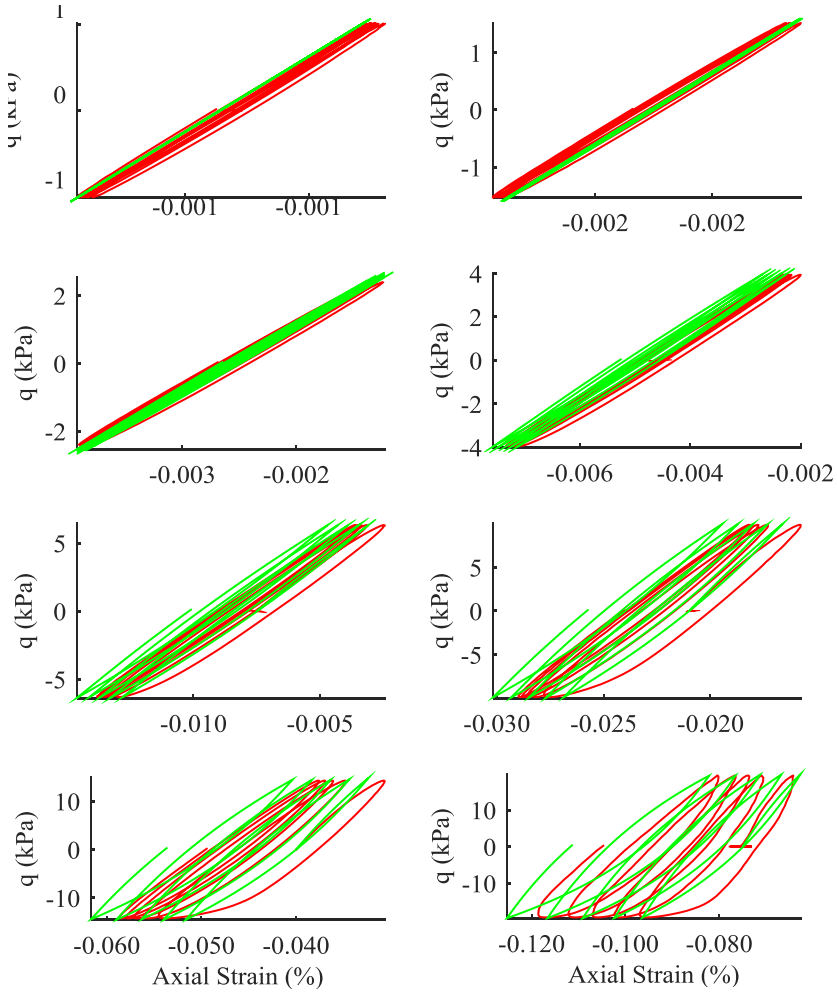

Figure 4-27: Specimen No. T2-2 deviatoric stress-axial strain calibration (green = simulation; red = laboratory)

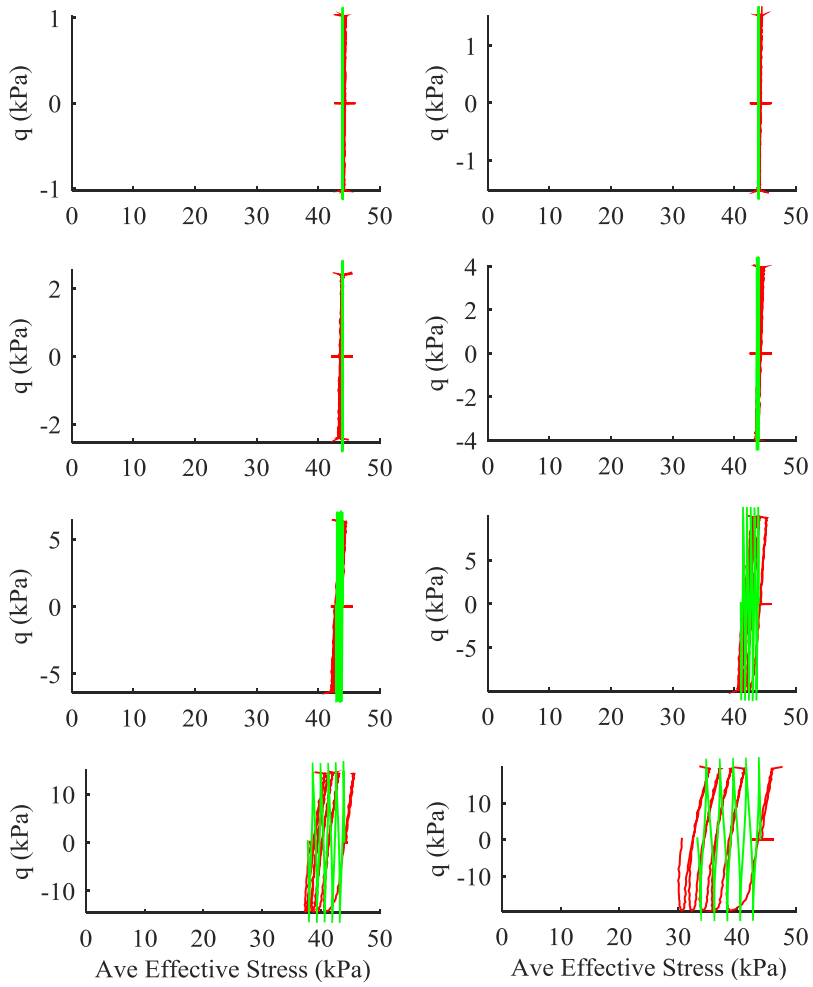

Figure 4-28: Specimen No. T2-2 deviatoric stress-average effective stress calibration (green = simulation; red = laboratory)

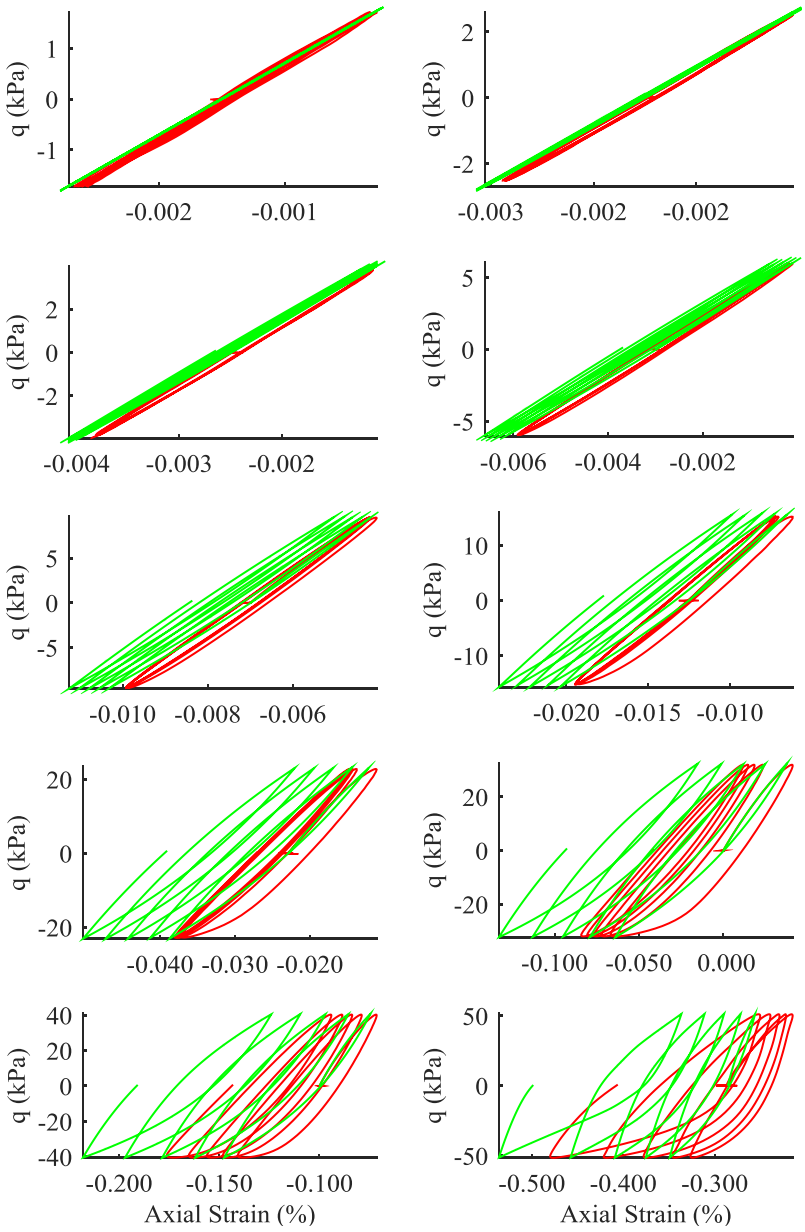

Figure 4-29: Specimen No. T2-4 deviatoric stress-axial strain calibration (green = simulation; red = laboratory)

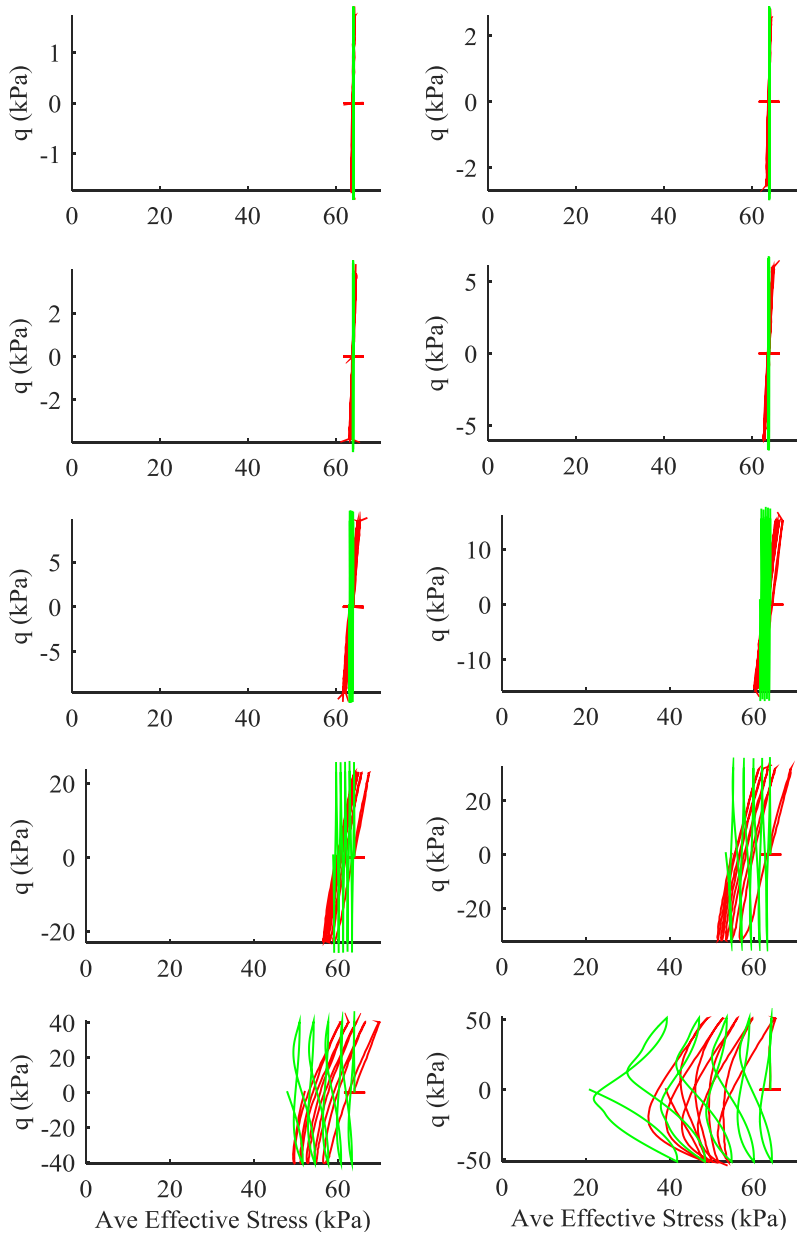

Figure 4-30: Specimen No. T2-4 deviatoric stress-mean effective stress calibration (green = simulation; red = laboratory)

The simulated shear modulus reduction and damping curves resulting from the calibration to the laboratory data are shown in Figure 4-31 and Figure 4-32. These curves are calculated based on the fifth cycle of each load step from the simulation and laboratory.

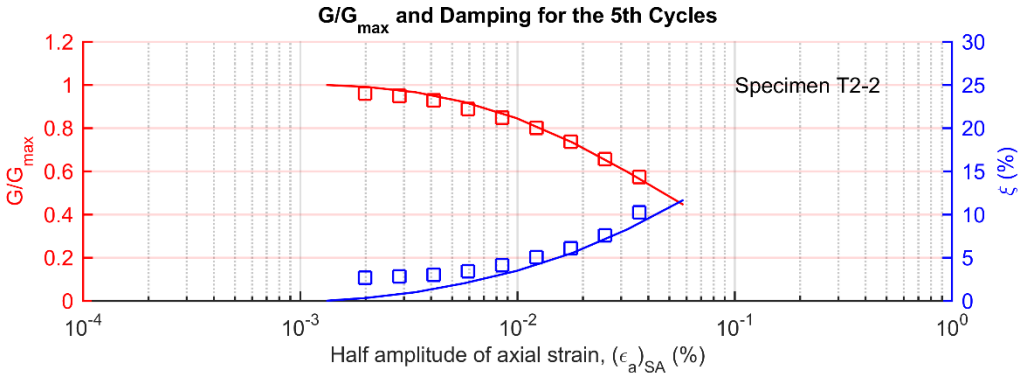

Figure 4-31: Cyclic triaxial calibration G/Gmax and damping curves for Specimen T2-2 (lines = simulation; symbols = laboratory data)

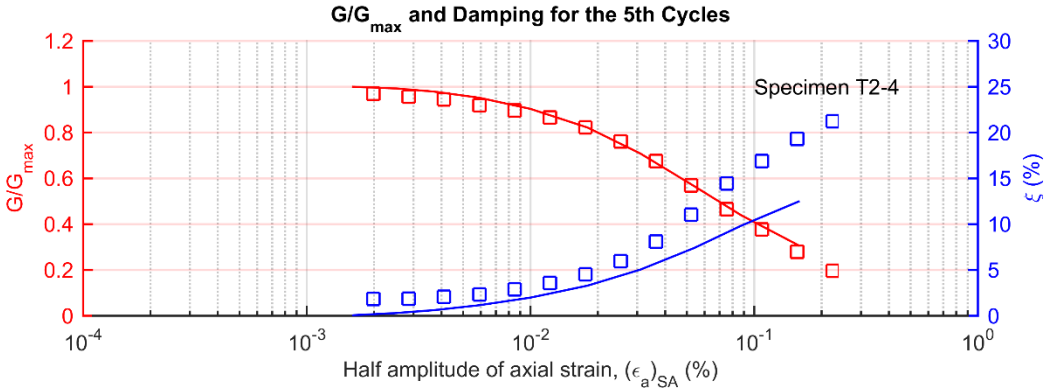

Figure 4-32: Cyclic triaxial calibration G/Gmax and damping curves for Specimen T2-4 (lines = simulation; symbols = laboratory data)

4.7.3 SANISAND Model Parameters Based on Calibration to Laboratory Data

As the SANISAND model is based on critical state soil mechanics framework, a single set of model parameters should approximate the dynamic behaviour of the sand over the depth of the Sendai site, provided that the sand is of the same origin with relatively constant characteristics. A single set of model parameters were selected to provide a match the results of the triaxial testing carried out in the laboratory on Specimen No. T2-2 (depth 2.8 – 3.8 m) and T2-4 (depth

4.9 – 5.9 m). The SANISAND model parameters calibrated to the drained monotonic and undrained cyclic triaxial tests are presented in Table 4-8.

Table 4-8: SANISAND Model Parameters Based on Undrained Cyclic Triaxial Tests

Parameter	Symbol	Value
Elasticity	G_0	125
	ν	0.05
CSL	M	1.35
	c	0.712
	e_0	0.934
	λ	0.111
	ξ	0.7
Yield Surface	m	0.02
Dilatancy	n^d	4
	A_0	0.5
Plastic Modulus	n^b	1.25
	h_0	16
	c_h	0.968
Fabric Dilatancy	z_{max}	15
	c_z	2400

4.7.4 G_0 Constant for Seismic Ground Response Analysis

The small-strain shear modulus values determined from the laboratory undrained cyclic triaxial tests ($G_{max\text{-}lab}$) are presented in Table 4-9, along with the small-strain shear modulus values calculated from the in-situ shear wave velocity ($G_{max\text{-}field}$) and the total mass density at the depths corresponding to Specimen No. T2-2 and T2-4.

Table 4-9: Gmax determined experimentally and from in-situ Vs

Soil Sample	$G_{max\text{-}lab}$ (MPa)	$G_{max\text{-}field}$ (MPa)	$G_{max\text{-}lab}/G_{max\text{-}field}$
T2-2 (2.8 – 3.8 m)	25	100	0.25
T2-4 (4.9 – 5.9 m)	37	148	0.25

Based on the $G_{max\text{-}lab}/G_{max\text{-}field}$ ratio of the values presented in Table 4-9, the maximum shear modulus values determined from the cyclic triaxial tests are less than the field in situ values by a factor of approximately four. Figure 4-33 compares the shear modulus reduction curves simulated using the SANISAND model when the G_0 parameter of the model is calibrated using the small strain data of the cyclic triaxial laboratory data on Specimen T2-2, and when the G_0 parameter is calibrated using the situ measurement of G_{max} based on shear wave velocity at the sampling depth of Specimen T2-2.

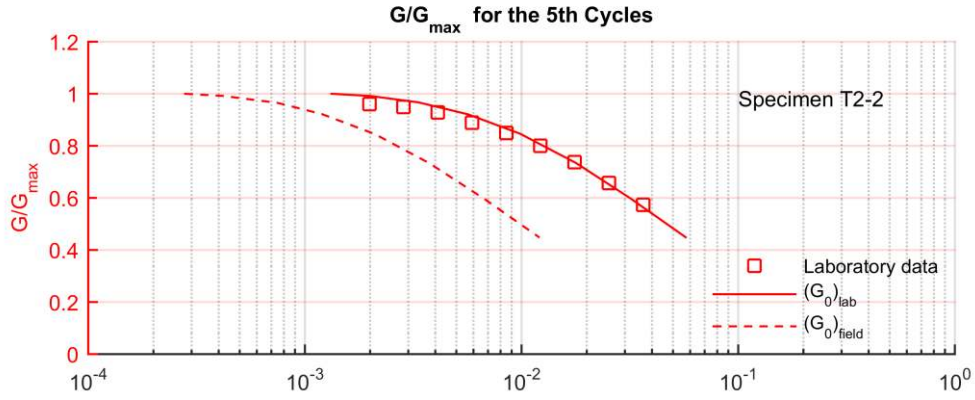

Figure 4-33: Effect of G_0 calibration on G/Gmax curves

As can be observed in Figure 4-33, the method of determining G_{max} for the calibration of the G_0 model parameter has a significant effect on the simulated cyclic response of the sand soils. Ishihara (1996) showed that the small strain shear modulus determined in the laboratory and by in situ measurements can differ greatly. The difference between the laboratory and field small-strain shear modulus values may result from a number of factors, including the following:

- Soil specimen disturbance during freezing and sampling, transportation, and thawing for the laboratory testing.
- Conventional triaxial tests are unable to measure stiffness within the range of very small strain where G_{max} exists.

- The level of strain induced at the determination of shear modulus. Shear waves induce very small strains (in the order of less than 10^{-4}%) when advanced through a soil body for the determination of shear wave velocity and maximum shear modulus in the field (Howie and Campanella, 2005). In contrast, the small strain shear modulus determined from the laboratory data was extrapolated from data collected on the fifth cycle of the first loading stage of an undrained cyclic triaxial test (OYO, 2014). Since the laboratory specimen had already been subjected to four hysteretic cycles prior to determining the small-strain shear modulus on the fifth cycle, the level of strain induced in the laboratory specimen would be greater than the level of strain when V_s was determined in the field.
- The shear wave velocity measured in the field was done so with the downhole method. The in situ measurement of field shear wave velocity will encompass a body of soil which is much larger than the soil specimen tested in the laboratory. This is expected to result in some discrepancy between the in situ and laboratory small strain shear modulus.
- Triaxial tests do not actually measure shear modulus; but rather measures the axial strain to evaluate the elastic modulus, which can then be used to calculate shear modulus using an assumed Poisson's ratio. The Poisson's ratio for the undrained cyclic triaxial tests has been assumed to be 0.5, corresponding to an undrained condition. However, this may present some inaccuracy in the determination of laboratory shear modulus, if the triaxial test is not truly undrained.

Disturbance of the soil samples and the difference between the level of strain induced in the soil during the laboratory and field determination of the small strain shear modulus are considered to be the primary cause of the discrepancy between the laboratory and field small-strain shear modulus values in Table 4-9. The small-strain shear modulus considered for calibration of the SANISAND model has an influence on the nonlinear behavior of the soil when subjected to earthquake motions. Therefore, the SANISAND G_0 constant needs careful consideration when calibrating the model.

If calibration of the SANISAND model considers only the cyclic triaxial data (and consequently a shear modulus which is small relative to the field measurements), then the fundamental ground response will not be captured during a seismic ground response analysis, as the site soils are being modeled as "softer" than is indicated by the field shear wave velocities. Based on the above, the SANISAND G_0 constant was calibrated over 1 m intervals to the in situ measurement of shear wave velocity at the Sendai site in order to adequately capture the in situ stiffness of the site soils. The G_0 values are presented in Table 4-10.

Table 4-10: G_0 constants determined from in situ Vs measurements

Parameter	Depth (m)	Value
Elasticity – G_0	0 - 1	420
	1 - 2	490
	2 - 3	590
	3 - 4	600
	4 - 5	700
	5 - 6	750
	6 - 7	810

4.8 Simulation Results

In this section the results of the total and effective stress seismic ground response analyses carried out for the Sendai site are presented. The parameters acceleration, porewater pressure (for the effective stress analyses), stress and strain were recorded along the soil profile during the analyses.

4.8.1 Seismic Ground Response Using Effective Stress Analyses

The simulation results for the effective stress ground response analyses are presented in Figure 4-34 through Figure 4-42. The effective stress analysis results presented include the following:

- East-west horizontal acceleration time history simulated at the surface of the site and input at the base of the site profile, along with east-west horizontal acceleration time history recorded at the Sendai site surface seismograph;

- The pore pressure time history simulated at 2 m depth intervals over the soil profile;
- The east-west horizontal acceleration response spectra with a damping ratio of $\xi = 5\%$ simulated at the surface of the site and input at the base of the site profile, along with the acceleration response spectra for the east-west horizontal motion recorded at the site surface seismograph; and
- The stress-strain loops simulated at 2 m intervals over the soil profile.

In the figures below, z refers to the site depth, as indicated on Figure 4-1.

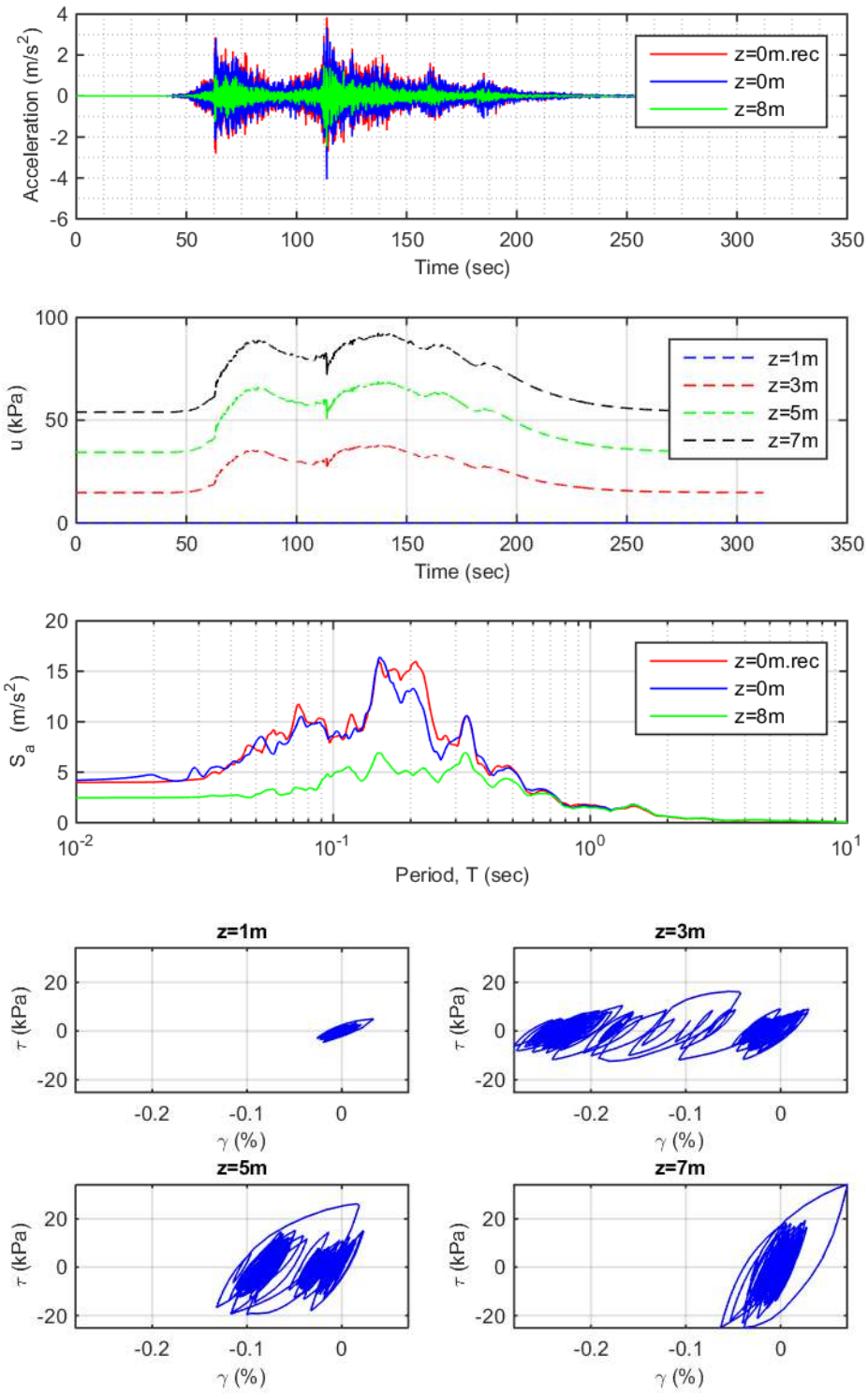

Figure 4-34: TS1 effective stress acceleration and pore pressure time history, acceleration response spectra (5 percent damping), and stress-strain loops

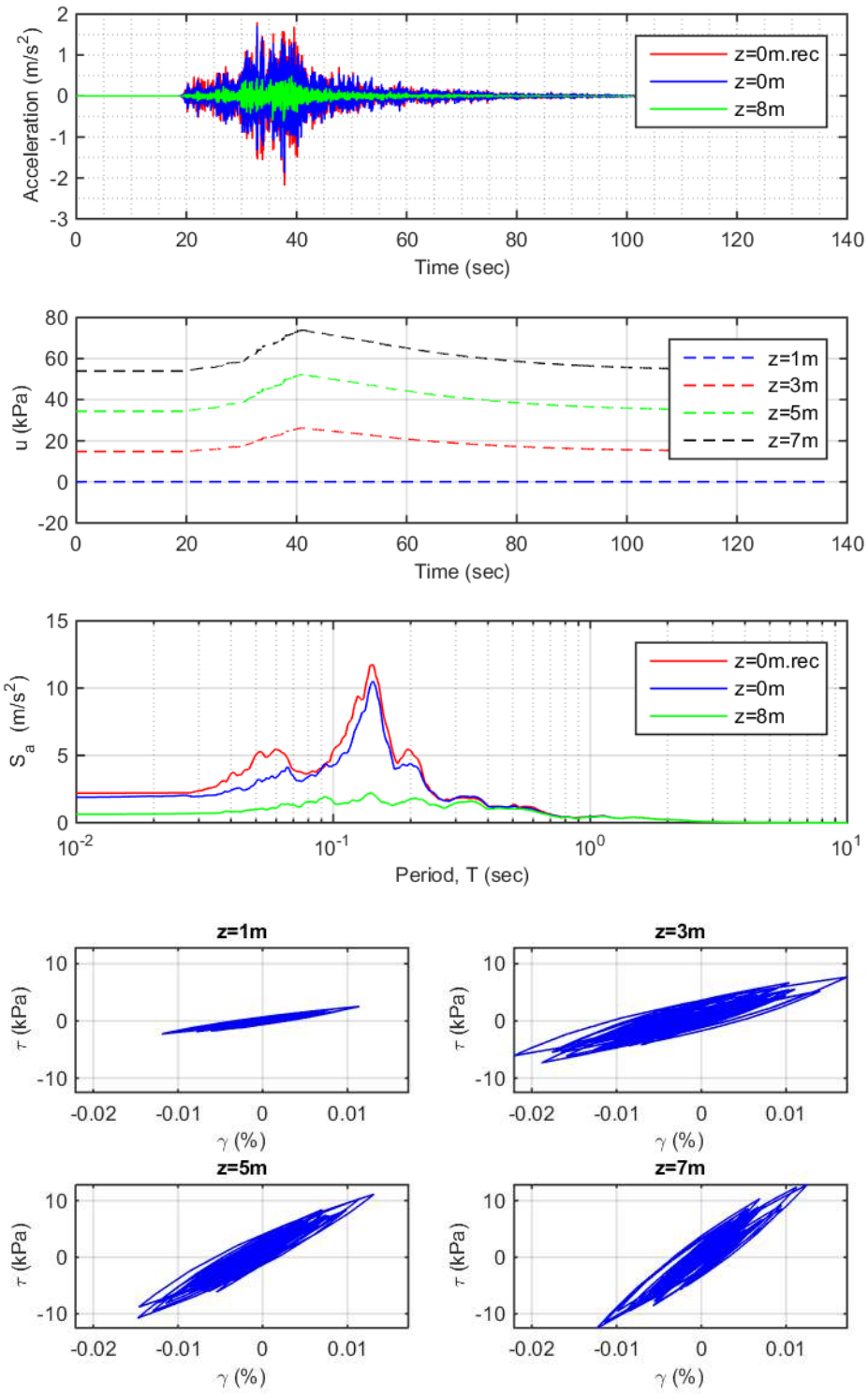

Figure 4-35: TS2 effective stress acceleration and pore pressure time history, acceleration response spectra (5 percent damping), and stress-strain loops

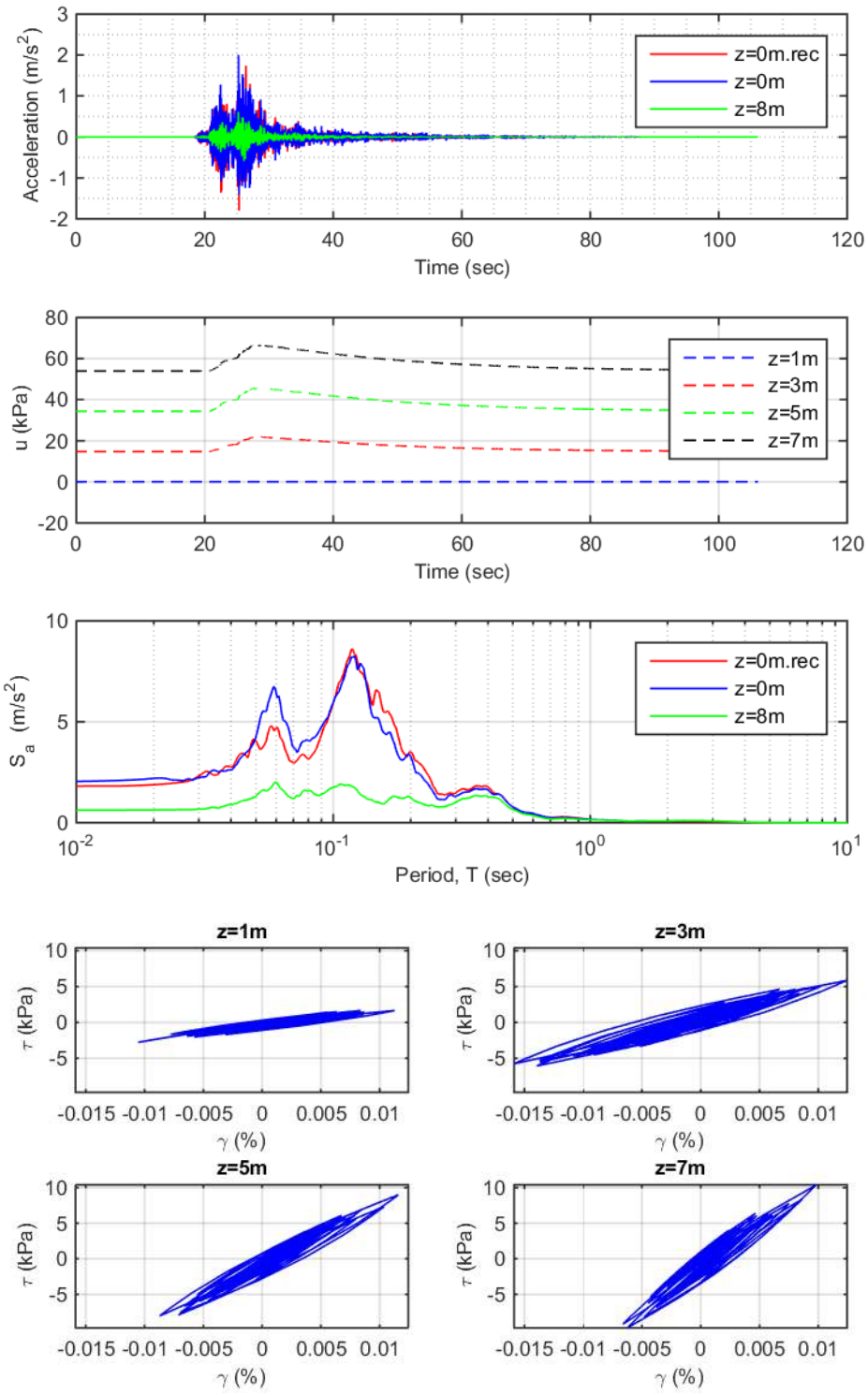

Figure 4-36: TS3 effective stress acceleration and pore pressure time history, acceleration response spectra (5 percent damping), and stress-strain loops

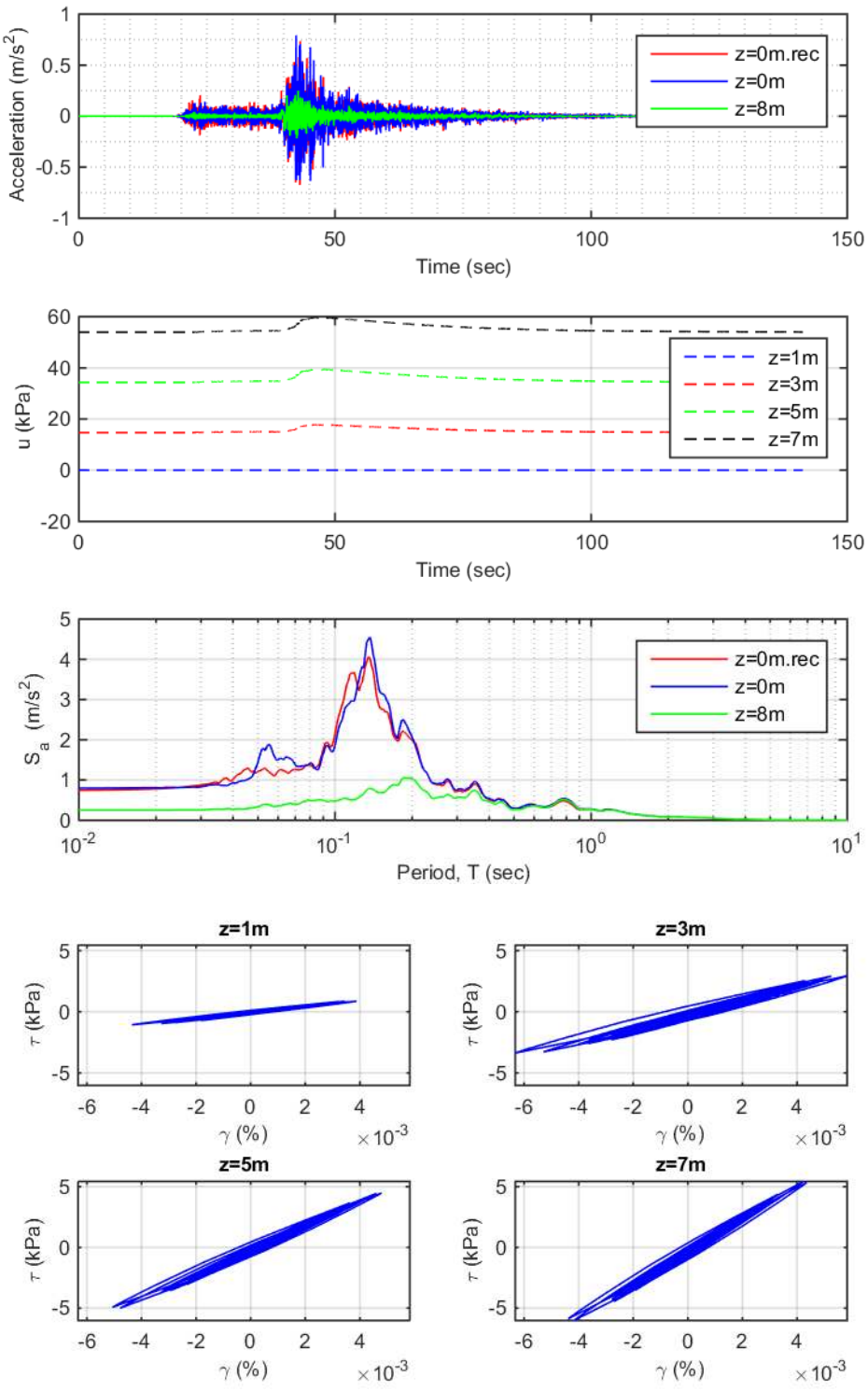

Figure 4-37: TS4 effective stress acceleration and pore pressure time history, acceleration response spectra (5 percent damping), and stress-strain loops

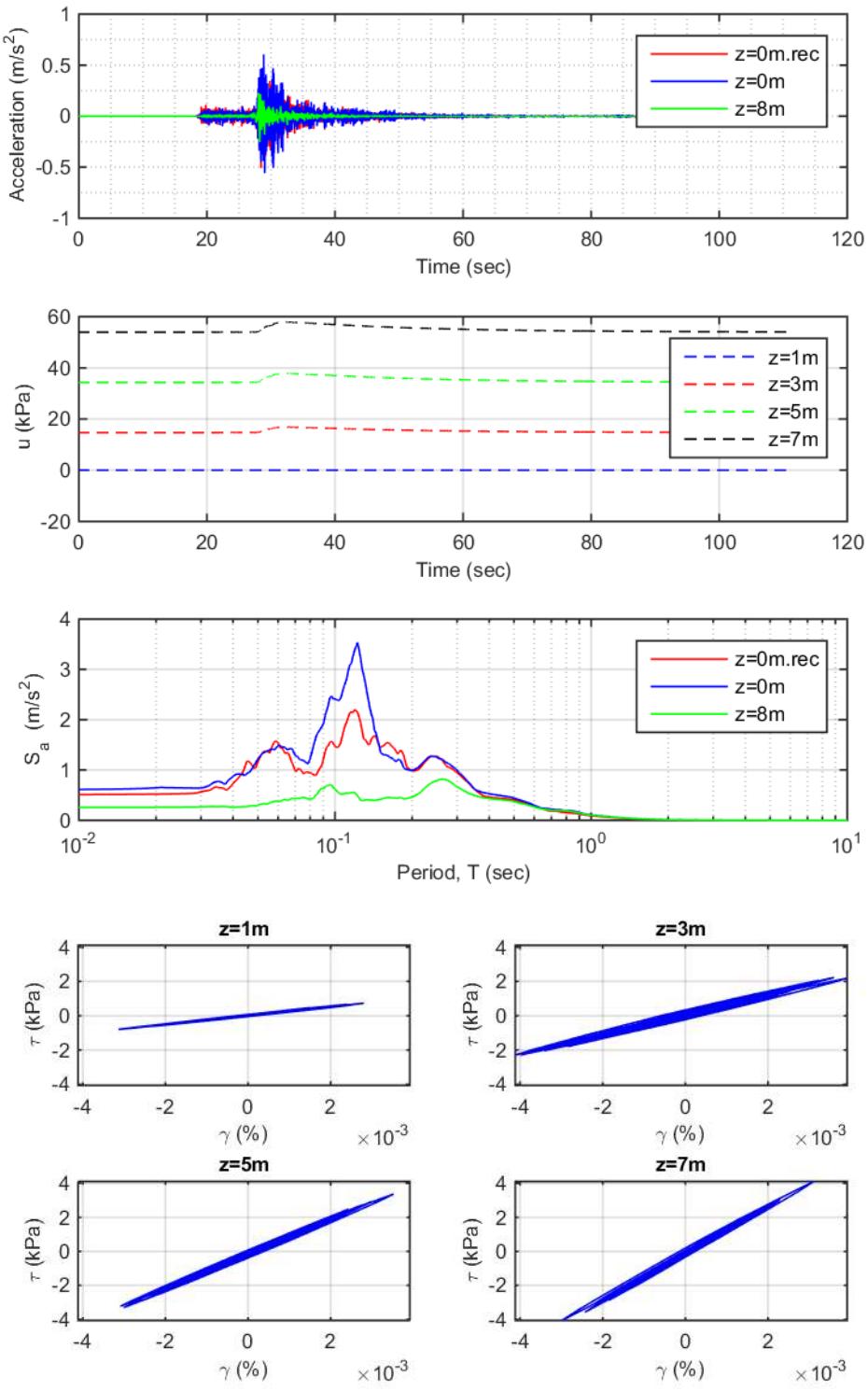

Figure 4-38: TS5 effective stress acceleration and pore pressure time history, acceleration response spectra (5 percent damping), and stress-strain loops

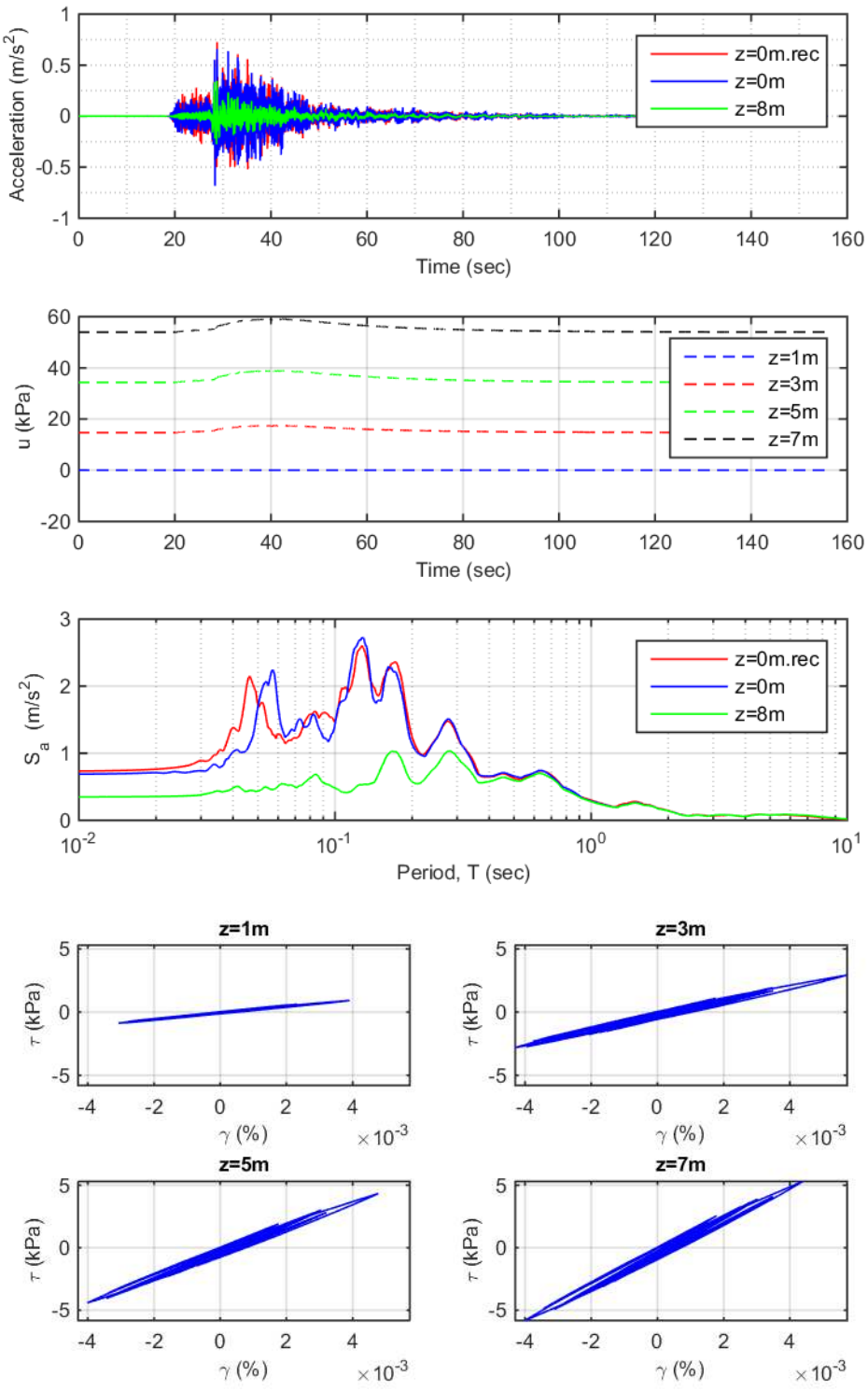

Figure 4-39: TS6 effective stress acceleration and pore pressure time history, acceleration response spectra (5 percent damping), and stress-strain loops

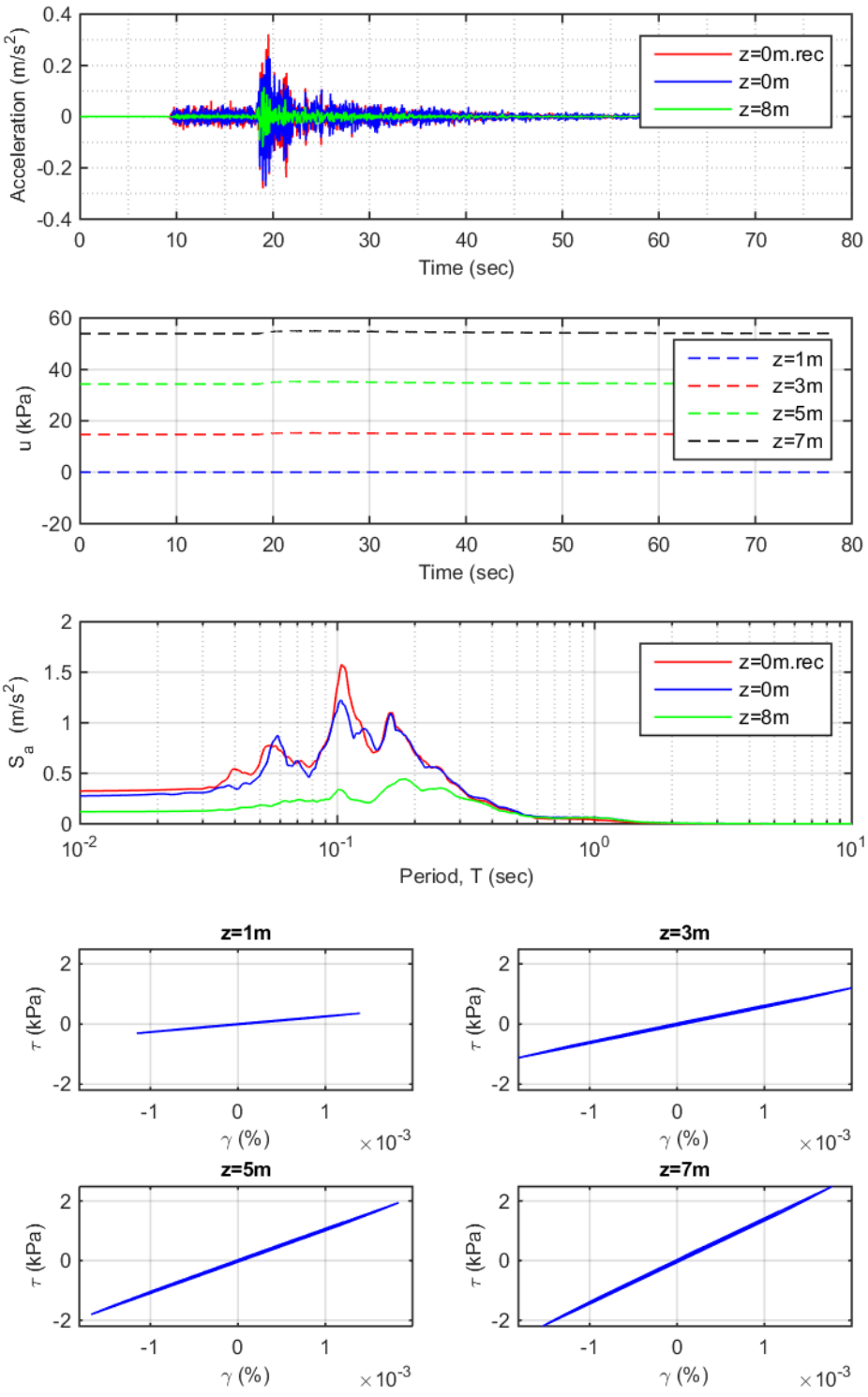

Figure 4-40: TS7 effective stress acceleration and pore pressure time history, acceleration response spectra (5 percent damping), and stress-strain loops

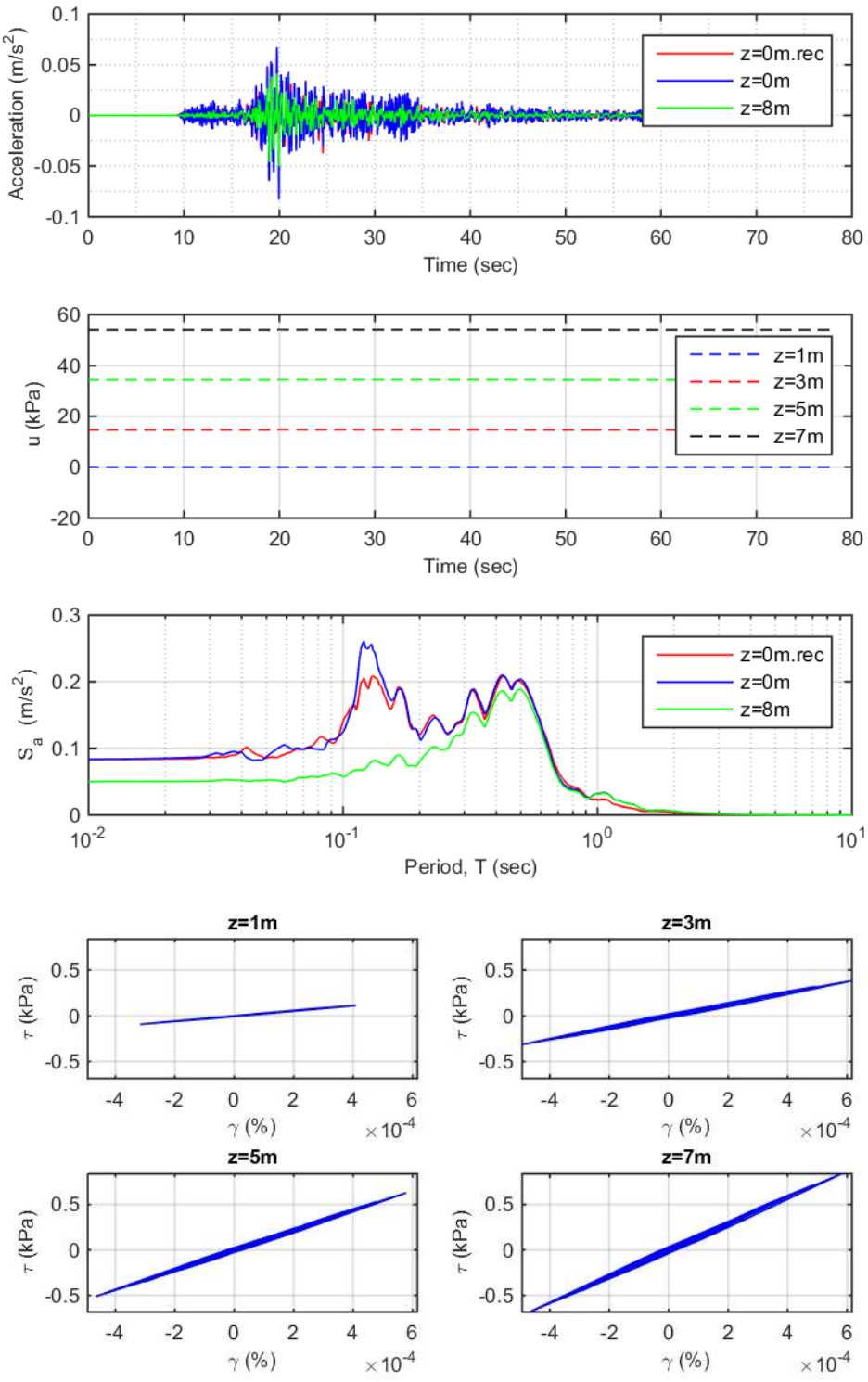

Figure 4-41: TS8 effective stress acceleration and pore pressure time history, acceleration response spectra (5 percent damping), and stress-strain loops

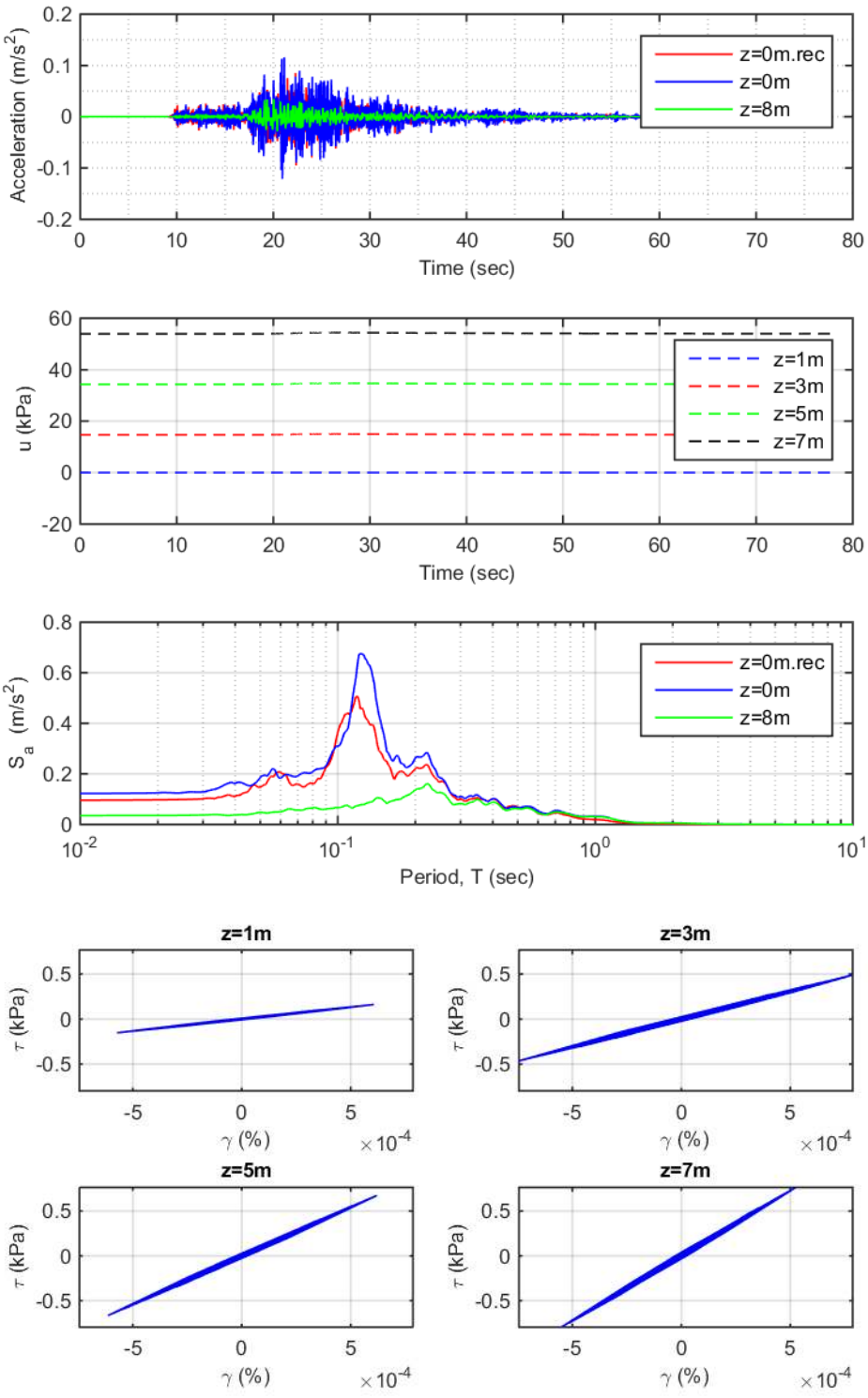

Figure 4-42: TS9 effective stress acceleration and pore pressure time history, acceleration response spectra (5 percent damping), and stress-strain loops

It should be noted that after completion of the effective stress analyses presented in Figure 4-34 through Figure 4-42 (with the downhole seismograph located at 1 m into the slate bedrock), the PRENOLIN organizing team revised the location of the downhole seismograph to approximately 3.4 m into the slate bedrock. The depth and characterization of the sand soils overtop of the bedrock, which are the focus of this research, remain unchanged. The deeper location of the downhole seismograph does not significantly change the ground response of the 7 m of sand soils overlying the bedrock, and the conclusions drawn based on the effective stress analysis results presented for the 8 m site are considered to be applicable. This is shown to be the case in Figure 4-43 through Figure 4-51 by repeating the analyses presented in Figure 4-34 through Figure 4-42 with the input motion applied at 3.5 m into the bedrock (z=10.5m), and comparing the ground surface acceleration response spectra (damping ratio ξ=5%) for this site geometry with the results from the original site geometry (input motion at z=8 m).

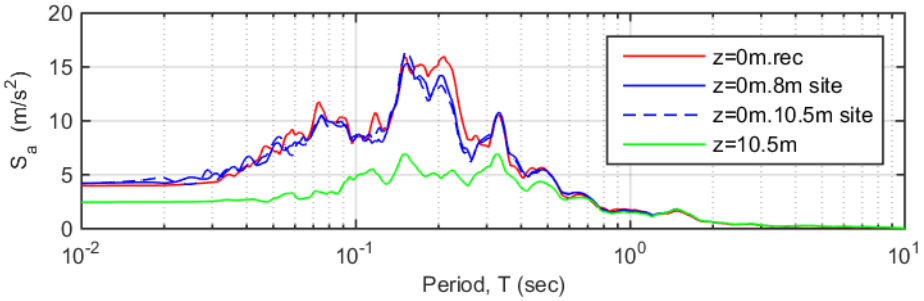

Figure 4-43: TS1 effective stress acceleration response spectra (5 percent damping) for seismograph located 1 m and 2.5 m into bedrock

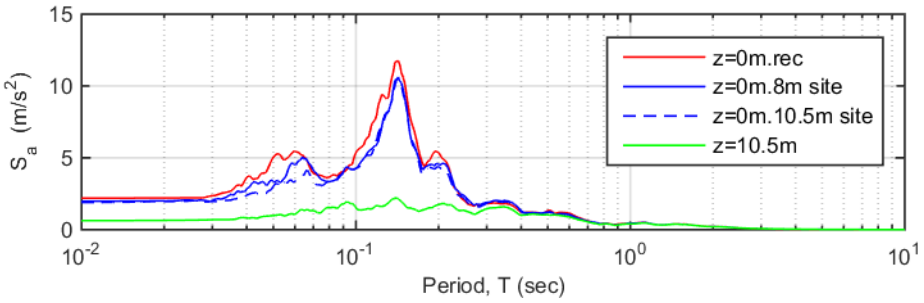

Figure 4-44: TS2 effective stress acceleration response spectra (5 percent damping) for seismograph located 1 m and 2.5 m into bedrock

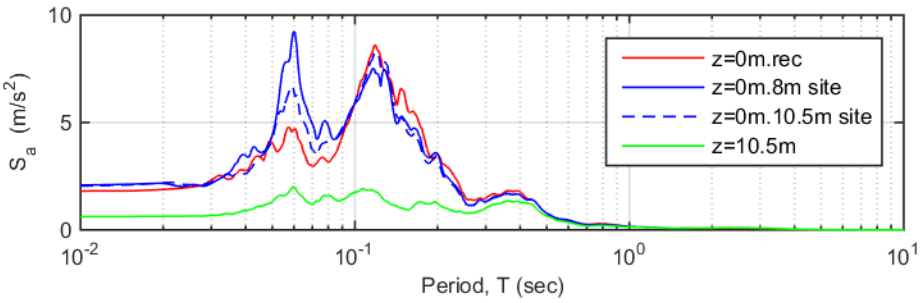

Figure 4-45: TS3 effective stress acceleration response spectra (5 percent damping) for seismograph located 1 m and 2.5 m into bedrock

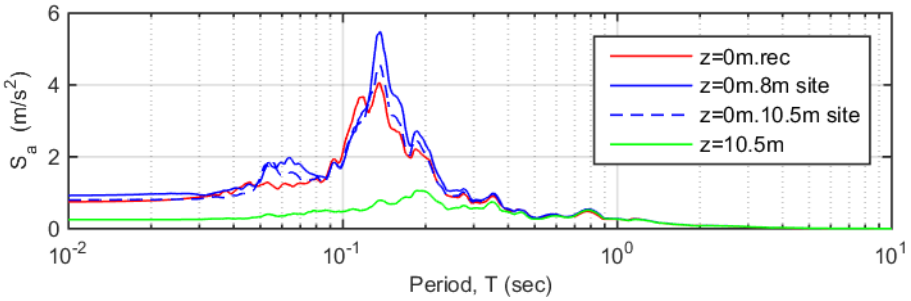

Figure 4-46: TS4 effective stress acceleration response spectra (5 percent damping) for seismograph located 1 m and 2.5 m into bedrock

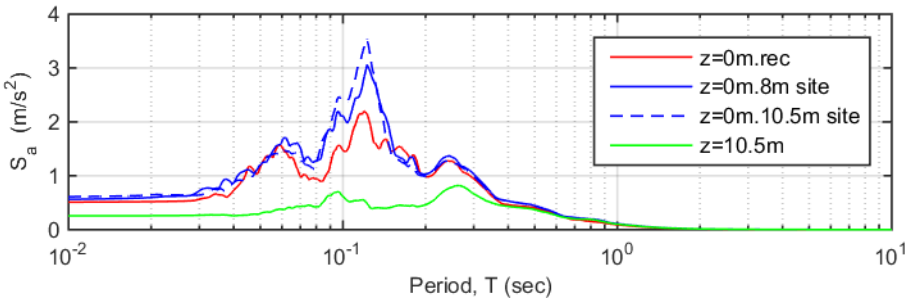

Figure 4-47: TS5 effective stress acceleration response spectra (5 percent damping) for seismograph located 1 m and 2.5 m into bedrock

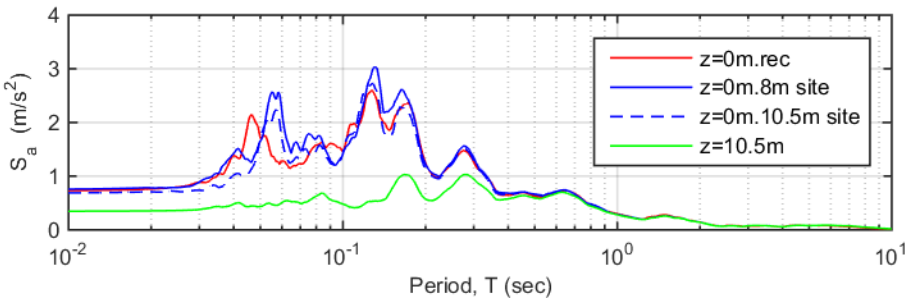

Figure 4-48: TS6 effective stress acceleration response spectra (5 percent damping) for seismograph located 1 m and 2.5 m into bedrock

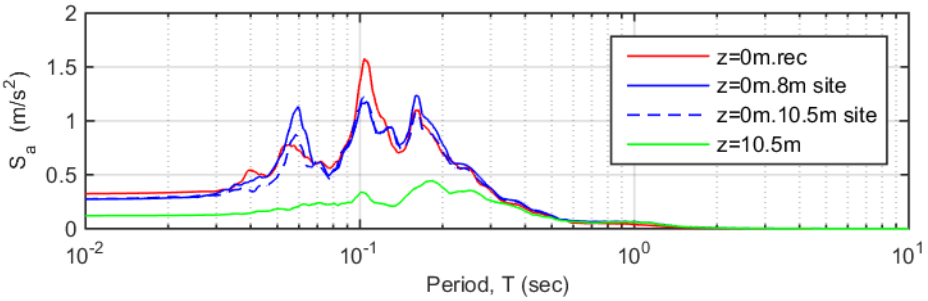

Figure 4-49: TS7 effective stress acceleration response spectra (5 percent damping) for seismograph located 1 m and 2.5 m into bedrock

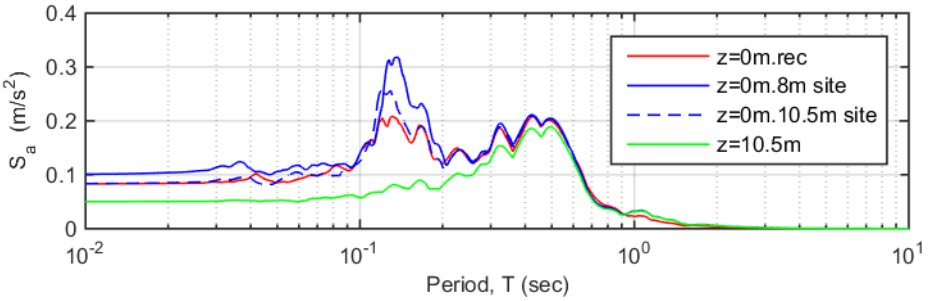

Figure 4-50: TS8 effective stress acceleration response spectra (5 percent damping) for seismograph located 1 m and 2.5 m into bedrock

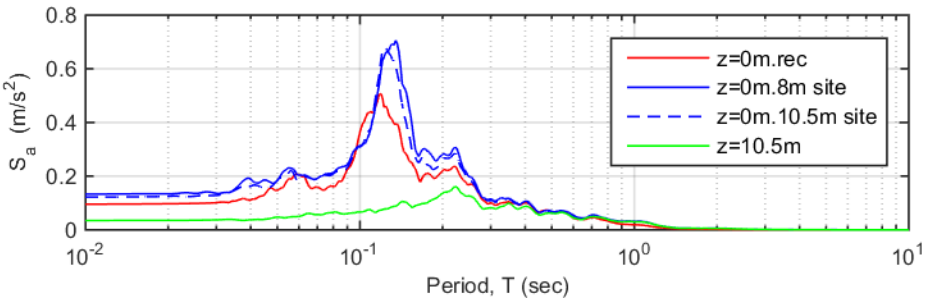

Figure 4-51: TS9 effective stress acceleration response spectra (5 percent damping) for seismograph located 1 m and 2.5 m into bedrock

As can be observed in Figure 4-43 through Figure 4-51, the effective stress acceleration response spectra simulated for the site configurations with the seismograph located 1 m and 3.5 m into bedrock is approximately the same, with some slight improvements in match between the recorded and simulated surface ground motions during TS3, TS4 and TS8 occurring when the downhole seismograph is located at 3.5 m into the slate bedrock.

4.8.2 Seismic Ground Response Using Total Stress Analyses

The simulation results for the total stress seismic ground response analyses are presented in Figure 4-52 through Figure 4-60. The total stress analysis results presented include the following:

- East-west horizontal acceleration time history simulated at the surface of the site and input at the base of the site profile, along with east-west horizontal acceleration time history recorded at the Sendai site surface seismograph;
- The east-west horizontal acceleration response spectra with a damping ratio of $\xi = 5\%$ simulated at the surface of the site and input at the base of the site profile, along with the acceleration response spectra for the east-west horizontal motion recorded at the site surface seismograph; and
- The stress-strain loops simulated at 2 m intervals over the soil profile.

In the figures below, z refers to the site depth, as indicated on Figure 4-1.

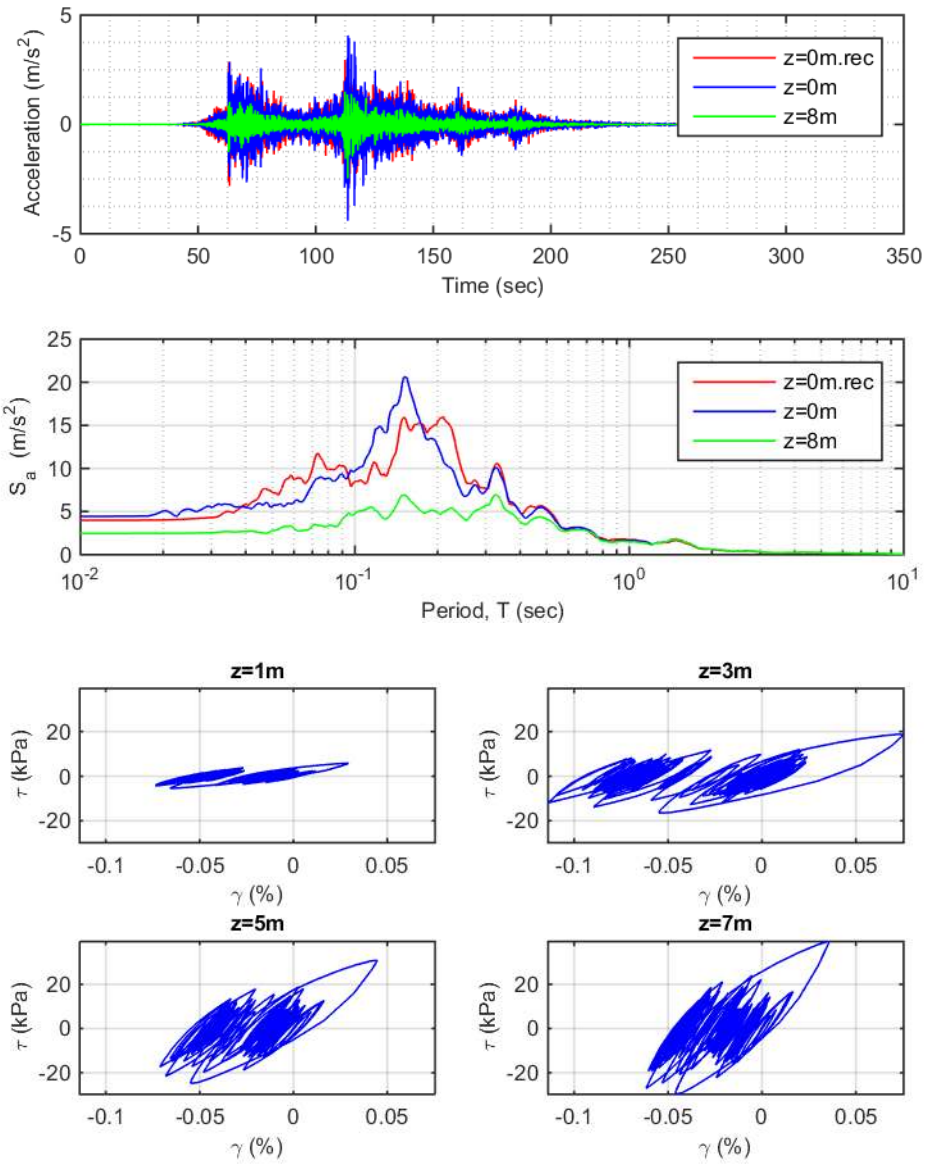

Figure 4-52: TS1 total stress acceleration time history, acceleration response spectra (5 percent damping), and stress-strain loops

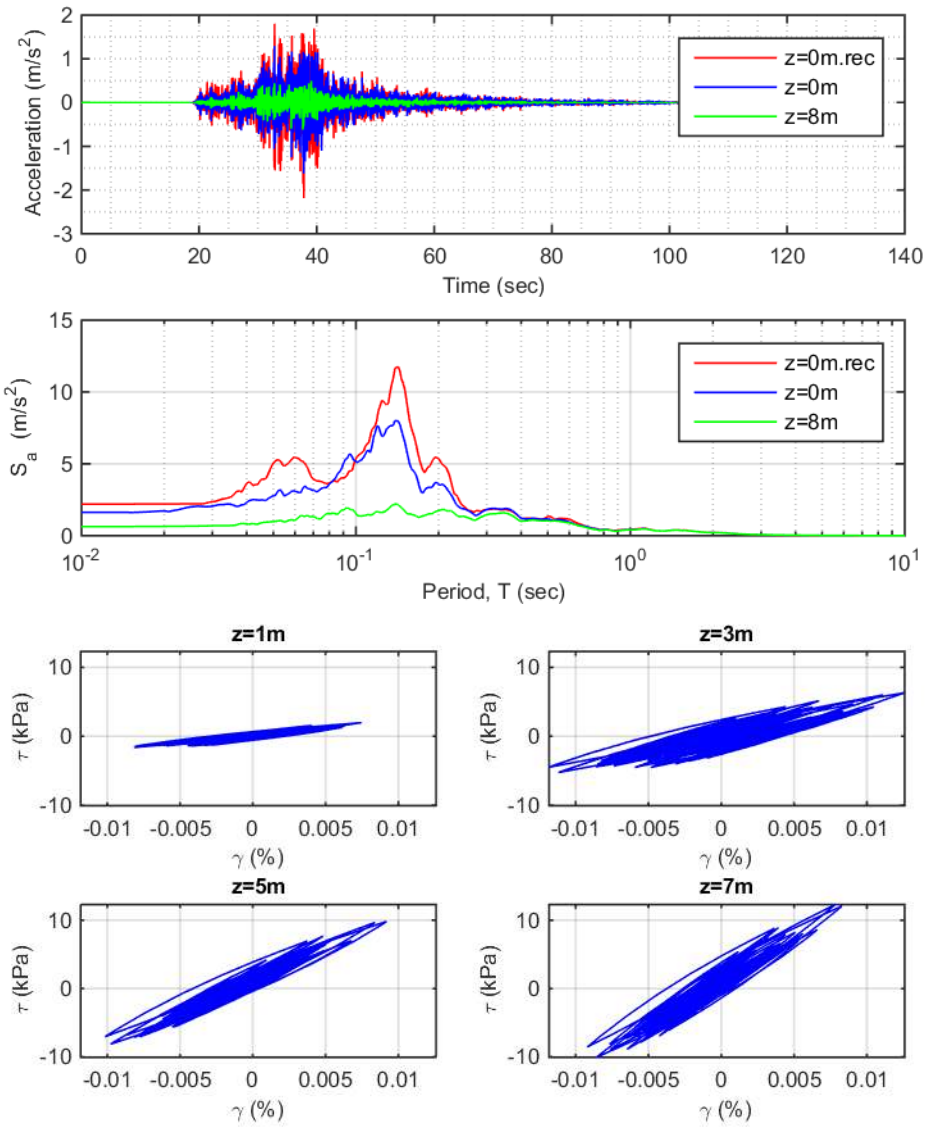

Figure 4-53: TS2 total stress acceleration time history, acceleration response spectra (5 percent damping), and stress-strain loops

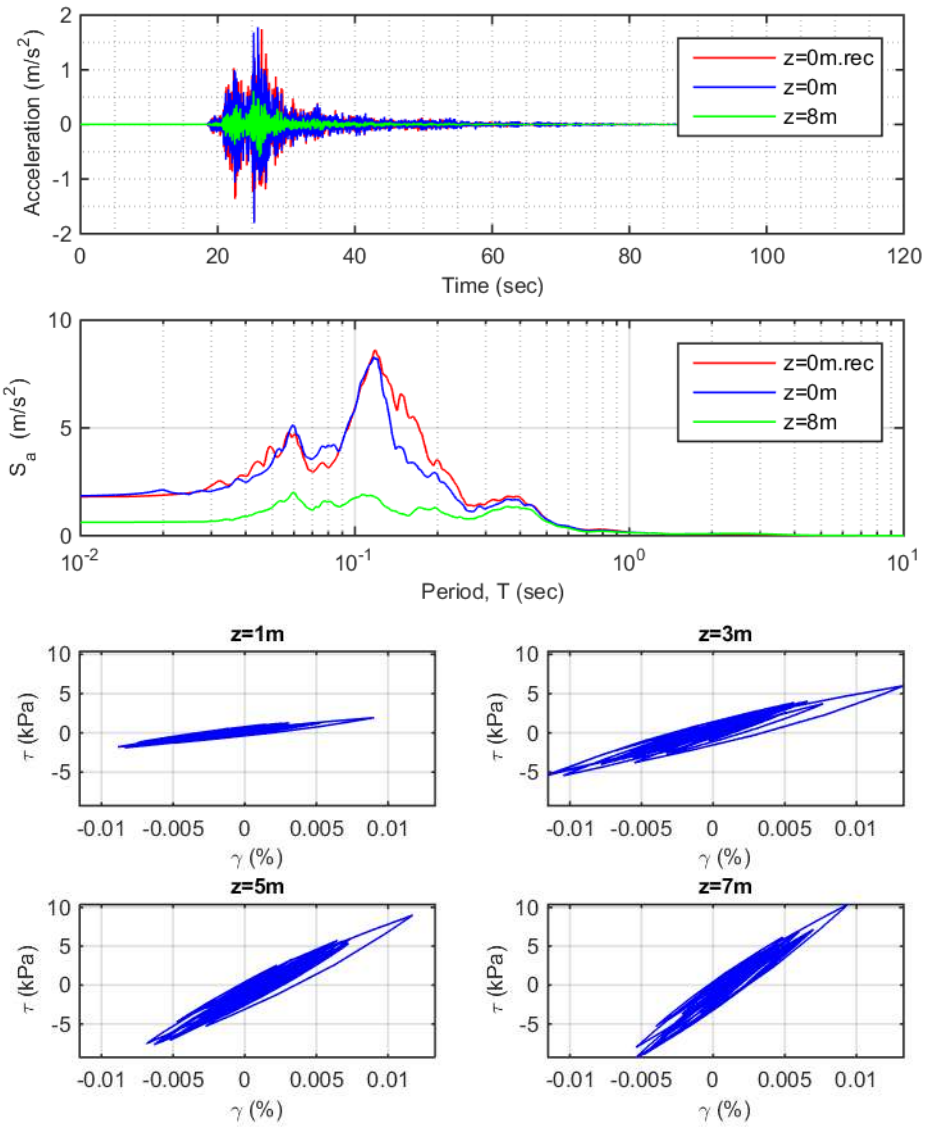

Figure 4-54: TS3 total stress acceleration time history, acceleration response spectra (5 percent damping), and stress-strain loops

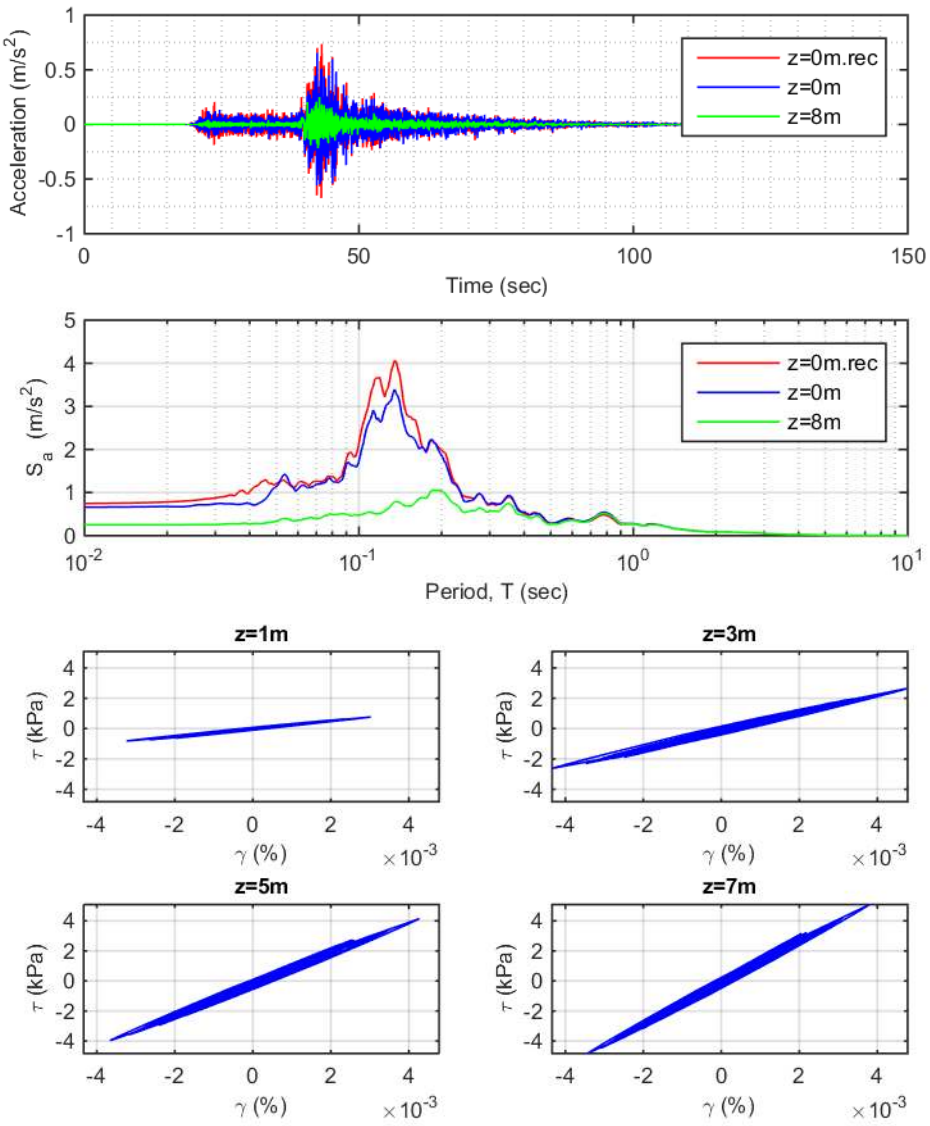

Figure 4-55: TS4 total stress acceleration time history, acceleration response spectra (5 percent damping), and stress-strain loops

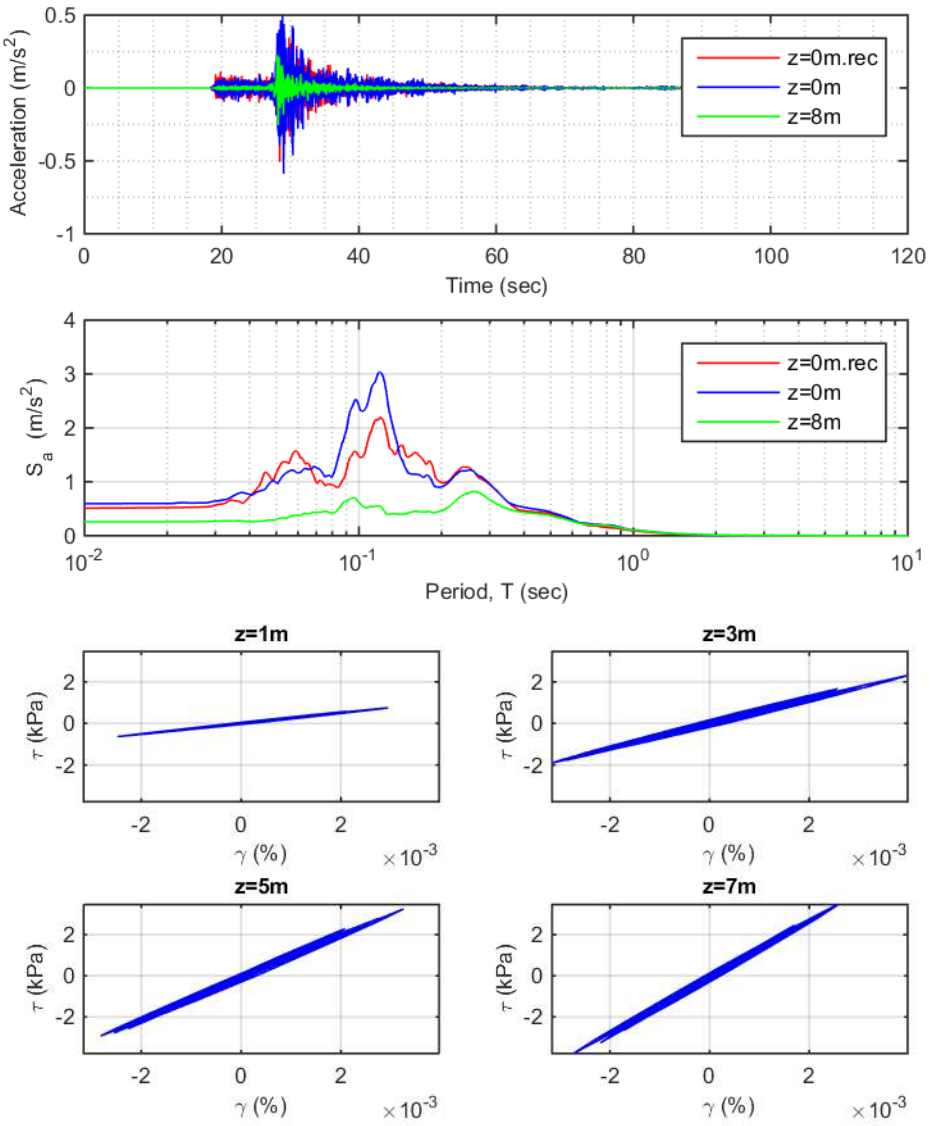

Figure 4-56: TS5 total stress acceleration time history, acceleration response spectra (5 percent damping), and stress-strain loops

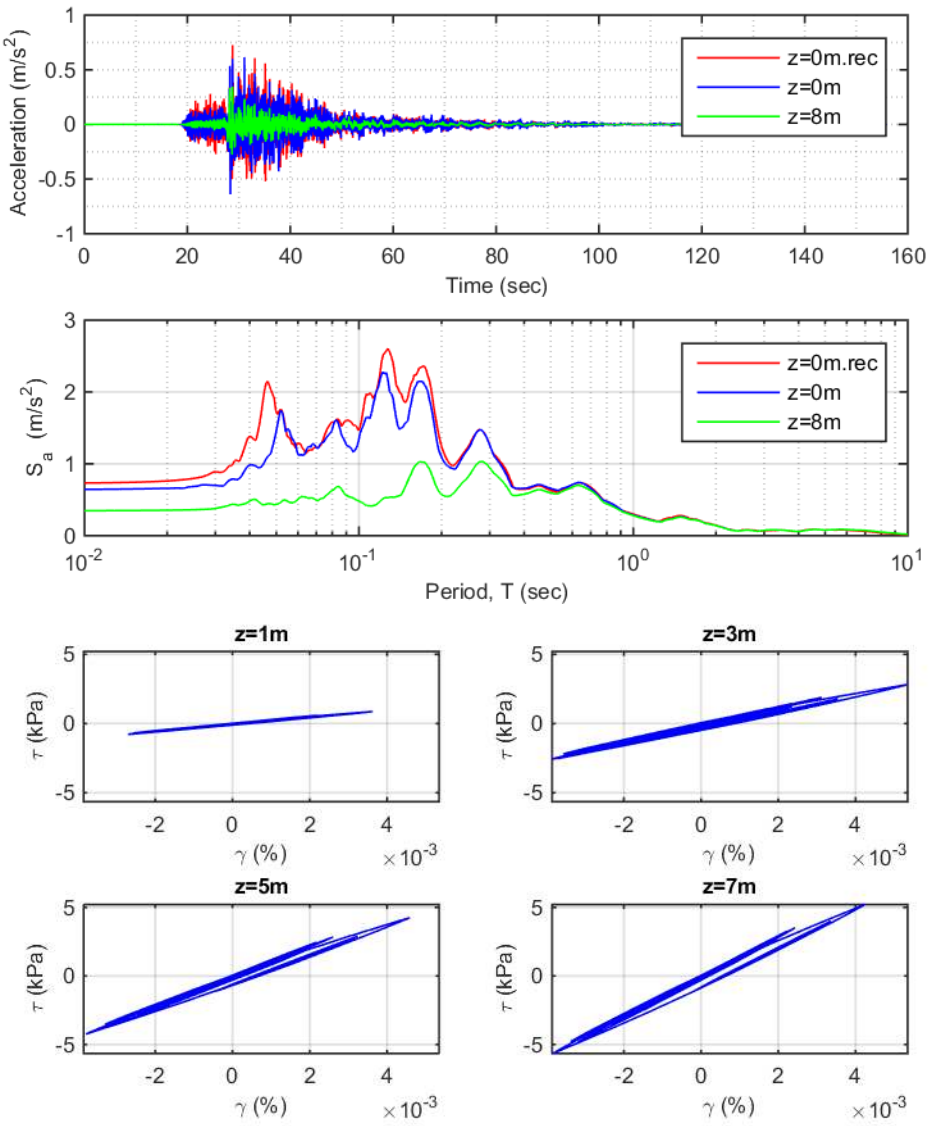

Figure 4-57: TS6 total stress acceleration time history, acceleration response spectra (5 percent damping), and stress-strain loops

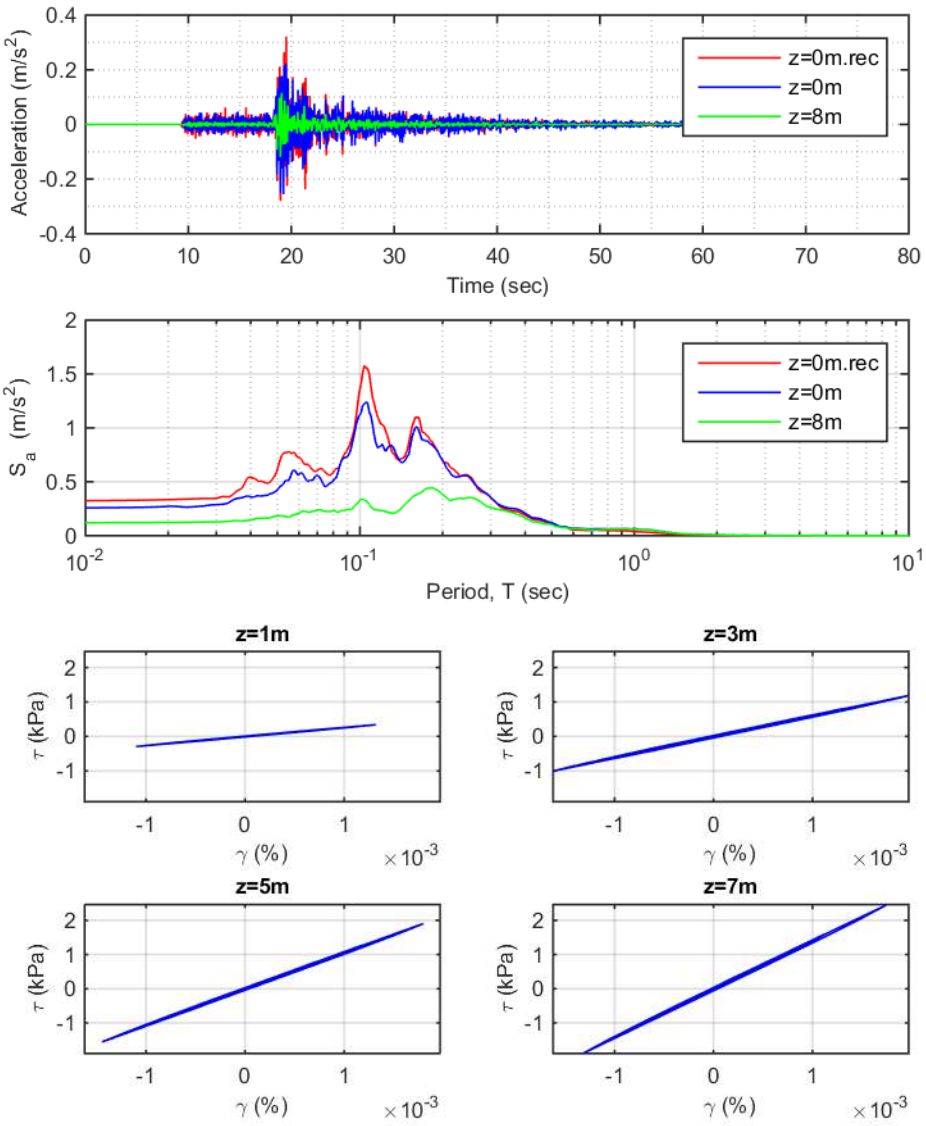

Figure 4-58: TS7 total stress acceleration time history, acceleration response spectra (5 percent damping), and stress-strain loops

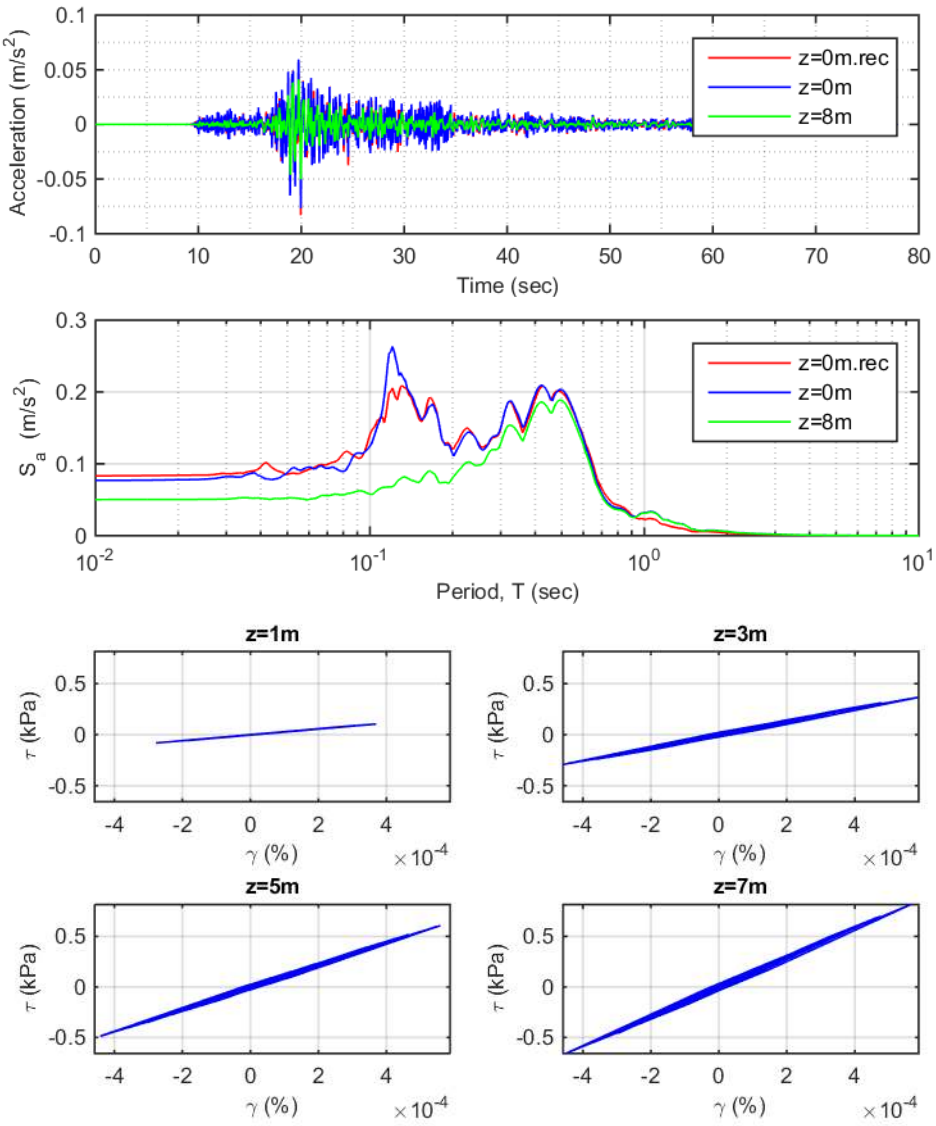

Figure 4-59: TS8 total stress acceleration time history, acceleration response spectra (5 percent damping), and stress-strain loops

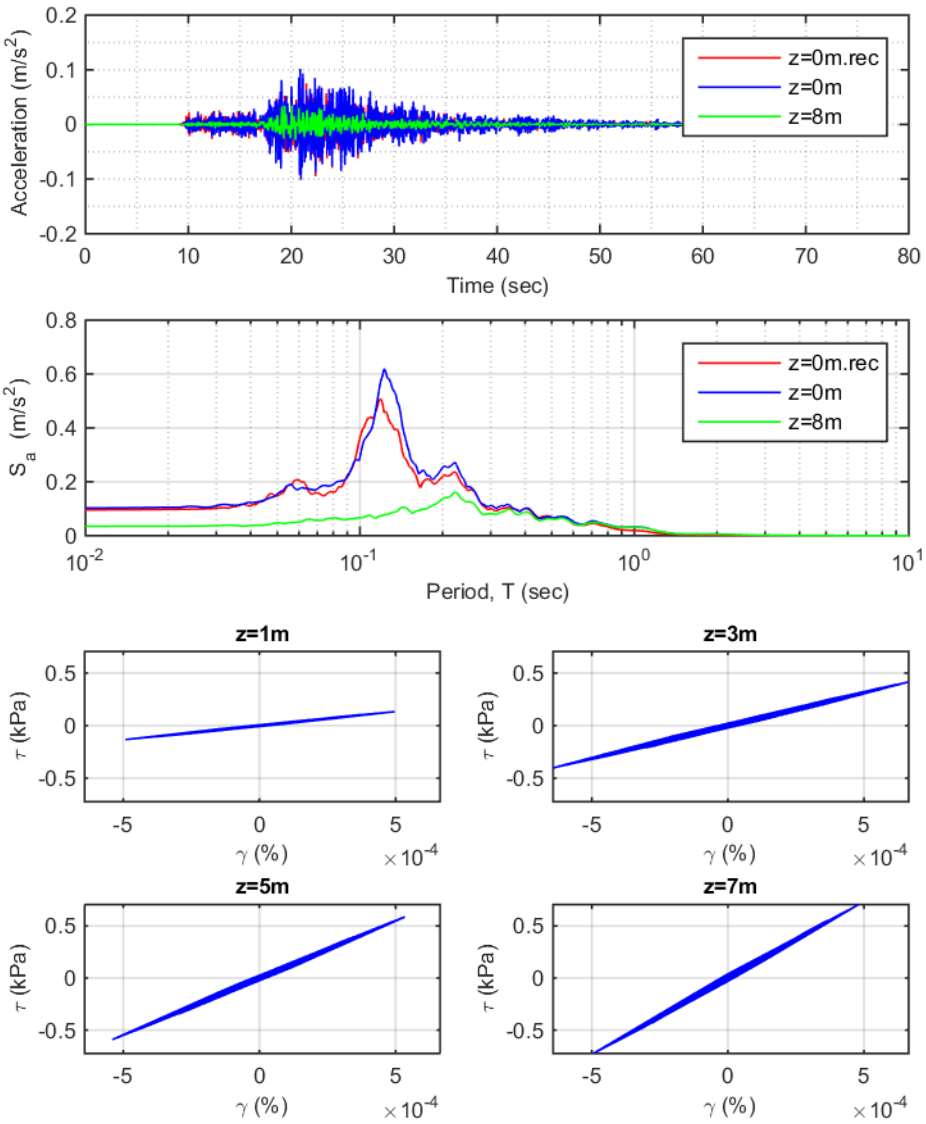

Figure 4-60: TS9 total stress acceleration time history, acceleration response spectra (5 percent damping), and stress-strain loops

As similarly described for the effective stress analyses in Section 4.8.1, after completion of the total stress analyses presented in Figure 4-52 through Figure 4-60 (with the downhole seismograph located at 1 m into the slate bedrock), the PRENOLIN organizing team revised the location of the downhole seismograph to approximately 3.4 m into the slate bedrock. The deeper location of the downhole seismograph does not significantly change the total stress ground response of the 7 m of sand soils overlying the bedrock, and the conclusions drawn based on the results presented for the 8 m deep site are considered to be applicable.

Figure 4-61 through Figure 4-69 compare the ground surface total stress acceleration response spectra (damping ratio of $\xi = 5\%$) simulated for the input motion applied at 3.5 m into the bedrock (z = 10.5m) and 1 m into the bedrock (z = 8 m).

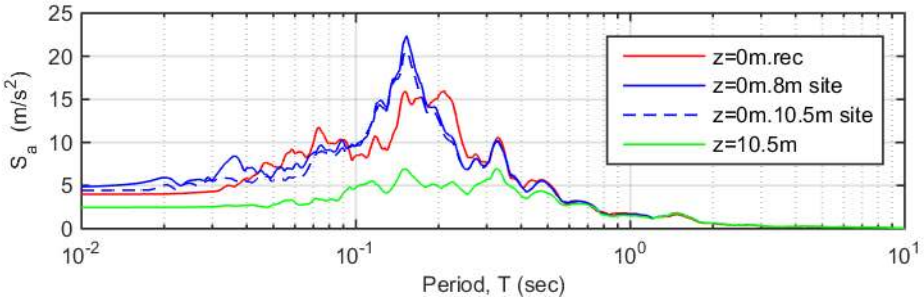

Figure 4-61: TS1 total stress acceleration response spectra (5 percent damping) for seismograph located 1 m and 2.5 m into bedrock

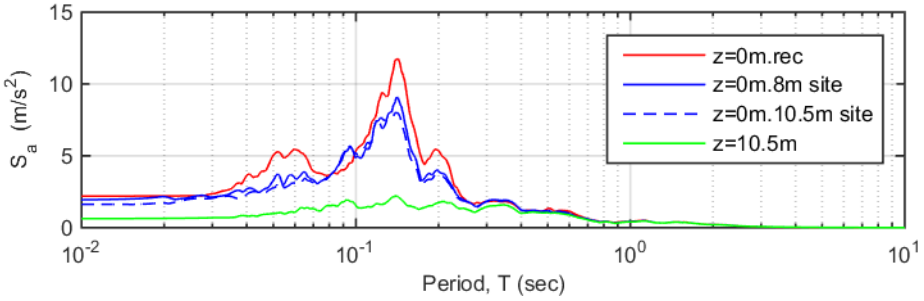

Figure 4-62: TS2 total stress acceleration response spectra (5 percent damping) for seismograph located 1 m and 2.5 m into bedrock

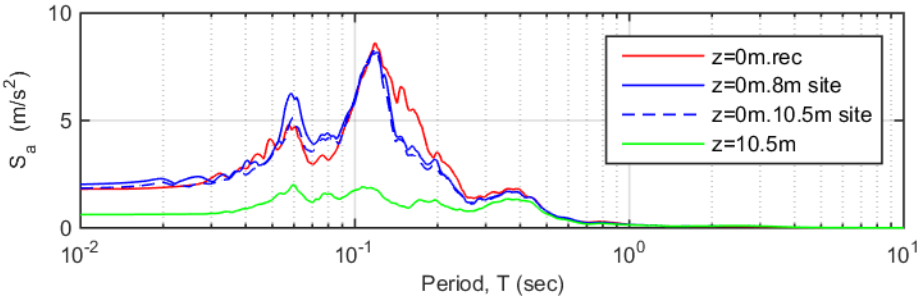

Figure 4-63: TS3 total stress acceleration response spectra (5 percent damping) for seismograph located 1 m and 2.5 m into bedrock

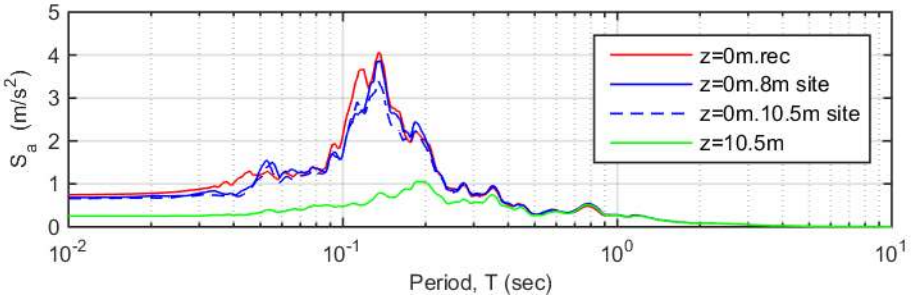

Figure 4-64: TS4 total stress acceleration response spectra (5 percent damping) for seismograph located 1 m and 2.5 m into bedrock

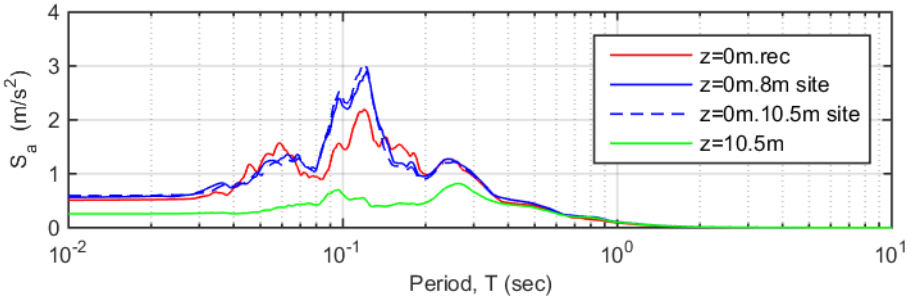

Figure 4-65: TS5 total stress acceleration response spectra (5 percent damping) for seismograph located 1 m and 2.5 m into bedrock

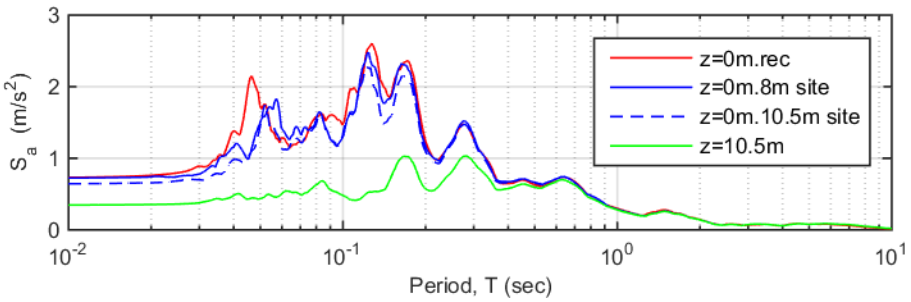

Figure 4-66: TS6 total stress acceleration response spectra (5 percent damping) for seismograph located 1 m and 2.5 m into bedrock

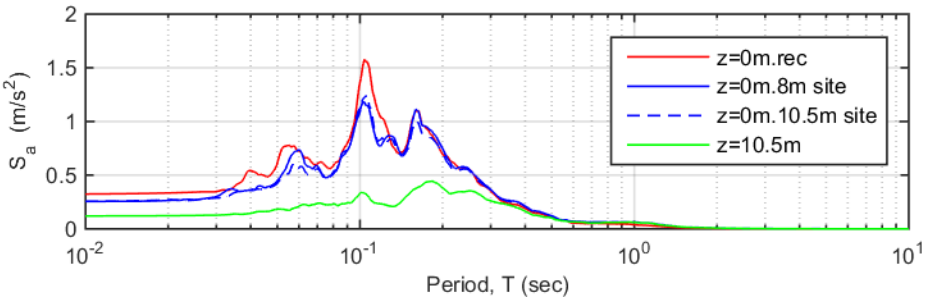

Figure 4-67: TS7 total stress acceleration response spectra (5 percent damping) for seismograph located 1 m and 2.5 m into bedrock

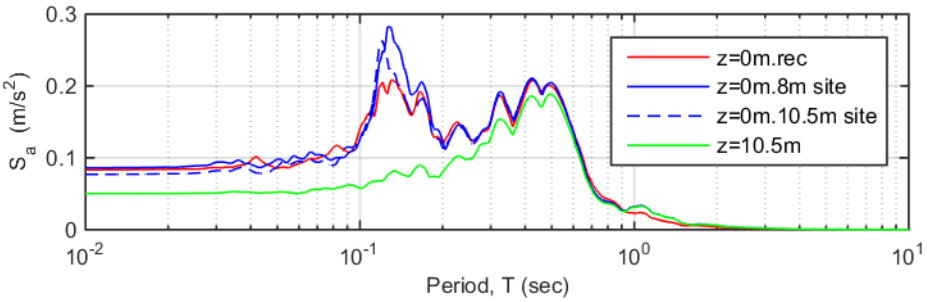

Figure 4-68: TS8 total stress acceleration response spectra (5 percent damping) for seismograph located 1 m and 2.5 m into bedrock

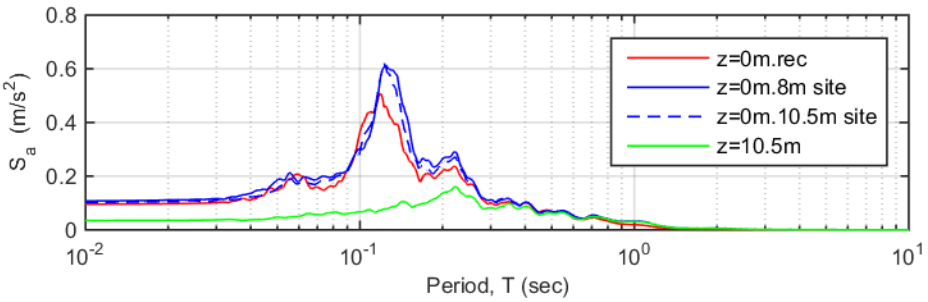

Figure 4-69: TS9 total stress acceleration response spectra (5 percent damping) for seismograph located 1 m and 2.5 m into bedrock

As can be observed in Figure 4-61 through Figure 4-69, the ground surface total stress acceleration response spectra simulated for the site configurations with the seismograph located 1 m and 3.5 m into the bedrock are approximately the same.

4.8.3 Comparison of Effective and Total Stress Analyses

In order to compare the difference in the predicted seismic ground response using effective and total stress analyses, the acceleration response spectra at the surface of the Sendai site for both the total and effective stress analyses are presented in Figure 4-70 through Figure 4-78.

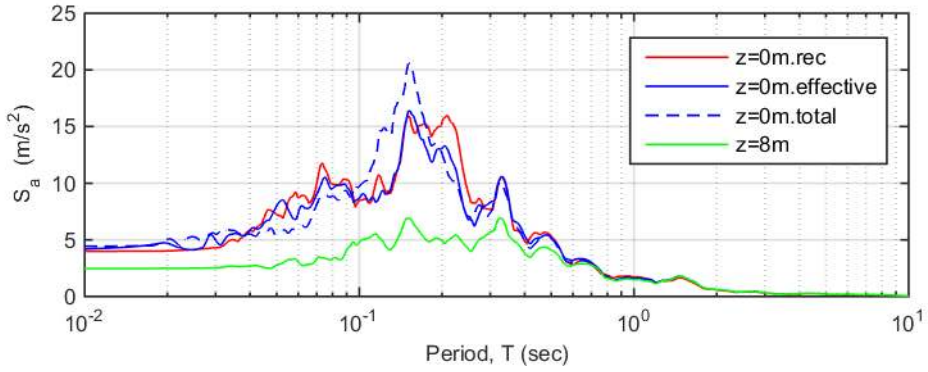

Figure 4-70: TS1 effective and total stress acceleration response spectra (5 percent damping)

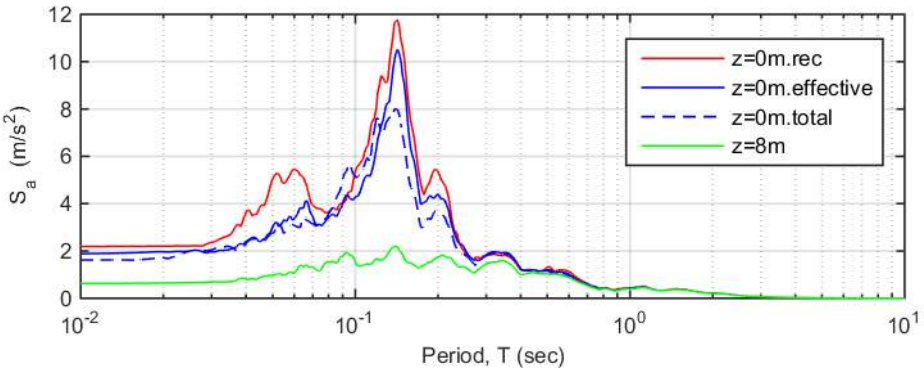

Figure 4-71: TS2 effective and total stress acceleration response spectra (5 percent damping)

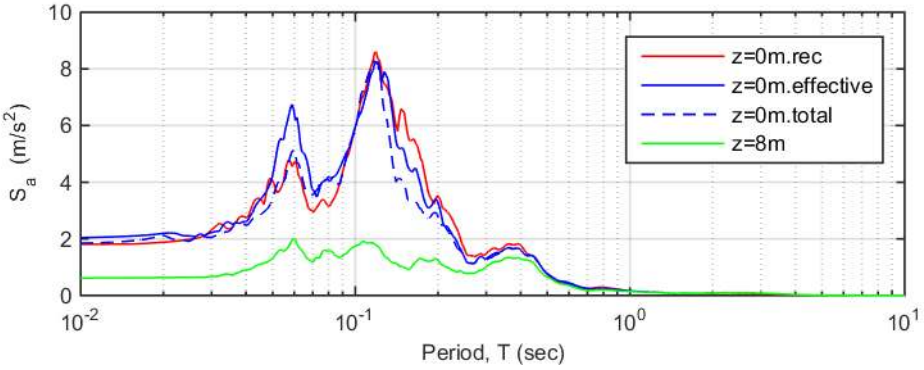

Figure 4-72: TS3 effective and total stress acceleration response spectra (5 percent damping)

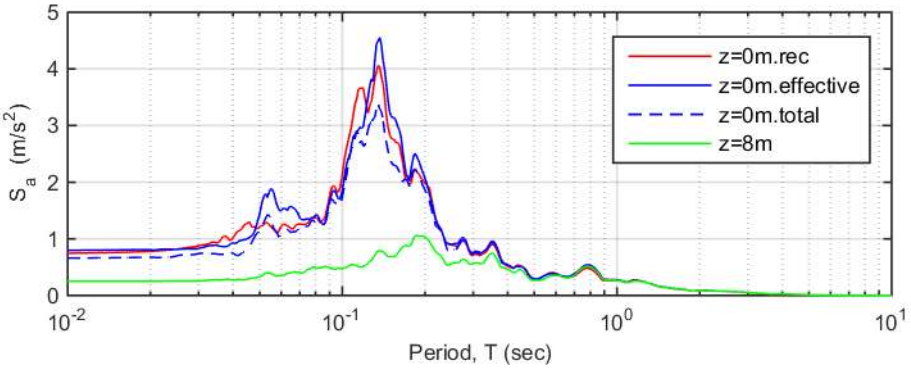

Figure 4-73: TS4 effective and total stress acceleration response spectra (5 percent damping)

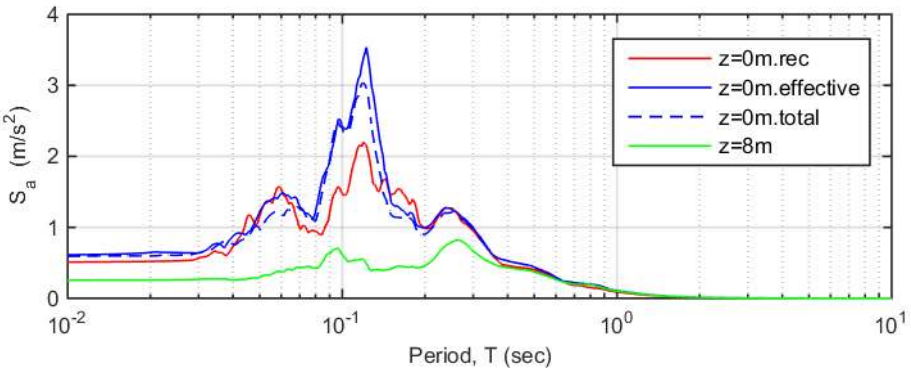

Figure 4-74: TS5 effective and total stress acceleration response spectra (5 percent damping)

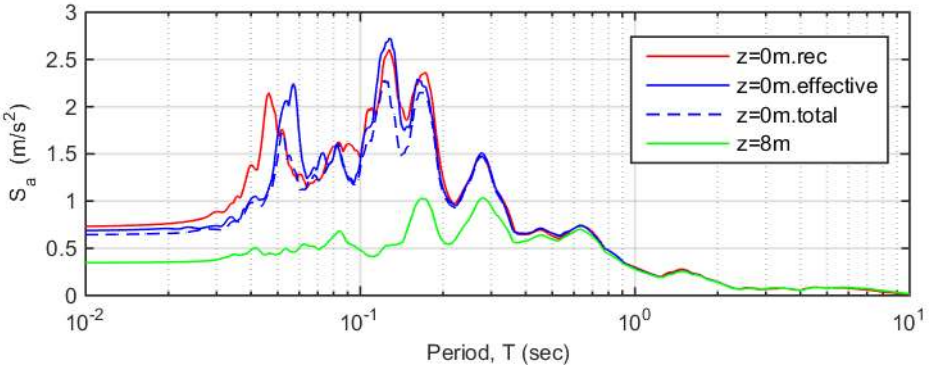

Figure 4-75: TS6 effective and total stress acceleration response spectra (5 percent damping)

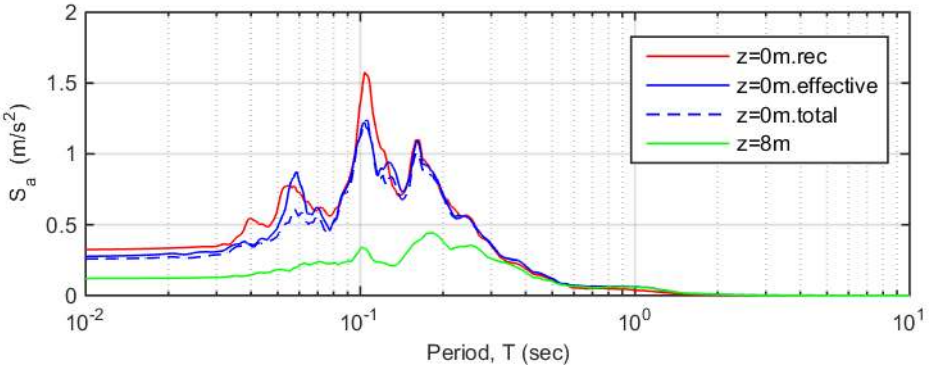

Figure 4-76: TS7 effective and total stress acceleration response spectra (5 percent damping)

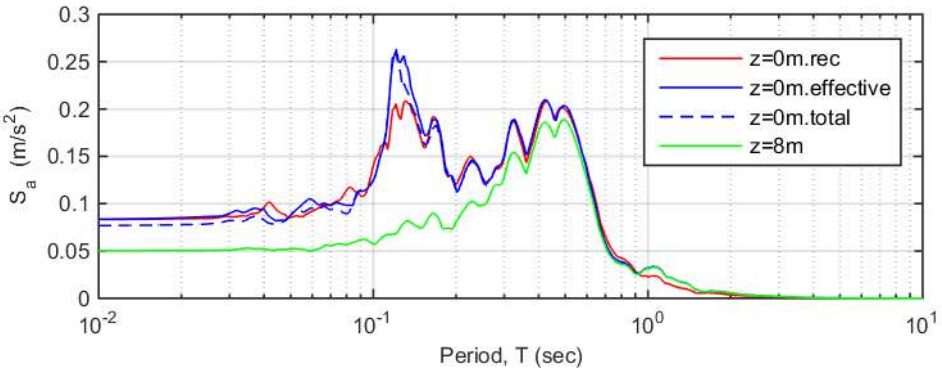

Figure 4-77: TS8 effective and total stress acceleration response spectra (5 percent damping)

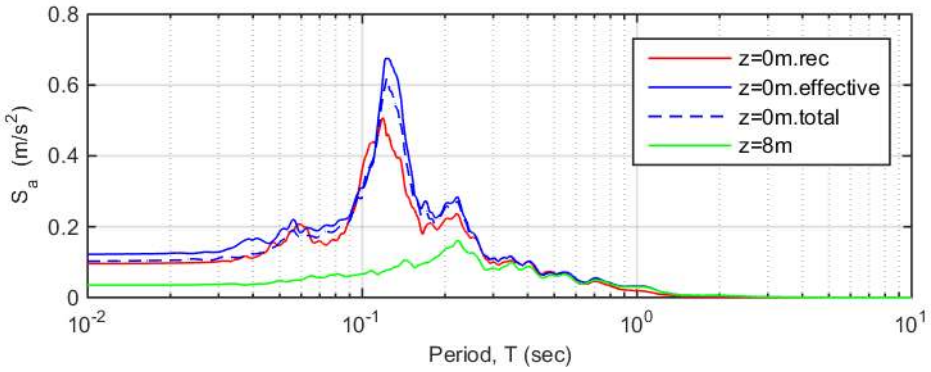

Figure 4-78: TS9 effective and total stress acceleration response spectra (5 percent damping)

Figure 4-70 through Figure 4-78 illustrate that the effective and total stress seismic ground response analyses of the Sendai site predict relatively similar surface acceleration response spectra for TS7 through TS9. Time series TS7 through TS9 cause soil column strains less than 0.002%. The effective stress analyses for the same time series generate excess porewater pressures during dynamic shaking less than 1.04 kPa. Based on this it can inferred that the time series TS7 through TS9 cause an insignificant build of excess porewater pressure and very small strains such that the effective and total stress analyses result in very similar predictions of ground surface acceleration response spectra.

Based on the acceleration response spectra in Figure 4-70 through Figure 4-75, the effective stress analyses generally better predict the recorded surface motion for TS1 through TS6, with the exception of TS5, where the total stress analysis slightly better predicts the recorded surface motion. The effective stress analysis predicts larger spectral accelerations than the total stress

analysis for each of these time series except TS1. Time series TS2 through TS6 all cause soil strains less than approximately 0.01% and 0.02% for the total and effective stress analyses, respectively. The time series TS1 is the largest input motion and causes soil strains up to approximately 0.3% during the effective stress analysis (as illustrated in Figure 4-34) and approximately 0.1% during the total stress analysis (as illustrated in Figure 4-52). This may imply that as larger strain develops, among other thing the porewater – soil skeleton interaction which develops in an effective stress analysis may invoke some level of damping which is not accounted for in a total stress analysis. These results show the importance of modelling the pore fluid phase of the soil in an effective stress analysis, even when the soils are not subject to large strain movements such as those which result from liquefaction.

4.8.4 Effect of Soil Permeability

In order to explore the effect of soil permeability on the ground response modeled with the effective stress analyses, additional simulations were run on the two input motions which invoked the largest increase in porewater pressure during seismic shaking; being input motions TS1 and TS2. For the additional analyses, soil permeability was selected to be $k = 10^{-4}$ m/s and $k = 10^{-6}$ m/s in order to cover a range of reasonable permeability values for sandy soils. The spectral acceleration responses for these simulations are presented in Figure 4-79 and Figure 4-80 to compare the results of these analyses.

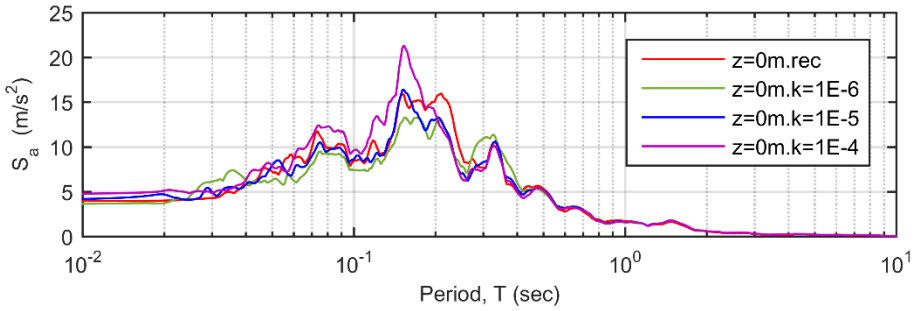

Figure 4-79: TS1 acceleration response spectra for varying soil permeability

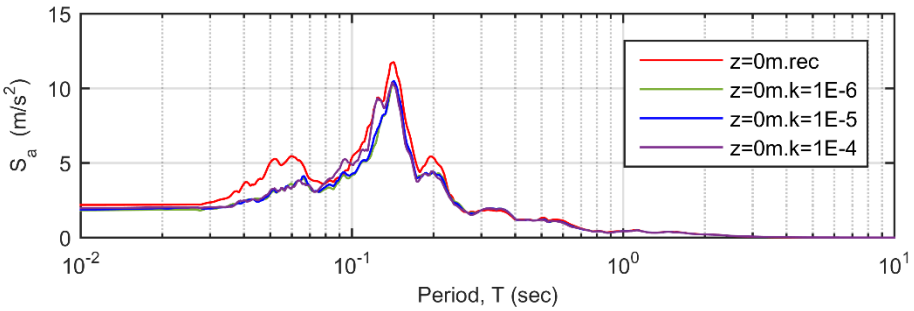

Figure 4-80: TS2 acceleration response spectra for varying soil permeability

It can be observed from Figure 4-79 and Figure 4-80 that the ground response varies more significantly with different soil permeability values for input motion TS1 than for input motion TS2. The ground response at the surface of the soil column to input motion TS1 overestimates the recorded peak response when the soil permeability is k = 10^{-4} m/s, whereas the peak ground response is underestimated when the soil permeability is k = 10^{-6} m/s. The ground response at the surface of the soil column to input motion TS2 is similar for each of the soil permeability values simulated, indicating that the soil permeability does not contribute as significantly to the simulated ground response as it does for TS1. Nonetheless, the findings presented in Figure 4-79 and Figure 4-80 highlight the importance of characterizing the soil hydraulic properties when carrying out ground response analyses for sites which are expected to be subject to relatively strong seismic events, regardless of whether or not the soil is expected to undergo large strain deformation.

Chapter 5: Application of SANISAND to Model Dilation Pulses

5.1 Introduction

This chapter presents numerical simulations of seismic ground response analyses on a generic site for the purpose of investigating the ability of the SANISAND model to simulate complex soil behaviour during a seismic event, such as high frequency dilation pulses when seismic waves propagate through a shallow medium-dense sand site. Nine recorded and four scaled ground motions are propagated through the site to complete these analyses. Further discussion on the seismic ground response analyses completed and the results are presented in the following sections.

5.2 Continuum Model

Total and effective stress seismic ground response analyses were completed to simulate the one-dimensional propagation of seismic waves through a generic site comprised of a 10 m deep layer of sand over an elastic half-space.

A parabolic distribution of shear wave velocity between 120 m/s at the surface of the site and 300 m/s at the base of the site was applied to represent in situ site stiffness. The groundwater table was assumed to be located at a depth of 2 m. Figure 5-1 illustrates the generic site profile and distribution of shear wave velocity.

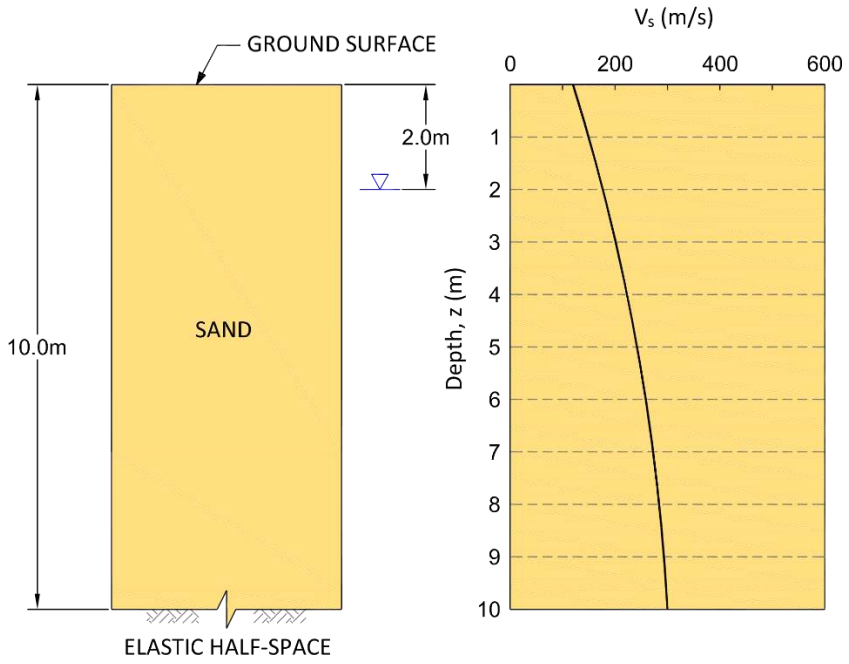

Figure 5-1: Generic site profile and distribution of shear wave velocity

The effective and total stress analyses were completed using the analysis procedures as previously described for the Sendai site, including the same element types, boundary conditions, constitutive materials, loading patterns and equation solvers. The minimum vertical element size for the generic site was selected to be 0.25 m in order to allocate eight elements to a wavelength propagating with a maximum frequency of f_{max} = 50 Hz. through soil with a minimum shear wave velocity $V_{s\text{-}min}$ = 120 m/s. A Lysmer-Kuhlemeyer dashpot was modeled at the base of the soil column in order to reproduce the within-ground input motions used in the analyses, which are further discussed in Section 5.3.

The sand layer is represented by the SANISAND constitutive model implemented in OpenSees. The SANISAND model parameters for Toyoura sand were selected for the nonlinear seismic ground response analyses of the generic site. The Toyoura sand parameters are based on the work of Taiebat et al. (2010) who compared experimental results and numerical simulations for Toyoura sand, Nevada sand and Sacramento sand using the SANISAND model. The SANISAND model parameters for Toyoura sand are presented in Table 5-1.

Table 5-1: SANISAND model parameters for Toyoura Sand (adapted from Taiebat et al., 2010)

Parameter	Symbol	Value
Elasticity	G_0	Variable[1]
	ν	0.05
CSL	M	1.25
	c	0.712
	e_0	0.934
	λ	0.019
	ξ	0.7
Yield Surface	m	0.02
Dilatancy	n^d	2.1
	A_0	0.704
Plastic Modulus	n^b	1.25
	h_0	7.05
	c_h	0.968
Fabric Dilatancy	z_{max}	2.0
	c_z	600

1. See Table 5-2 for G_0 values

The modeled sand had a mass density $\rho = 1700$ kg/m^3. To simulate medium-dense sand with a relative density of 65%, the initial void ratio was selected to be $e_{in} = 0.73$, based on the maximum void ratio $e_{max} = 0.977$ and minimum void ratios $e_{min} = 0.597$ for Toyoura Sand provided in Ishihara (1996).

As was shown for the Sendai site, the small strain shear modulus determined in the laboratory and by in situ measurements can differ greatly, and this difference effects the calibration of the model constant G_0. Therefore, the SANISAND model for the generic site is calibrated at 1 m intervals over the depth of the model based on the in situ shear wave velocity, confining pressure and void ratio using Equation (2.19)(2.19. The G_0 model constant values are summarized in Table 5-2.

Table 5-2: SANISAND G_0 model constants for generic site

Depth (m)	G_0 Value
0 – 1	365
1 – 2	370
2 – 3	435
3 – 4	490
4 – 5	535
5 – 6	580
6 – 7	620
7 – 8	660
8 – 9	700
9 – 10	740

The effective stress analyses require the additional parameter of soil permeability which was selected to be $k = 10^{-5}$ m/s.

5.3 Earthquake Input Motions

Earthquake input motions were applied at the base of the generic site using the same methodology described for the Sendai site. The nine earthquake motions summarized in Table 4-6 (TS1 through TS9) and used for the seismic ground response simulations of the Sendai site were used as input motions in the analyses of the 10 m deep generic site.

In order to simulate a wider range of earthquake input motions with different PGAs, the time series TS1 was scaled by constant factors 0.5 (TS1-0.50), 0.75 (TS1-0.75), 1.25 (TS1-1.25), and 1.5 (TS1-1.50) using the software SeismoSignal (Seismosoft, 2013). The resulting artificial time series, their PGAs and duration are summarized in Table 5-3.

Table 5-3: Summary of artificial earthquake input motions

Time Series	Scaling Factor	PGA (g)	Duration (sec)
TS1-050	0.50	0.125	312
TS1-075	0.75	0.189	312
TS1-125	1.25	0.314	312
TS1-150	1.50	0.376	312

5.4 Analysis Results

In this section the results of the total and effective stress seismic ground response analyses carried out for the generic 10 m deep sand site are presented. In particular variations of acceleration, porewater pressure (for the effective stress analyses), and stress and strain were recorded along the soil profile during the analyses. The section includes acceleration and pore pressure time histories at select depths of the soil profile, stress-strain loops and acceleration response spectra.

5.4.1 Seismic Ground Response Using Effective Stress Analyses

The simulation results for the effective stress seismic ground response analyses are presented in Figure 5-2 through Figure 5-14. The effective stress analysis results presented include the following:

- East-west horizontal acceleration time history simulated at the surface of the site and input at the base of the site profile;
- The pore pressure time history simulated at 2 m depth intervals over the soil profile;
- The east-west horizontal acceleration response spectra with a damping ratio of $\xi = 5\%$ simulated at the surface of the site and input at the base of the site profile; and
- The stress-strain loops simulated at 3 m intervals over the soil profile.

In the figures below, z refers to the site depth, as indicated on Figure 5-1.

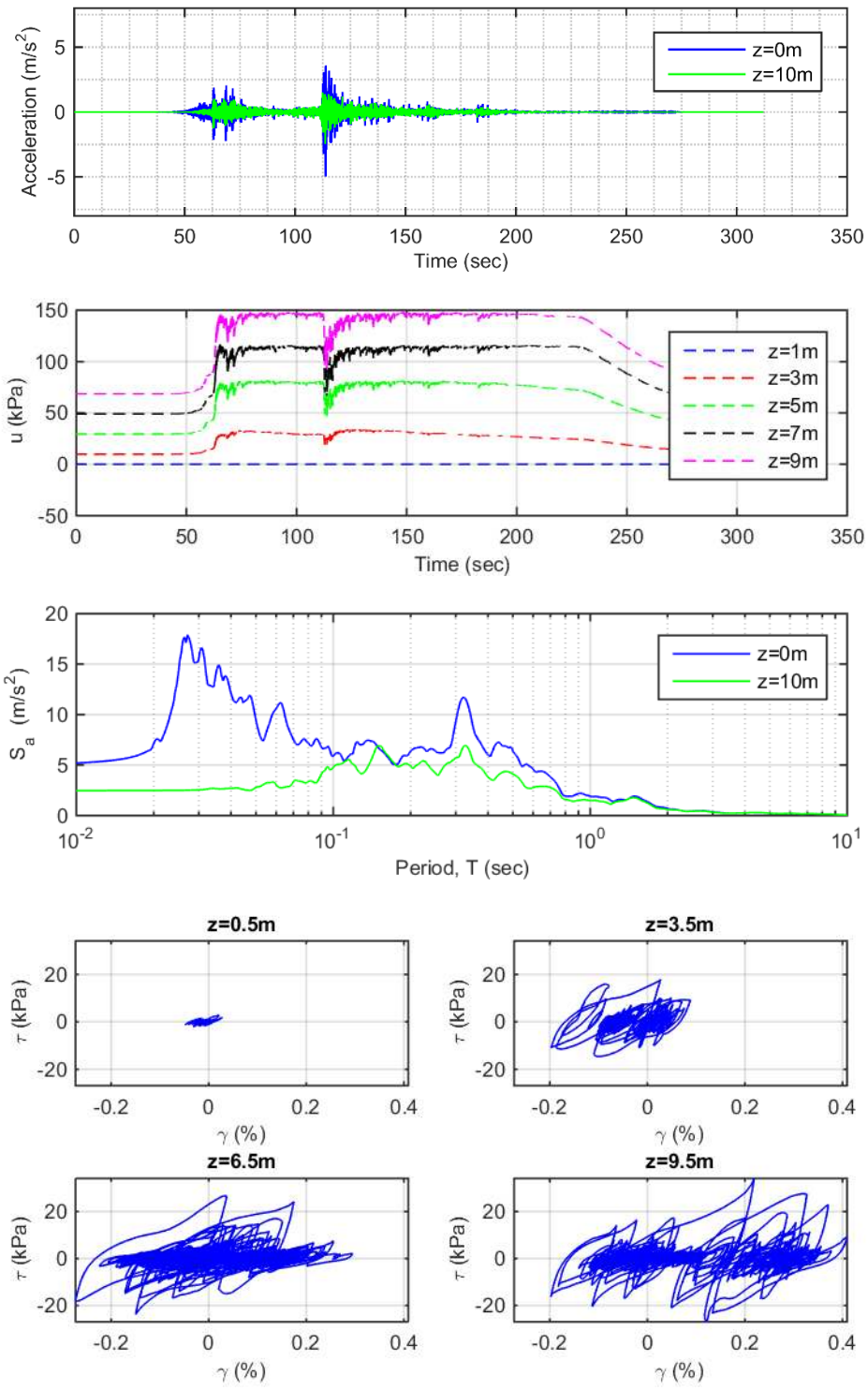

Figure 5-2: TS1 effective stress acceleration and pore pressure time history, acceleration response spectra (5 percent damping), and stress-strain loops

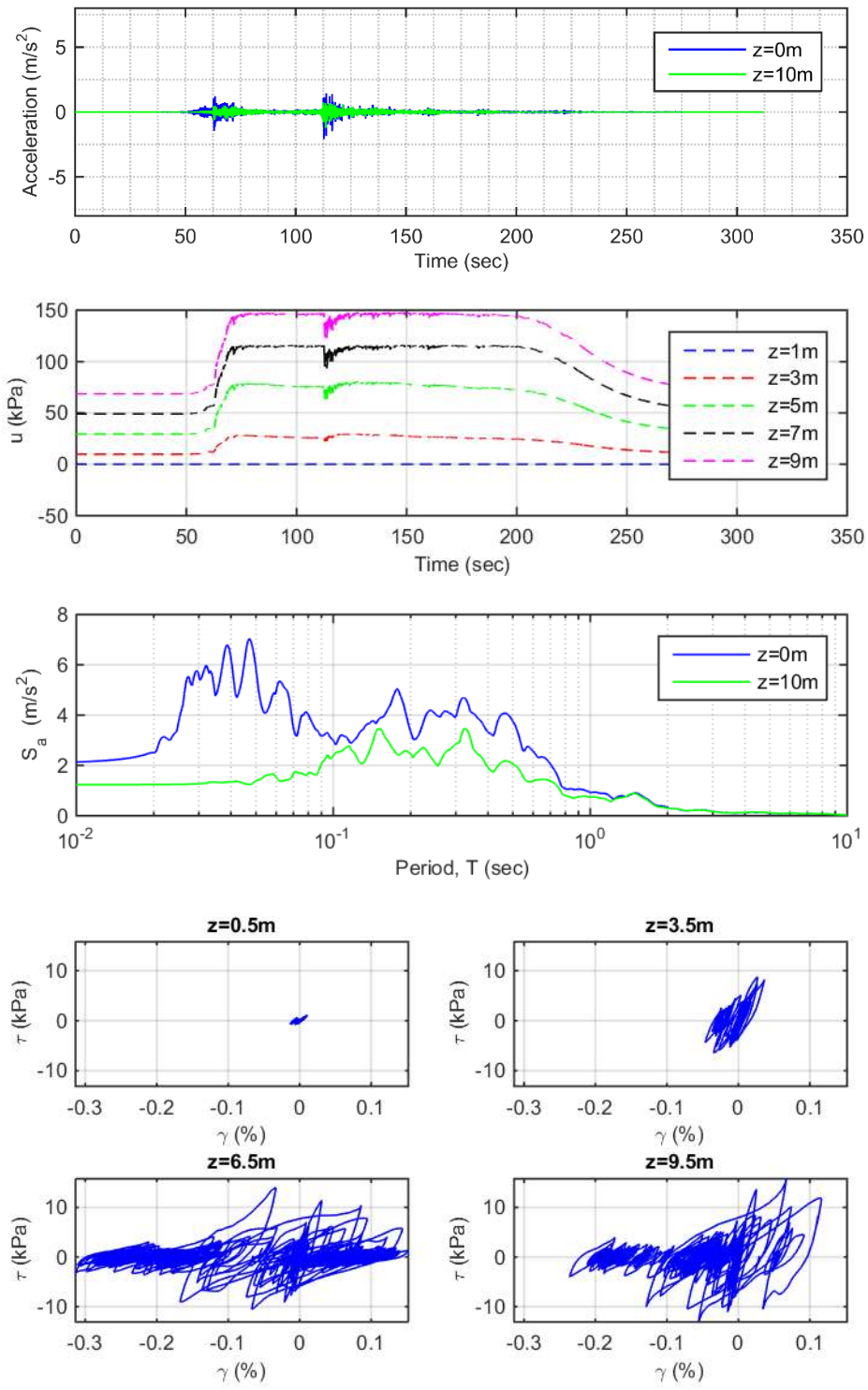

Figure 5-3: TS1-050 effective stress acceleration and pore pressure time history, acceleration response spectra (5 percent damping), and stress-strain loops

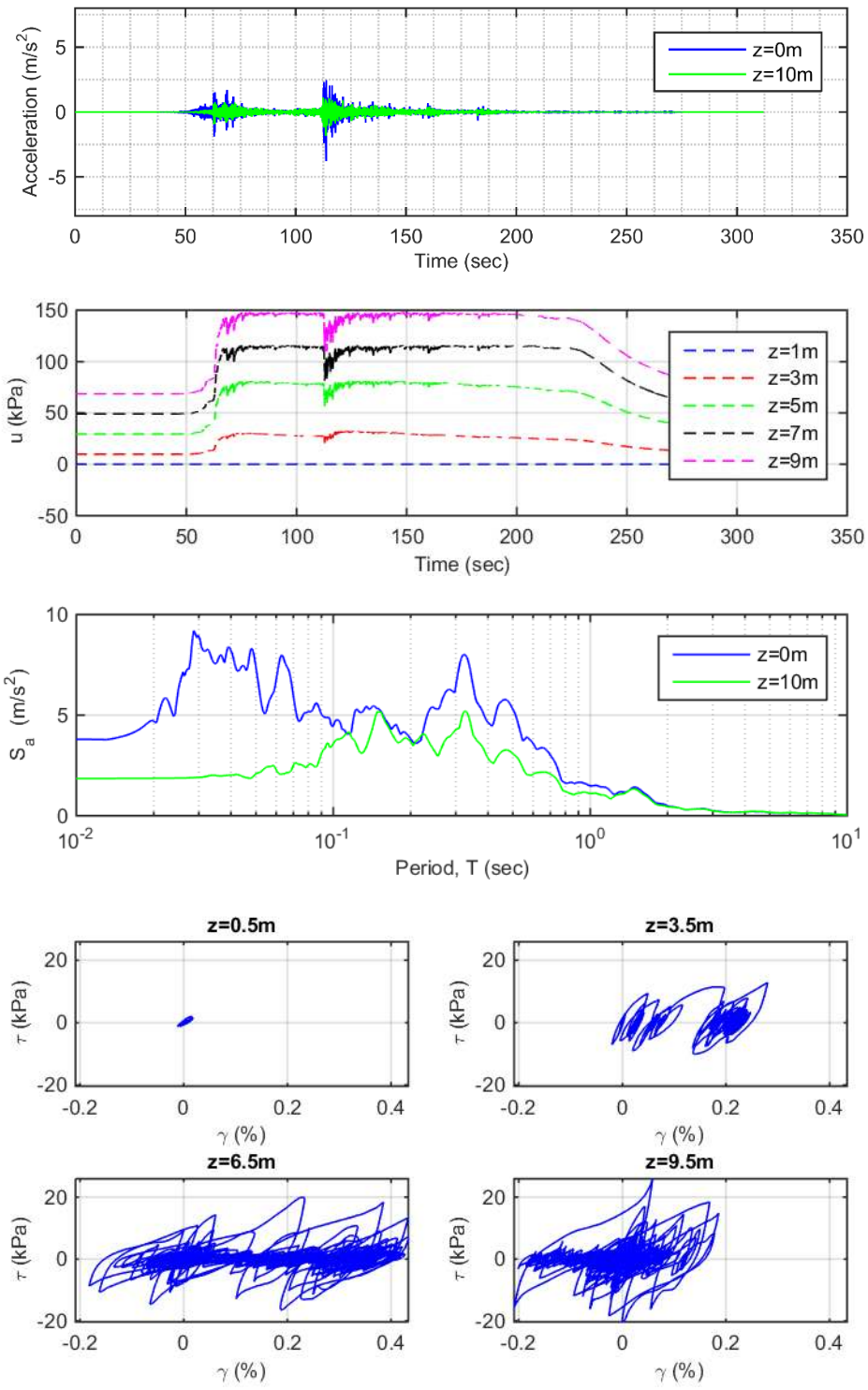

Figure 5-4: TS1-075 effective stress acceleration and pore pressure time history, acceleration response spectra (5 percent damping), and stress-strain loops

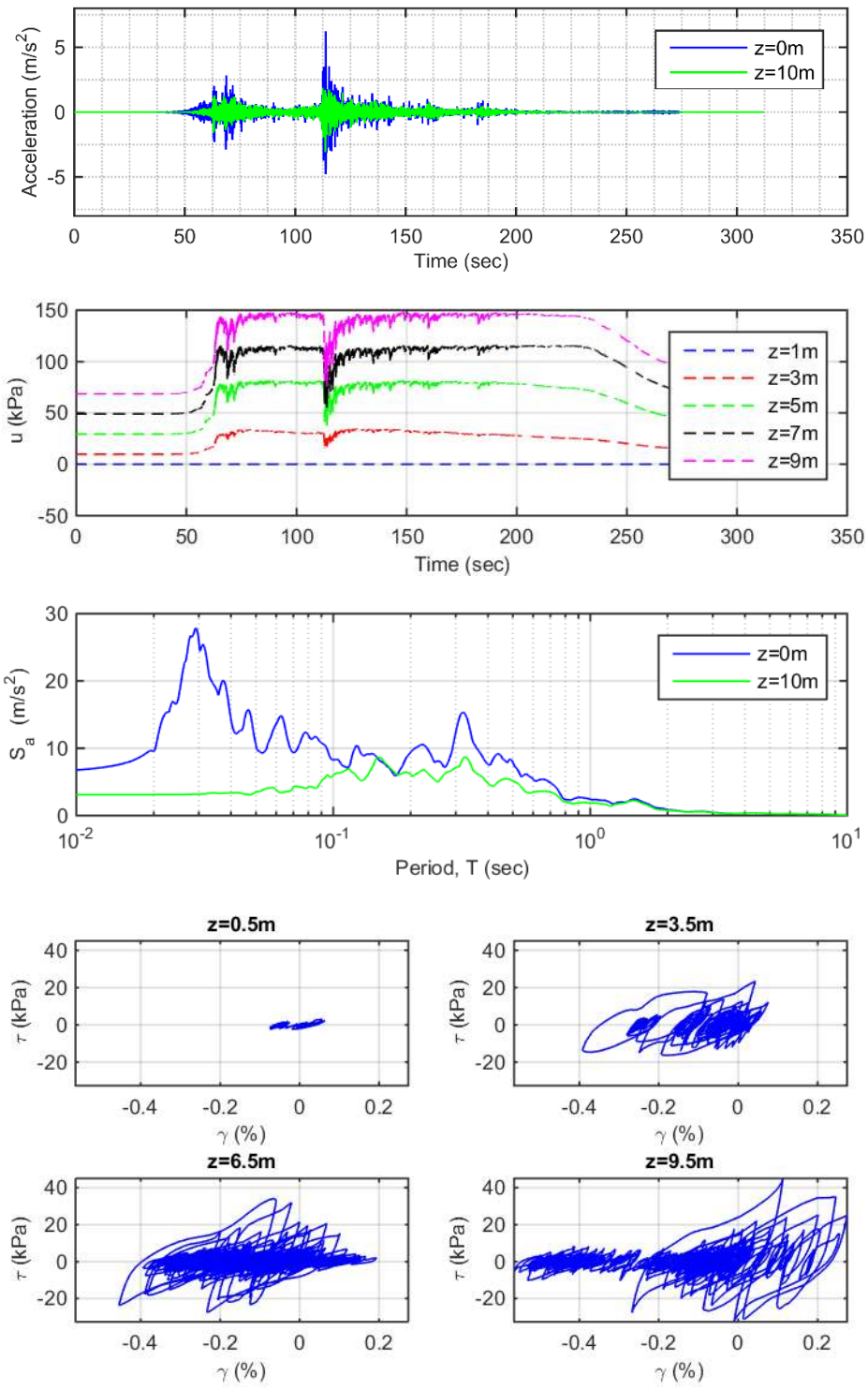

Figure 5-5: TS1-125 effective stress acceleration and pore pressure time history, acceleration response spectra (5 percent damping), and stress-strain loops

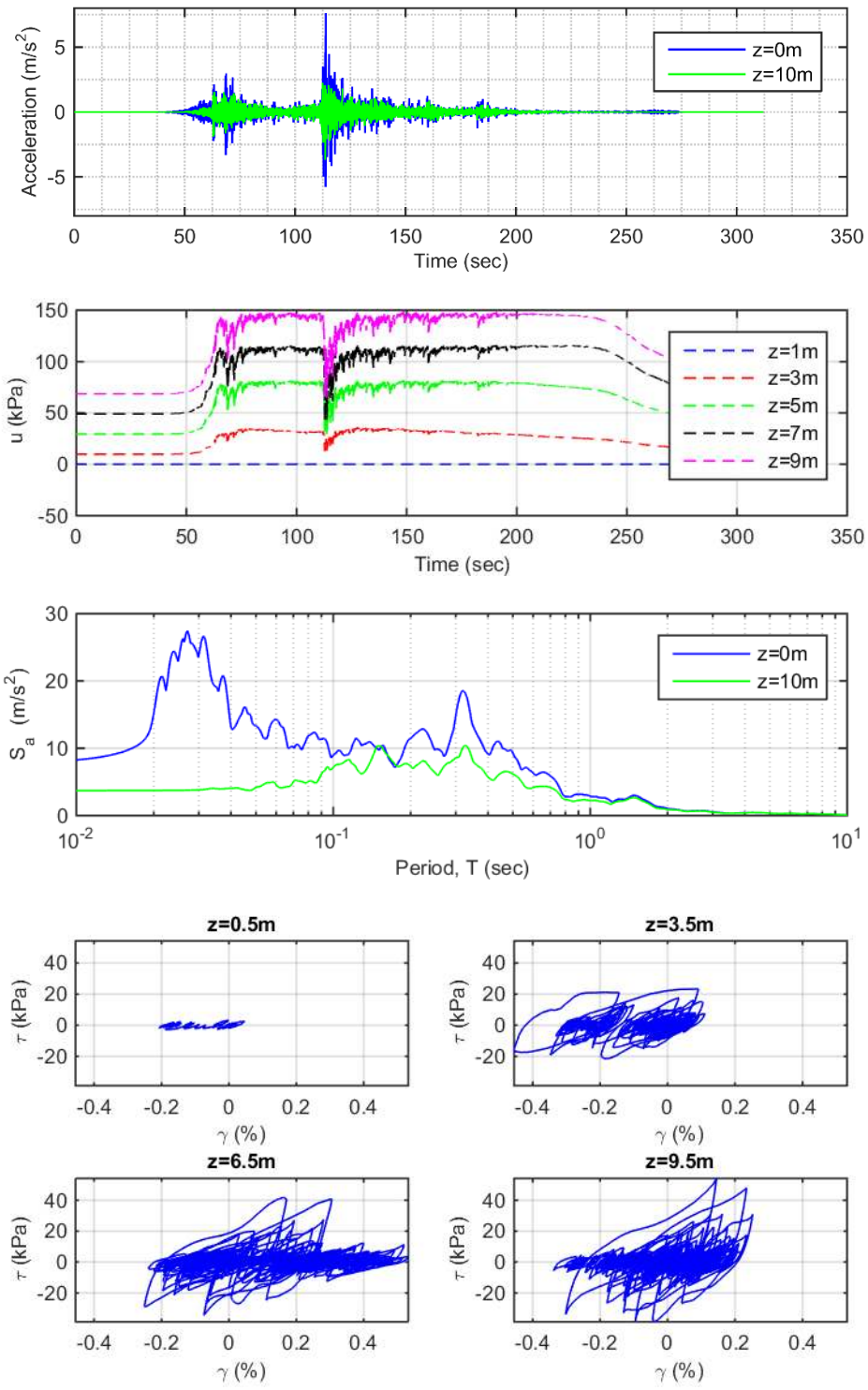

Figure 5-6: TS1-150 effective stress acceleration and pore pressure time history, acceleration response spectra (5 percent damping), and stress-strain loops

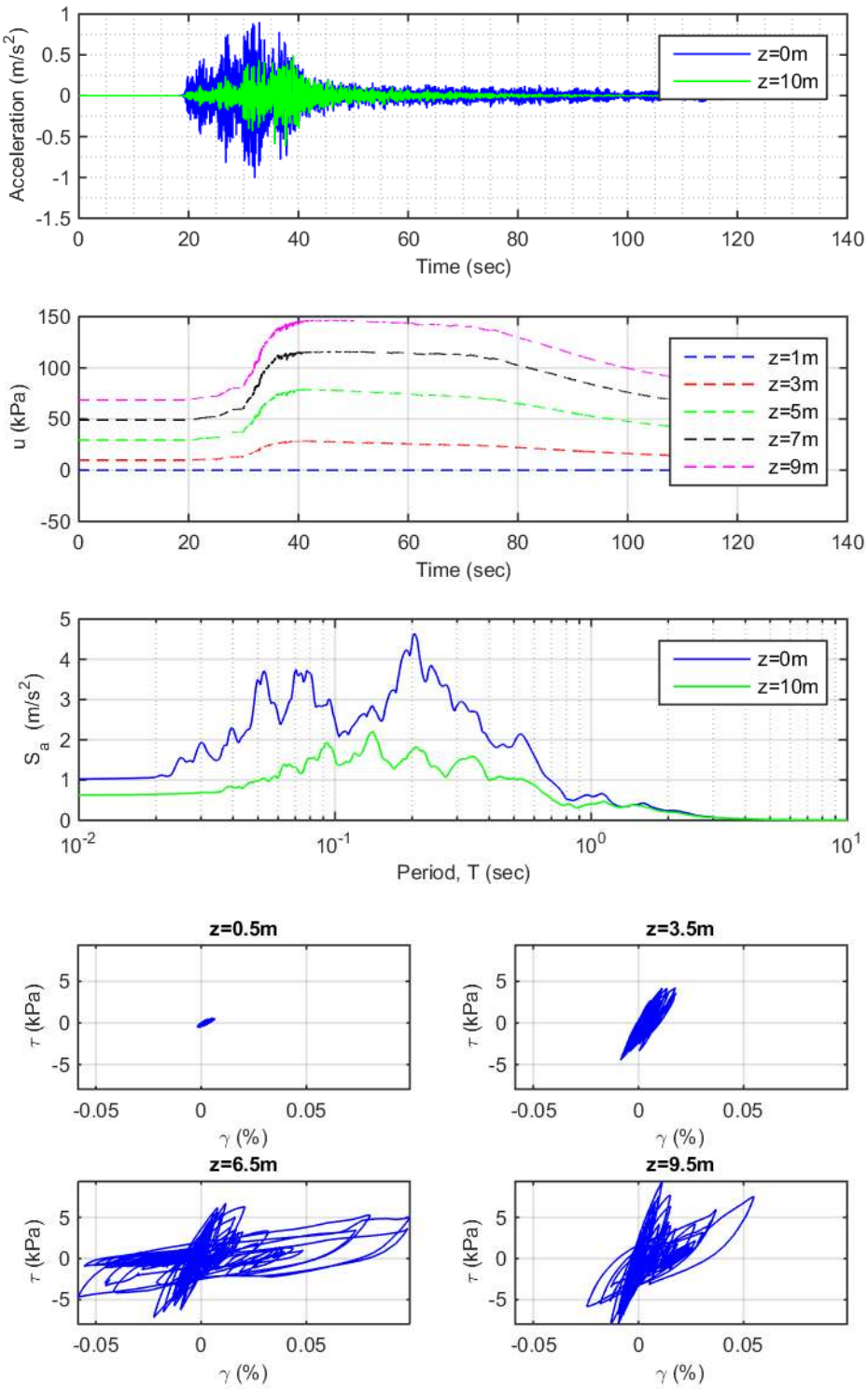

Figure 5-7: TS2 effective stress acceleration and pore pressure time history, acceleration response spectra (5 percent damping), and stress-strain loops

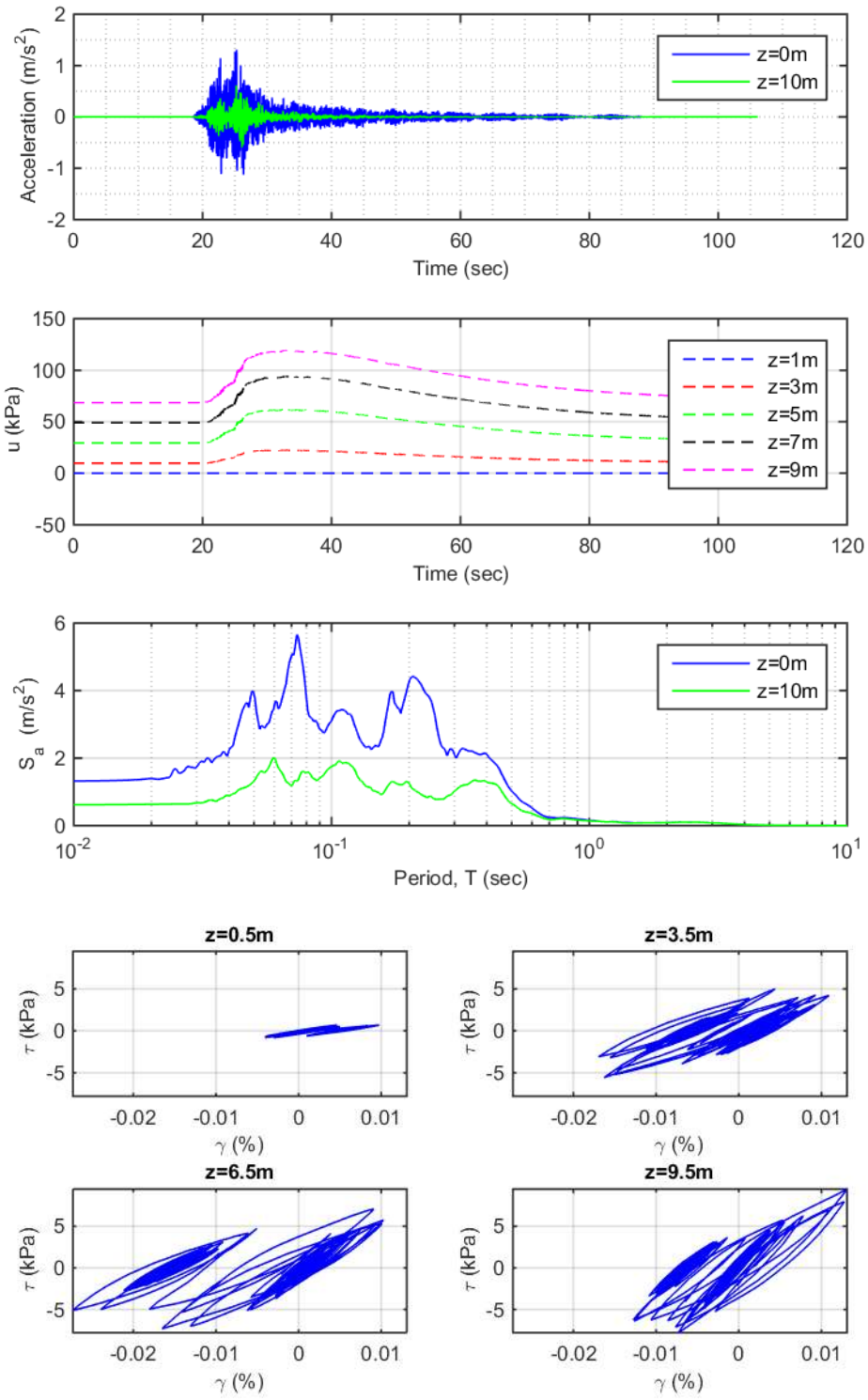

Figure 5-8: TS3 effective stress acceleration and pore pressure time history, acceleration response spectra (5 percent damping), and stress-strain loops

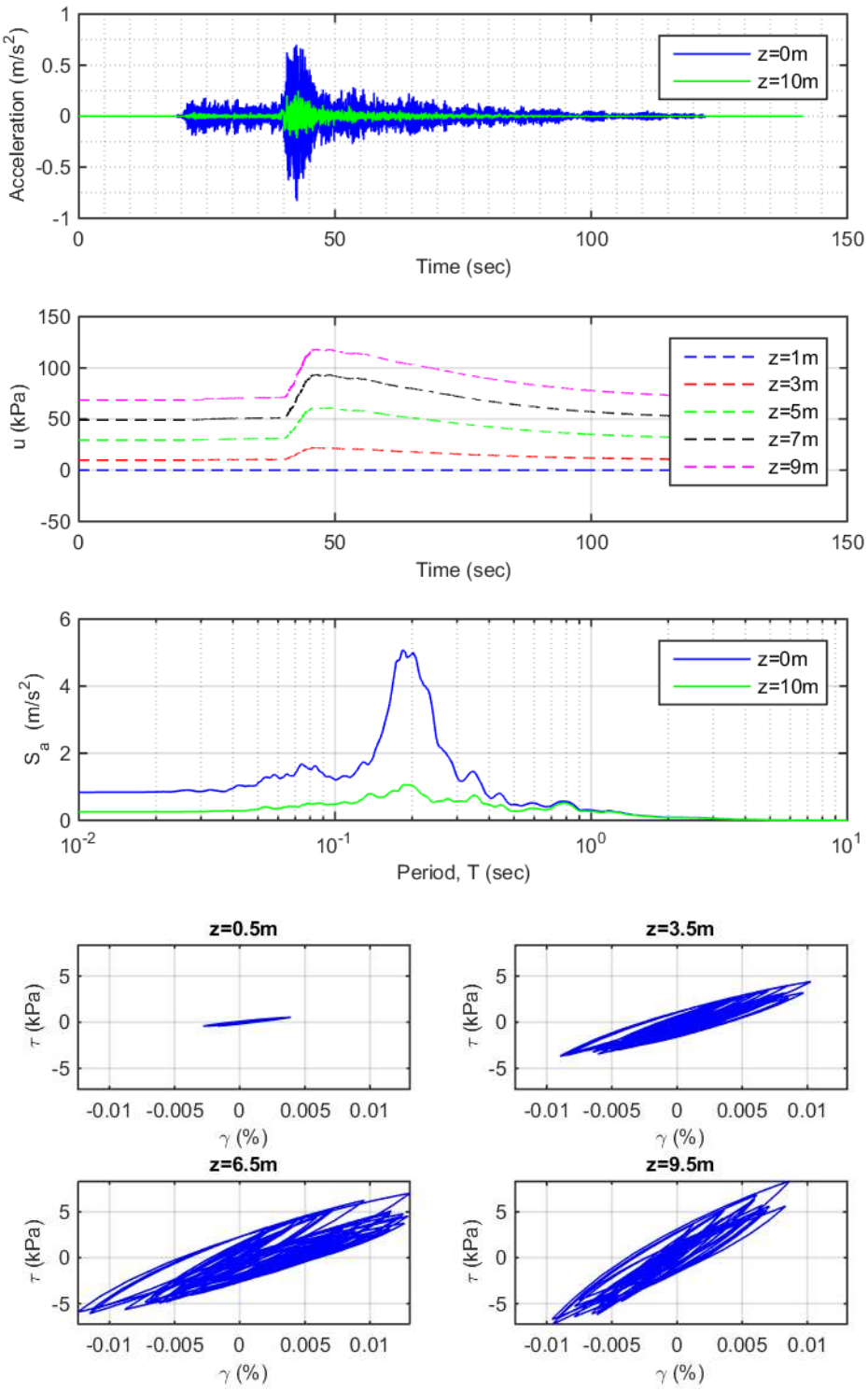

Figure 5-9: TS4 effective stress acceleration and pore pressure time history, acceleration response spectra (5 percent damping), and stress-strain loops

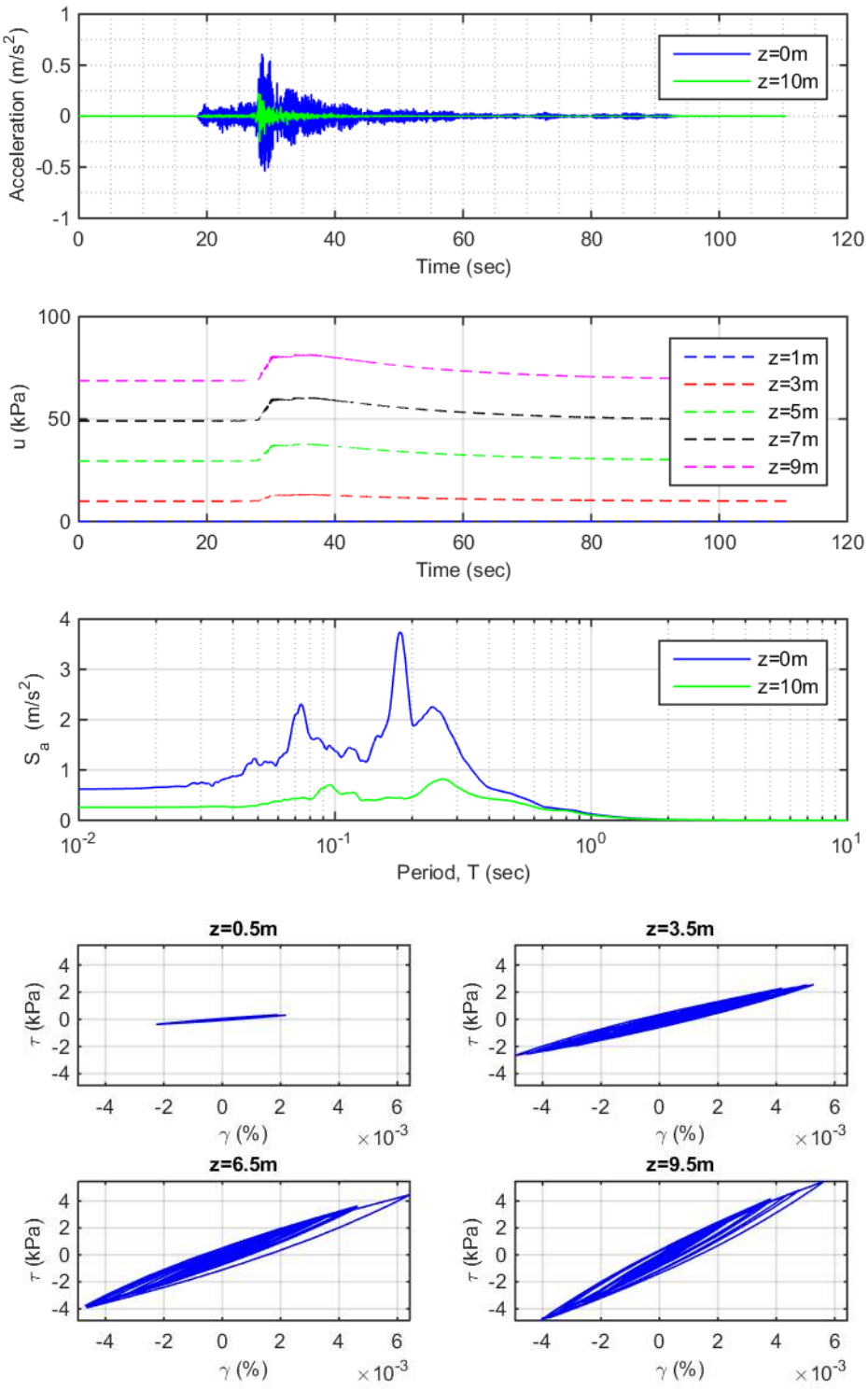

Figure 5-10: TS5 effective stress acceleration and pore pressure time history, acceleration response spectra (5 percent damping), and stress-strain loops

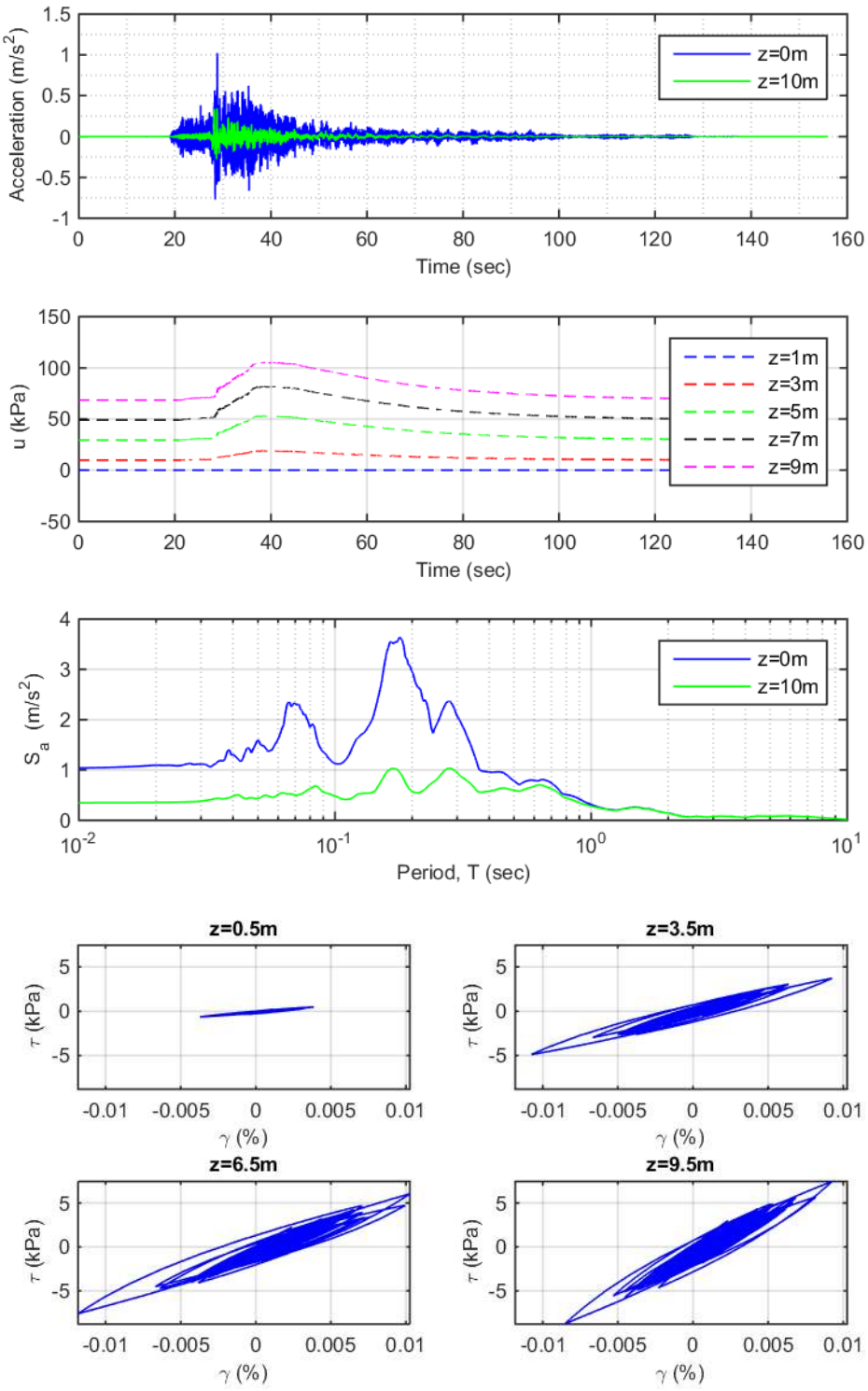

Figure 5-11: TS6 effective stress acceleration and pore pressure time history, acceleration response spectra (5 percent damping), and stress-strain loops

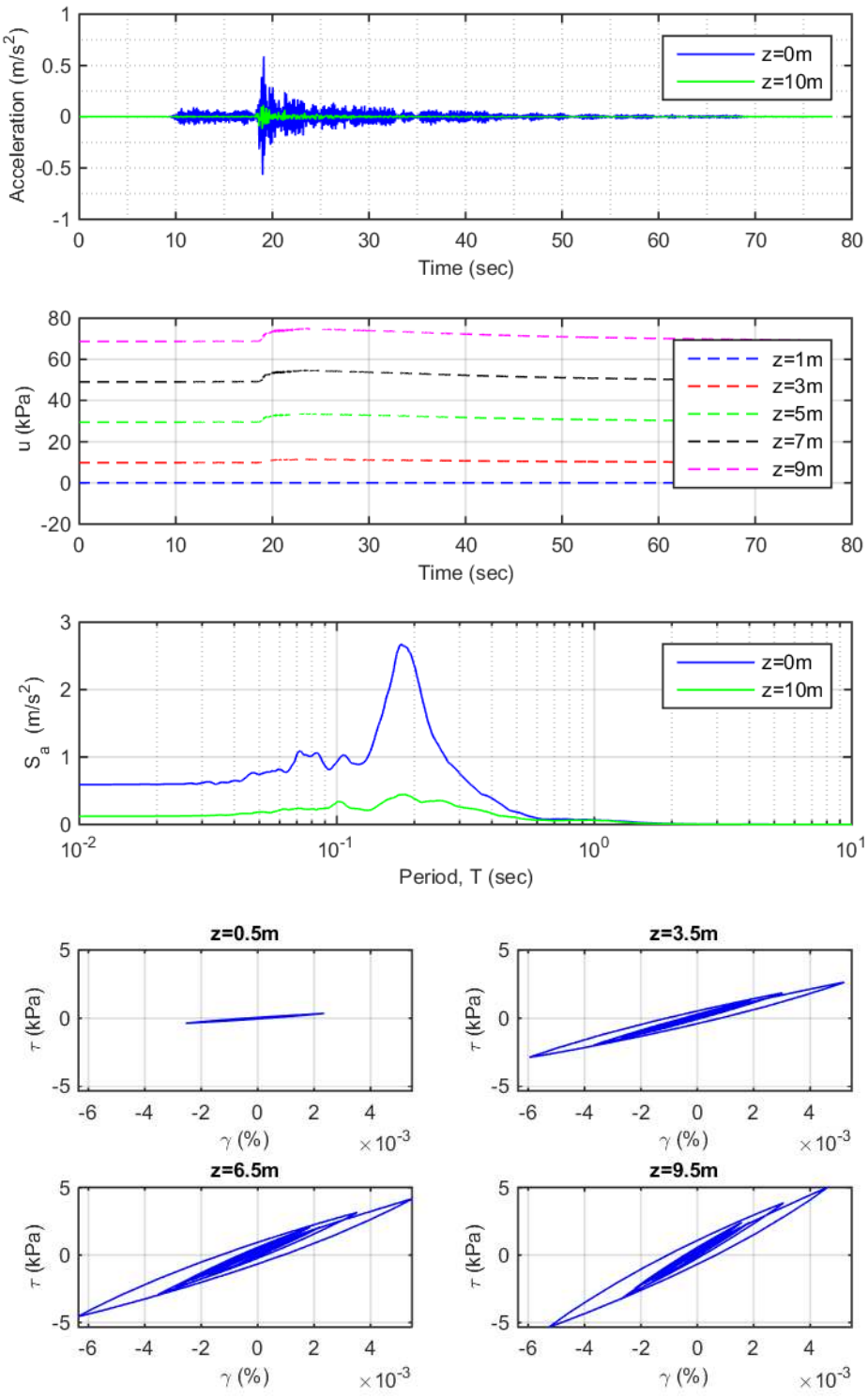

Figure 5-12: TS7 effective stress acceleration and pore pressure time history, acceleration response spectra (5 percent damping), and stress-strain loops

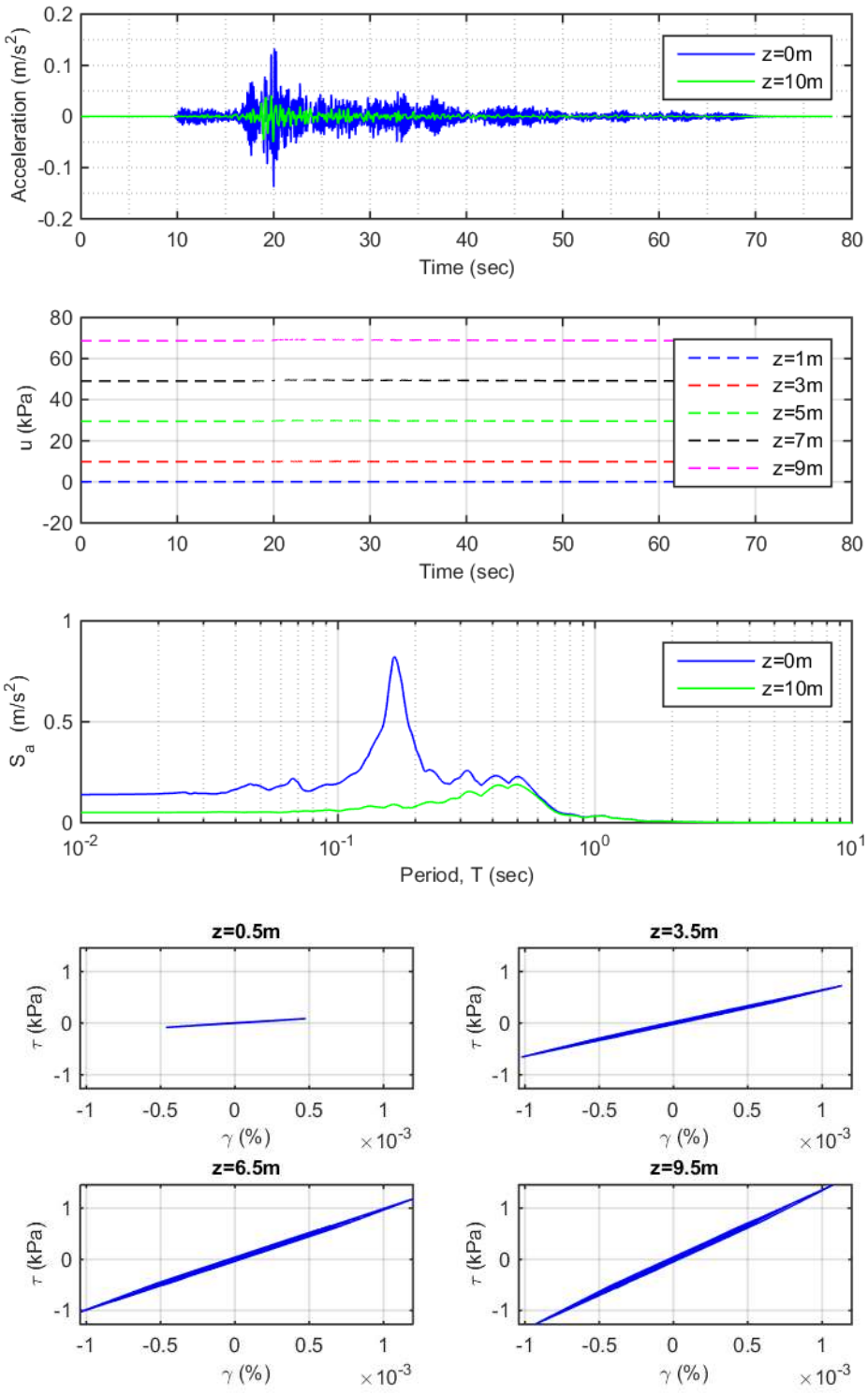

Figure 5-13: TS8 effective stress acceleration and pore pressure time history, acceleration response spectra (5 percent damping), and stress-strain loops

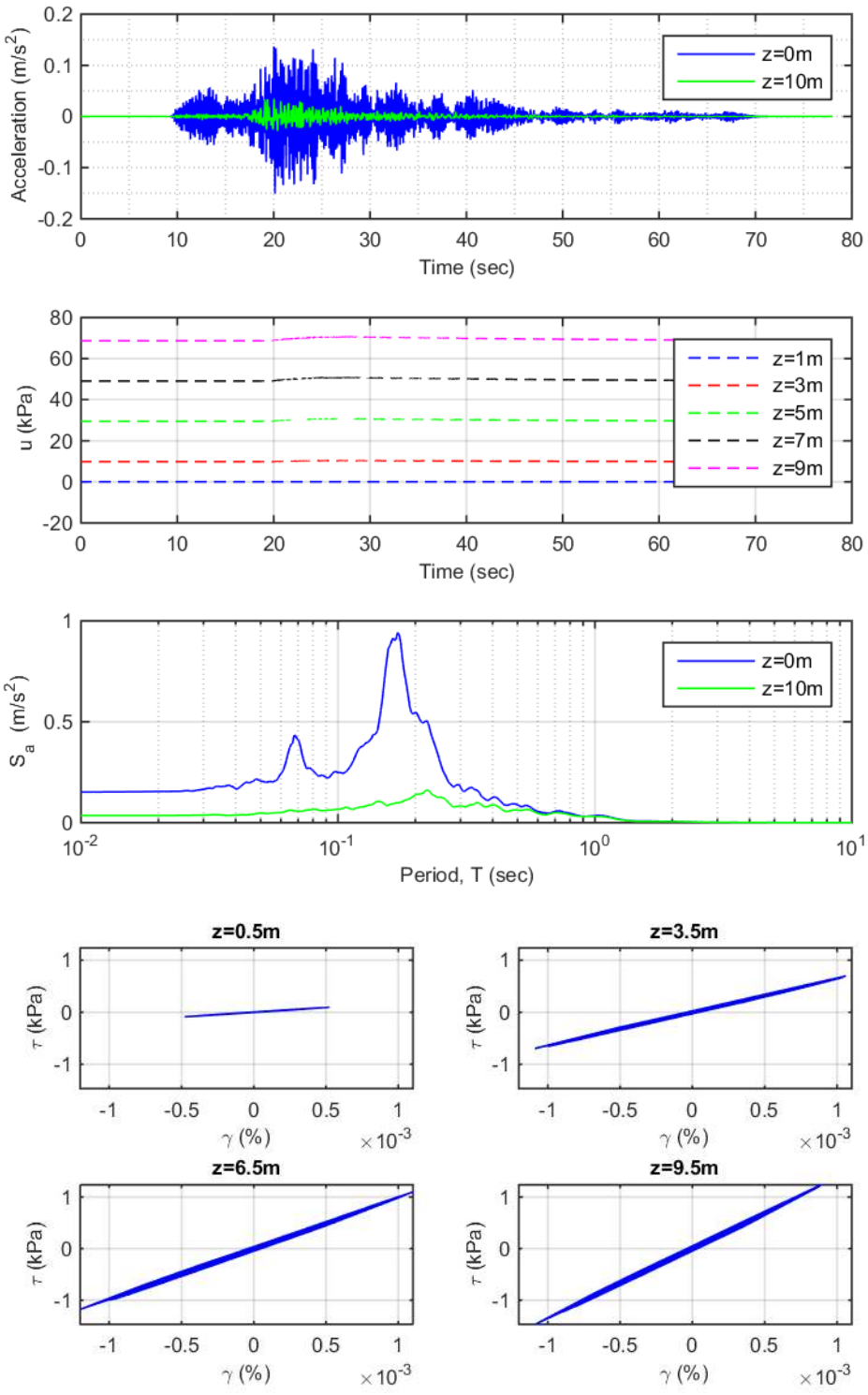

Figure 5-14: TS9 effective stress acceleration and pore pressure time history, acceleration response spectra (5 percent damping), and stress-strain loops

5.4.2 Seismic Ground Response Using Total Stress Analyses

The simulation results for the total stress seismic ground response analyses are presented in Figure 5-15 through Figure 5-27. The total stress analysis results presented include the following:

- East-west horizontal acceleration time history simulated at the surface of the site and input at the base of the site profile;
- The east-west horizontal acceleration response spectra with a damping ratio of $\xi = 5\%$ simulated at the surface of the site and input at the base of the site profile; and
- The stress-strain loops simulated at 3 m intervals over the soil profile.

In the figures below, z refers to the site depth, as indicated on Figure 5-1.

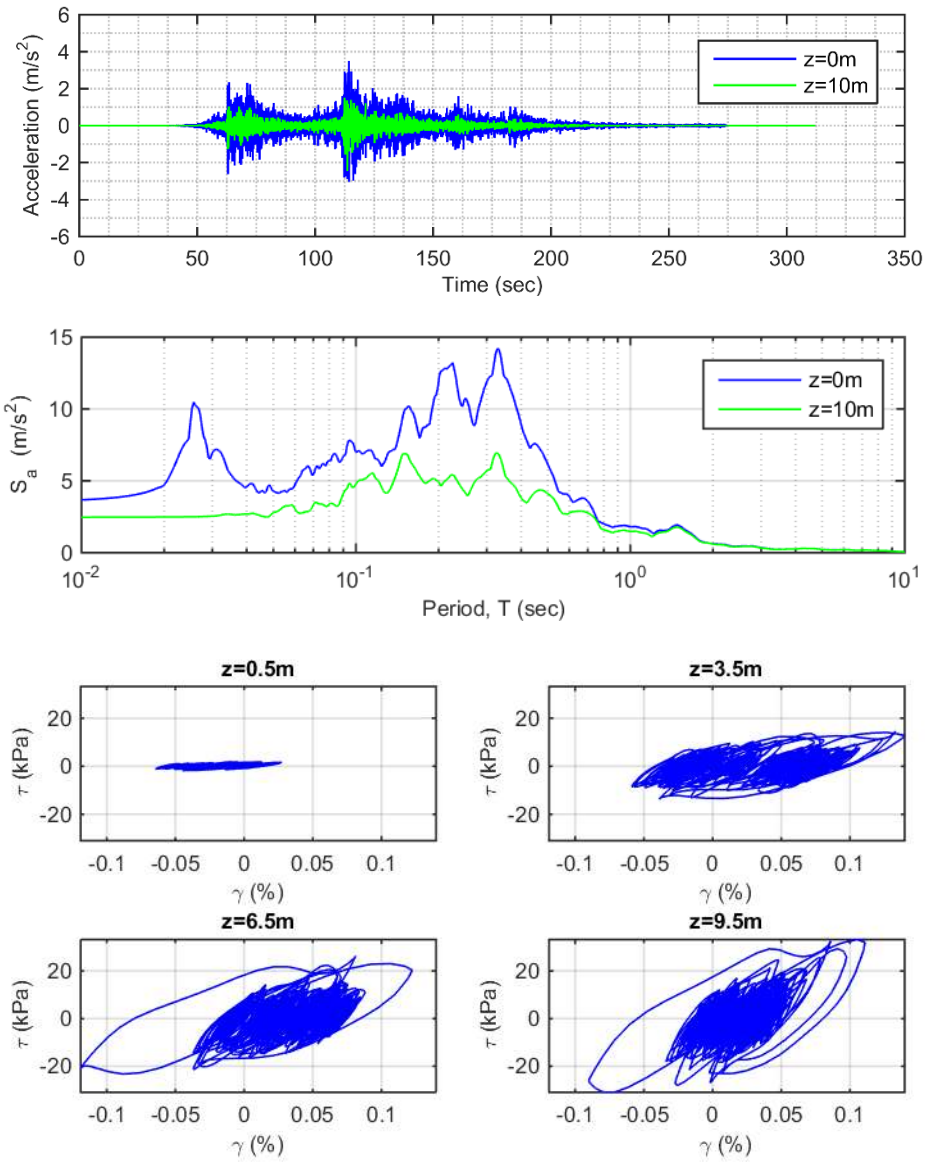

Figure 5-15: TS1 total stress acceleration time history, acceleration response spectra (5 percent damping), and stress-strain loops

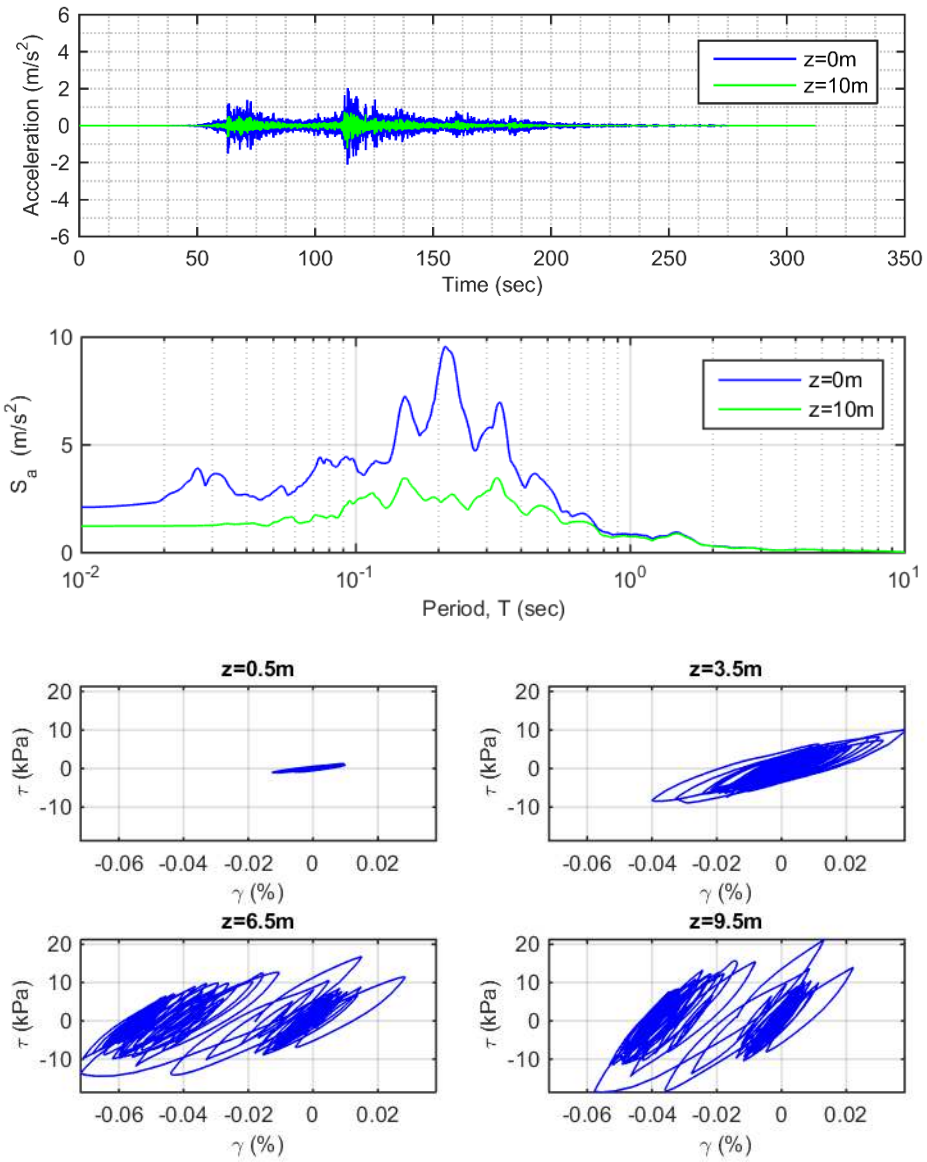

Figure 5-16: TS1-050 total stress acceleration time history, acceleration response spectra (5 percent damping), and stress-strain loops

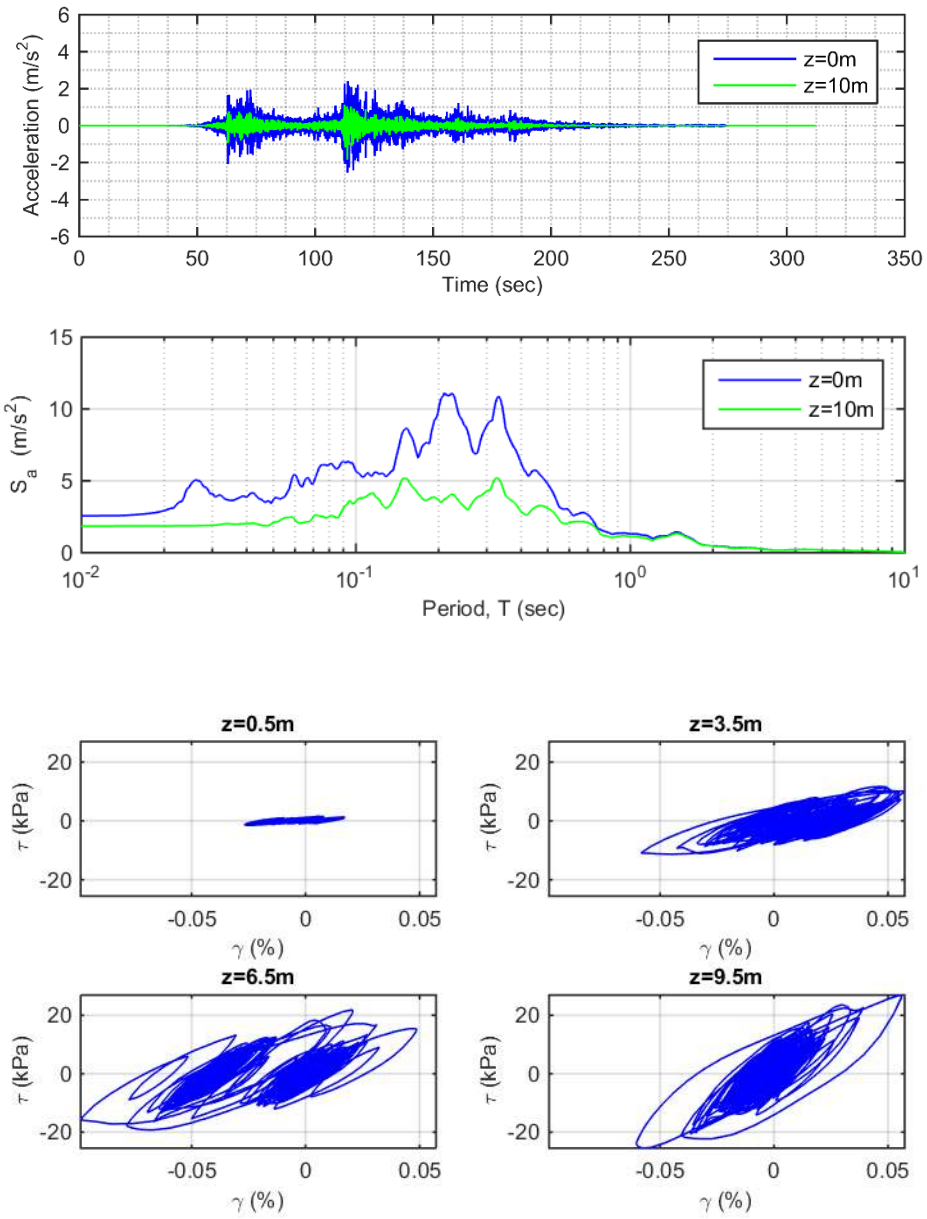

Figure 5-17: TS1-075 total stress acceleration time history, acceleration response spectra (5 percent damping), and stress-strain loops

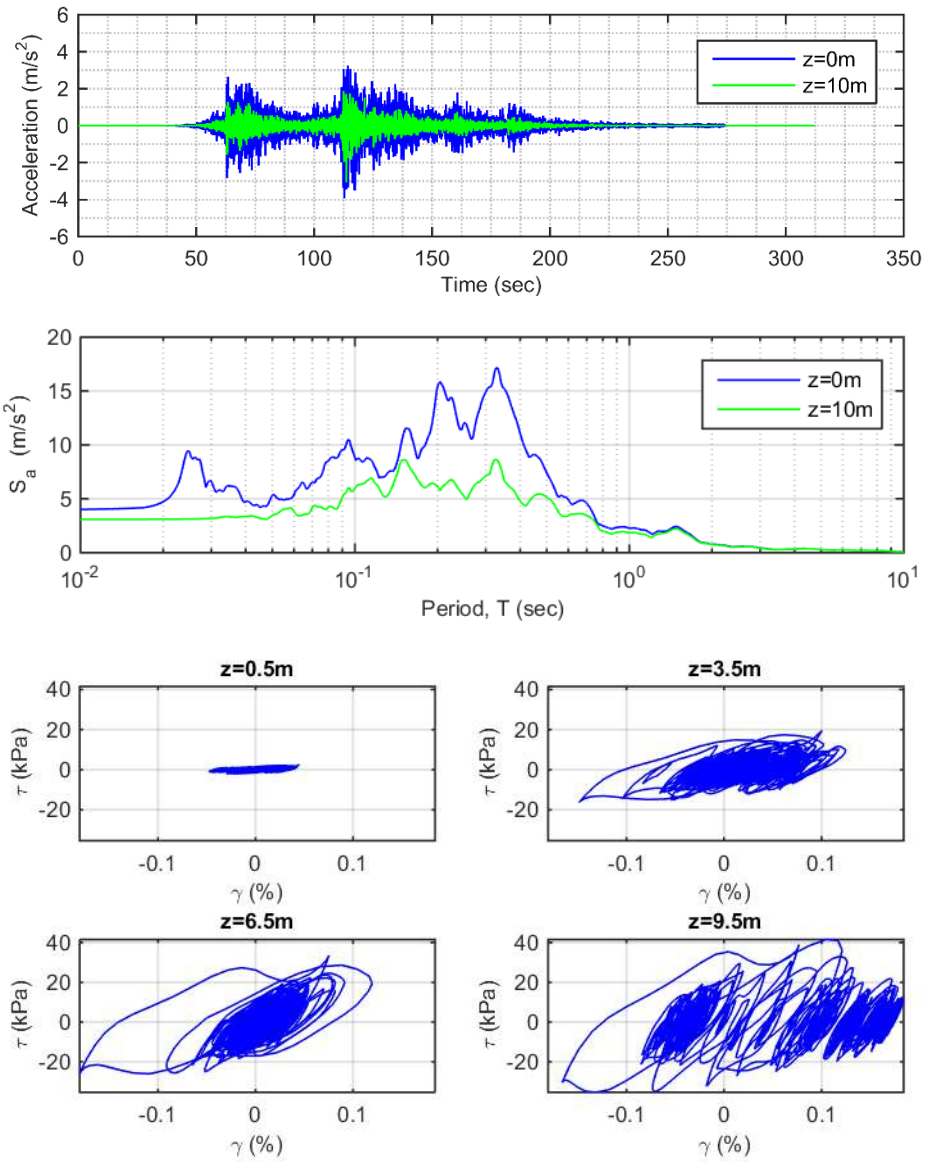

Figure 5-18: TS1-125 total stress acceleration time history, acceleration response spectra (5 percent damping), and stress-strain loops

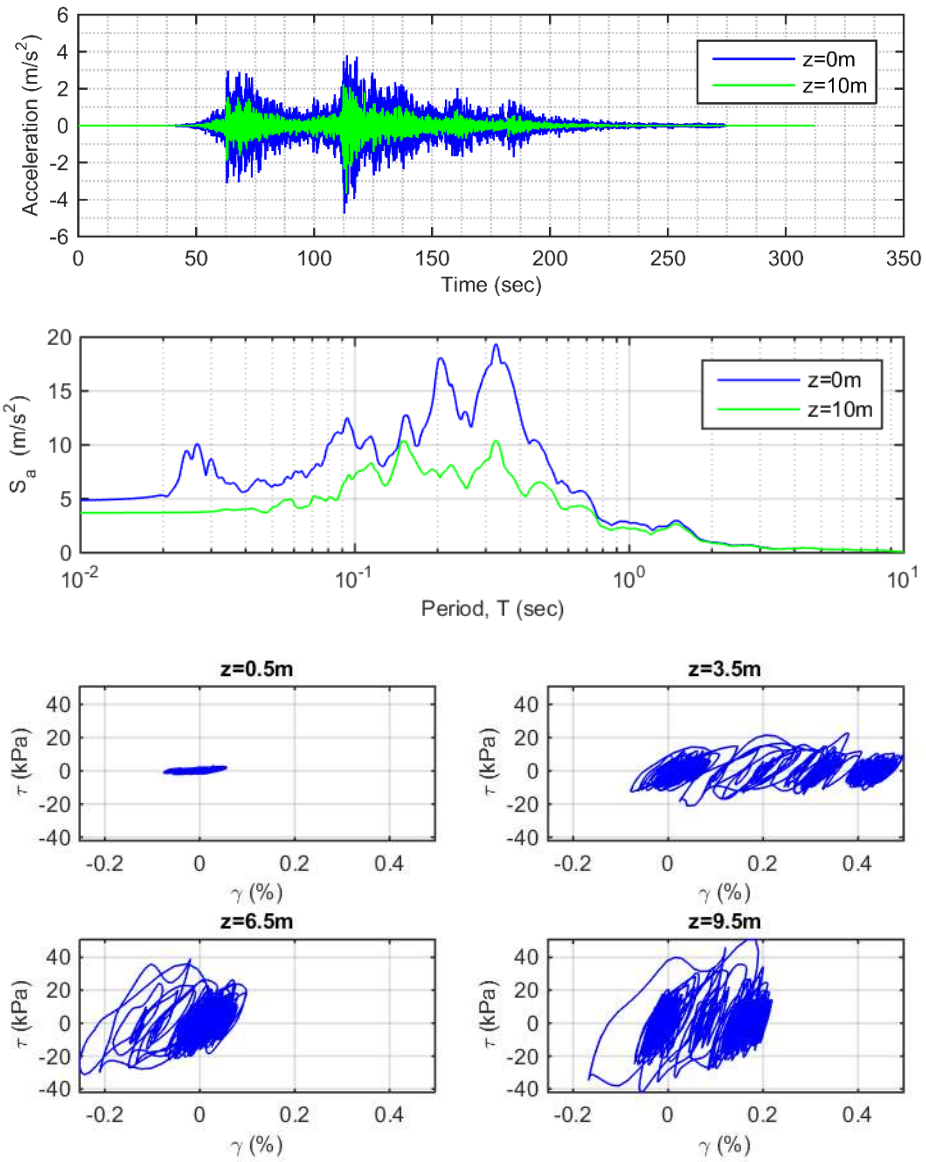

Figure 5-19: TS1-150 total stress acceleration time history, acceleration response spectra (5 percent damping), and stress-strain loops

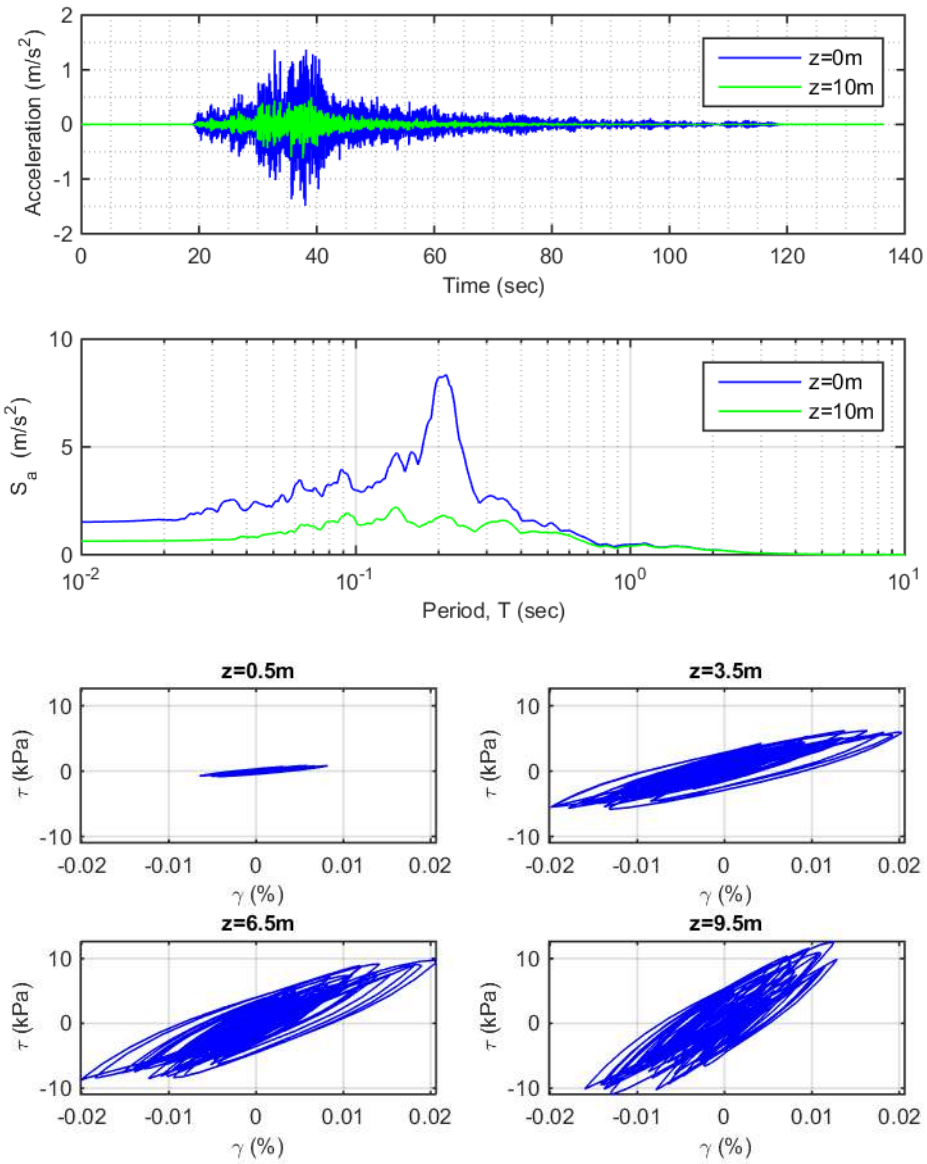

Figure 5-20: TS2 total stress acceleration time history, acceleration response spectra (5 percent damping), and stress-strain loops

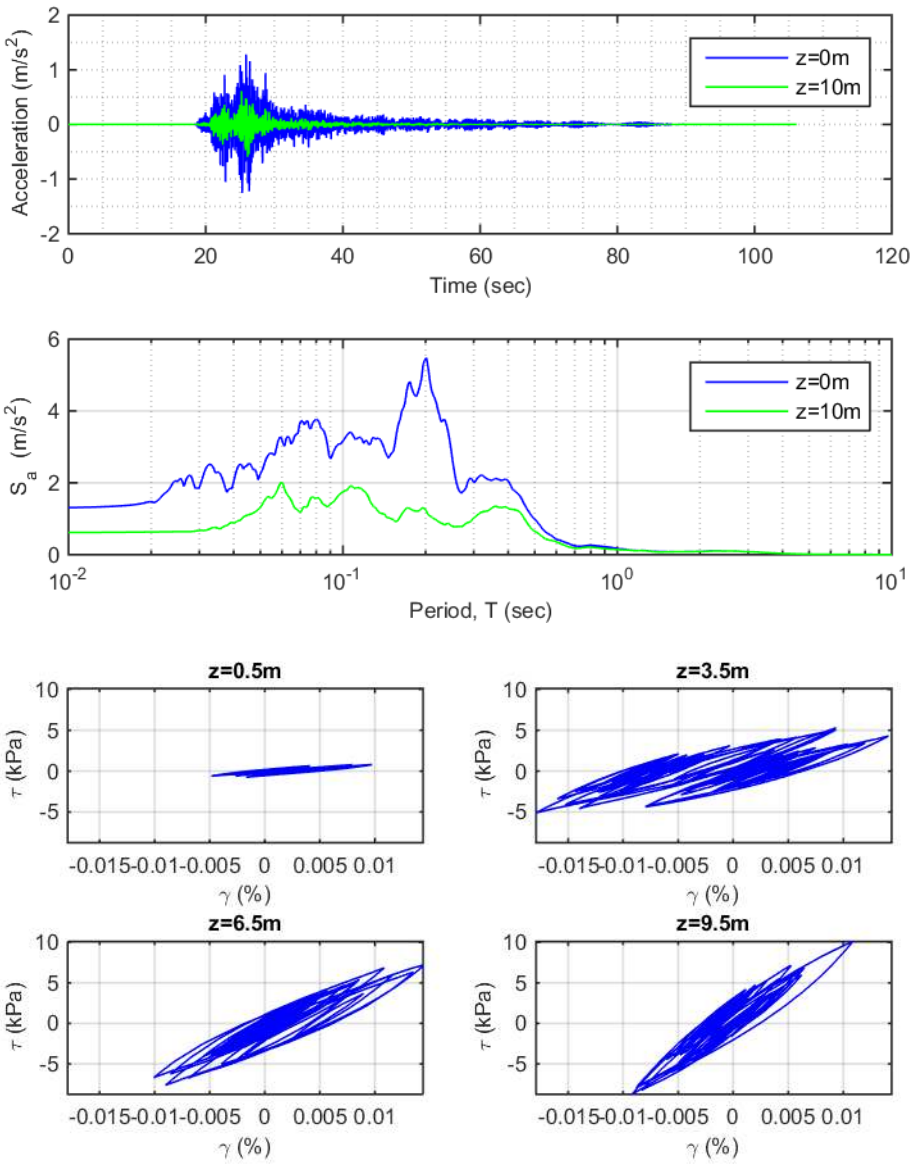

Figure 5-21: TS3 total stress acceleration time history, acceleration response spectra (5 percent damping), and stress-strain loops

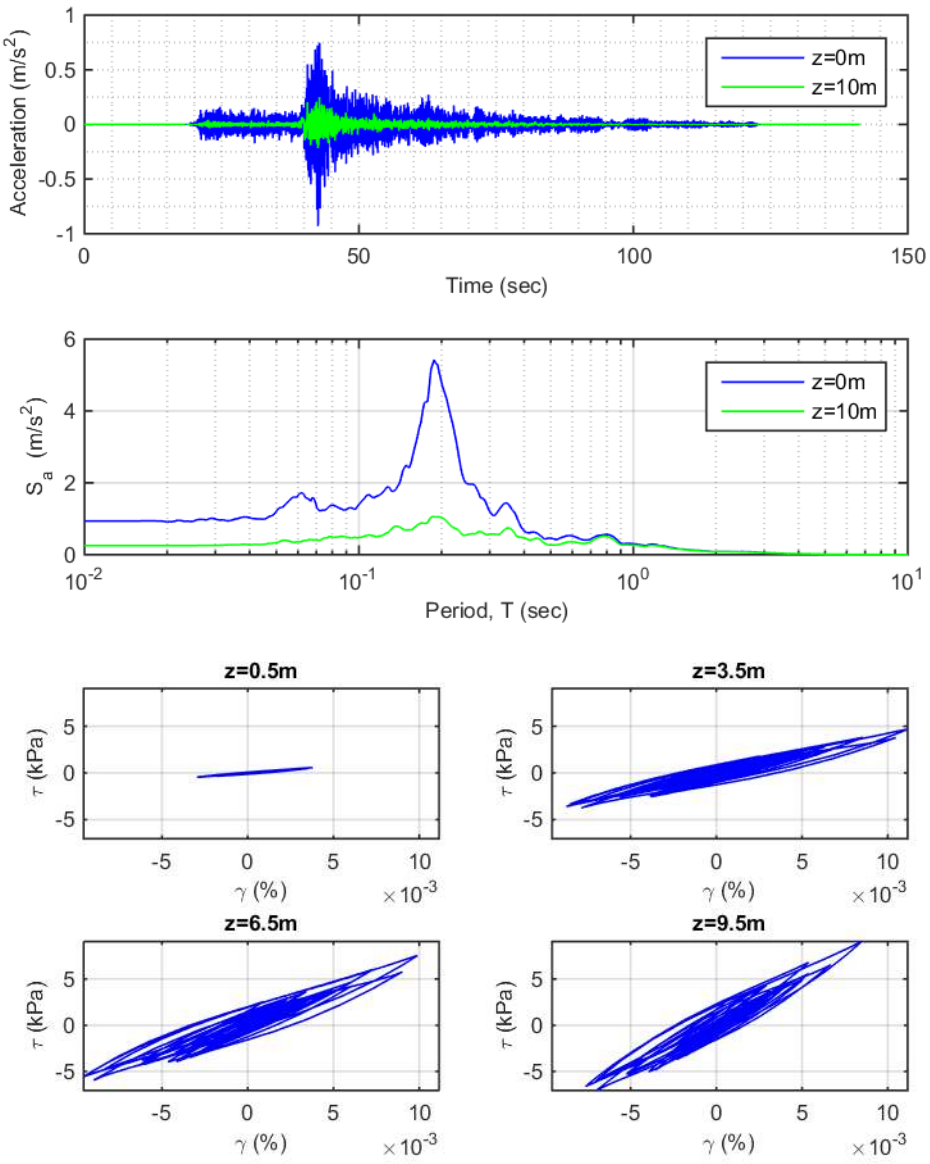

Figure 5-22: TS4 total stress acceleration time history, acceleration response spectra (5 percent damping), and stress-strain loops

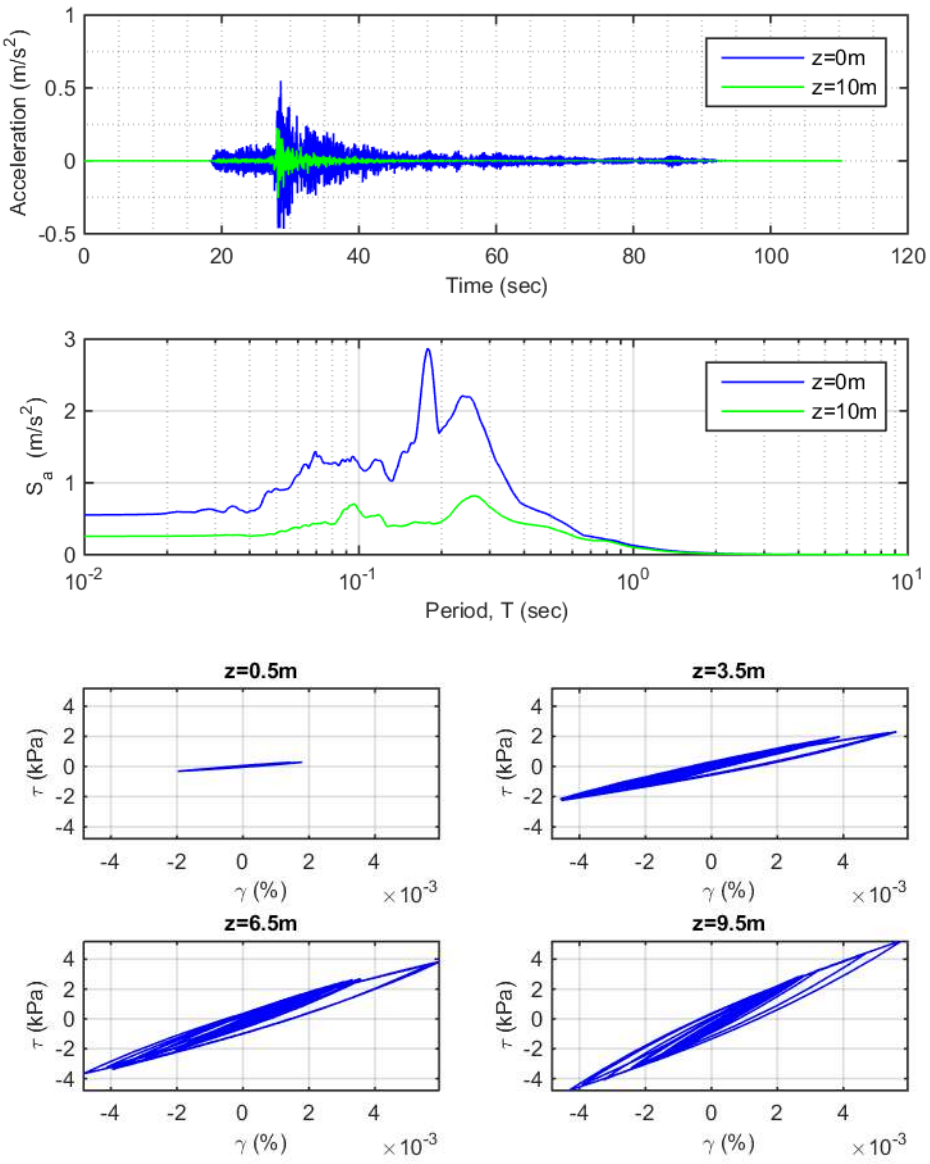

Figure 5-23: TS5 total stress acceleration time history, acceleration response spectra (5 percent damping), and stress-strain loops

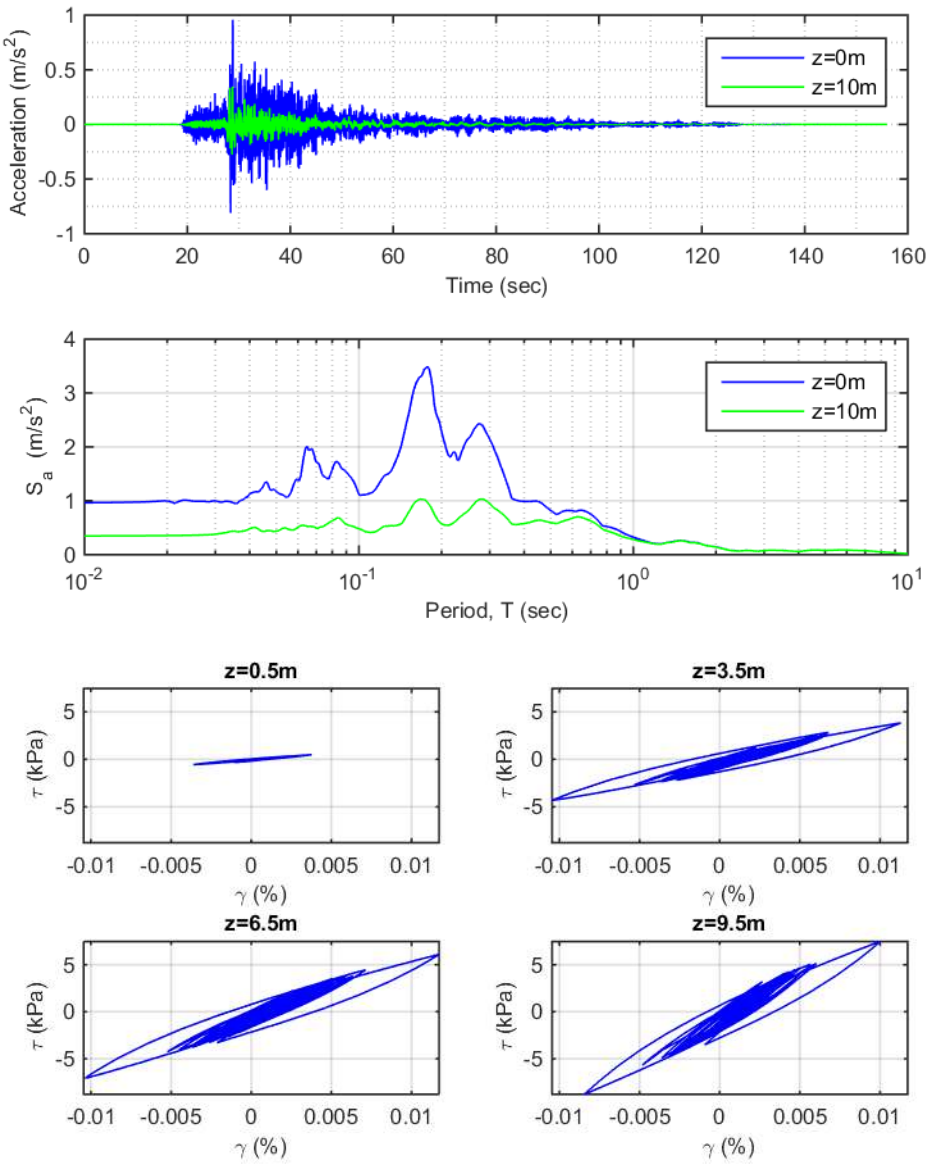

Figure 5-24: TS6 total stress acceleration time history, acceleration response spectra (5 percent damping), and stress-strain loops

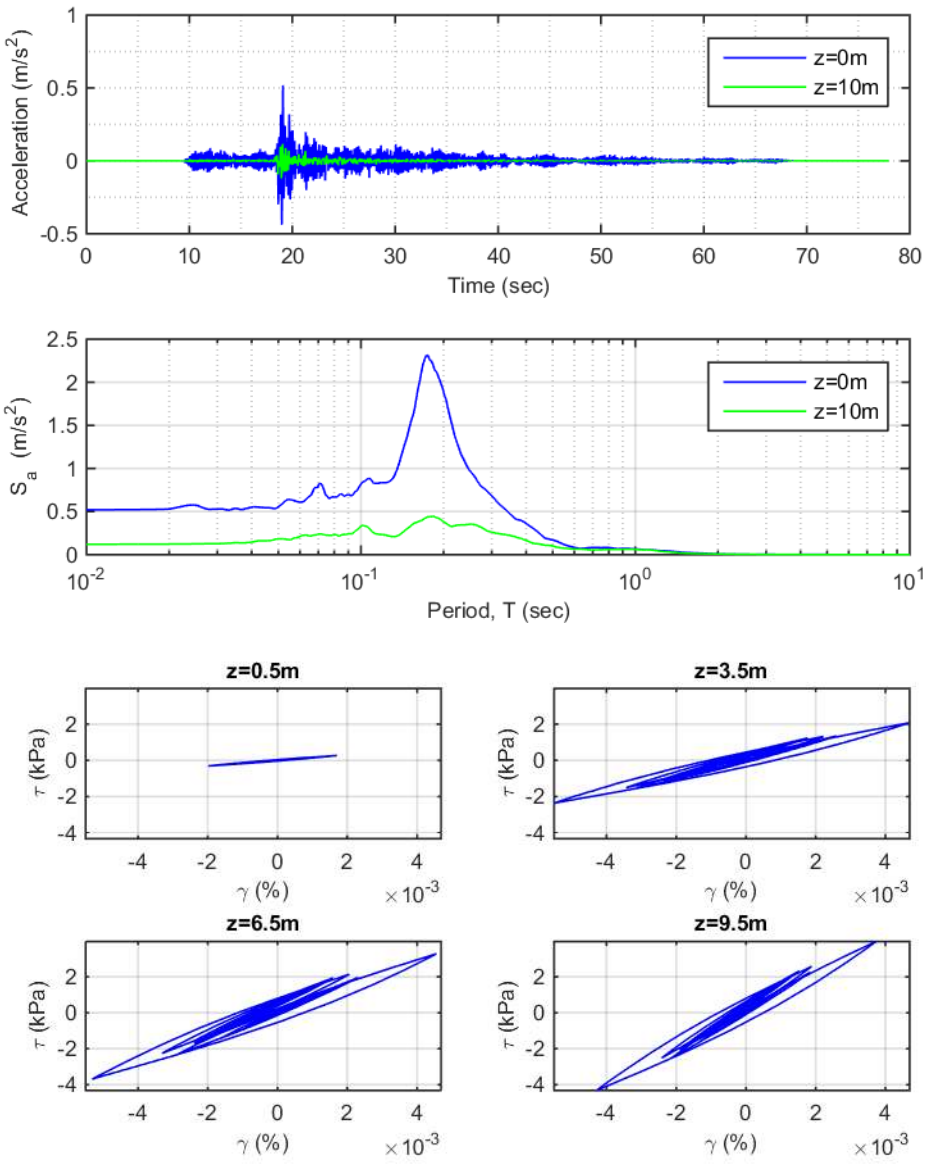

Figure 5-25: TS7 total stress acceleration time history, acceleration response spectra (5 percent damping), and stress-strain loops

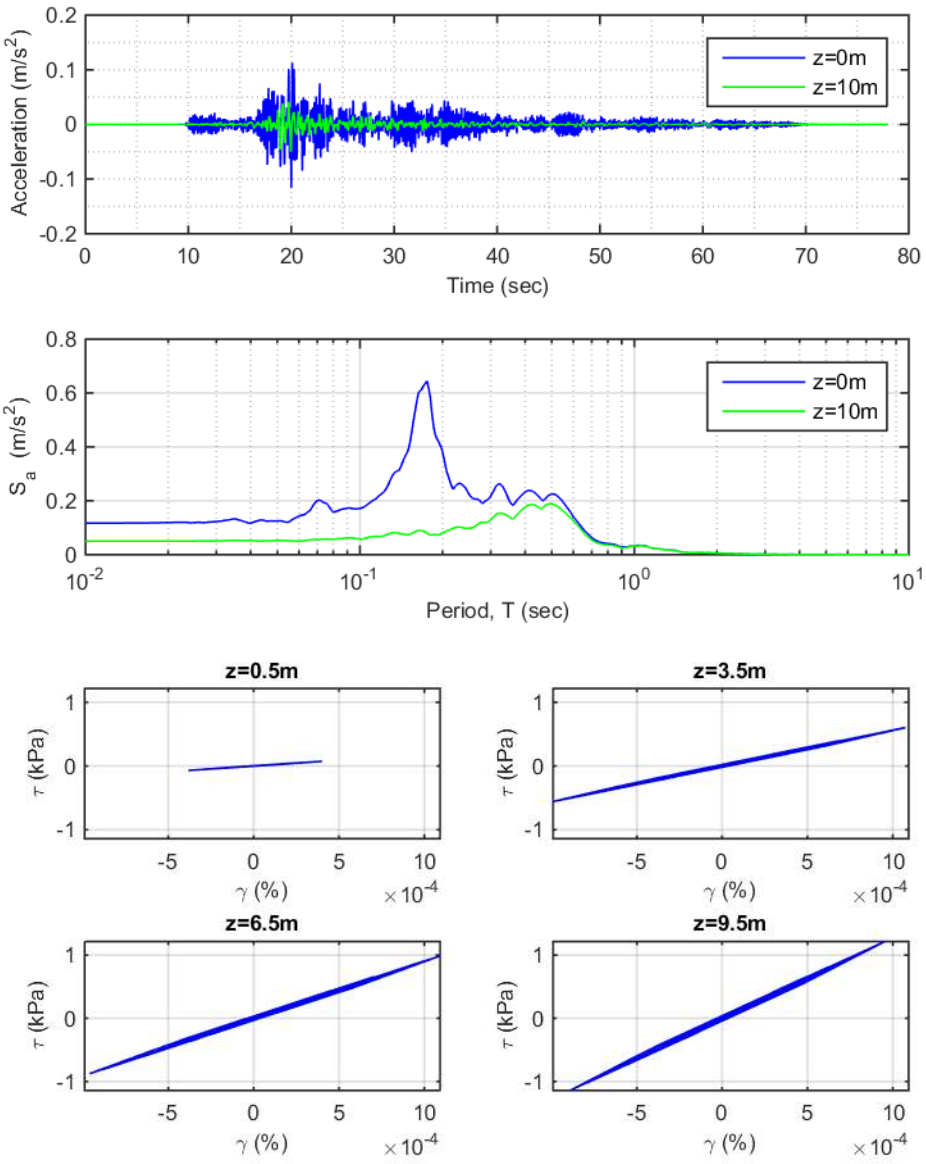

Figure 5-26: TS8 total stress acceleration time history, acceleration response spectra (5 percent damping), and stress-strain loops

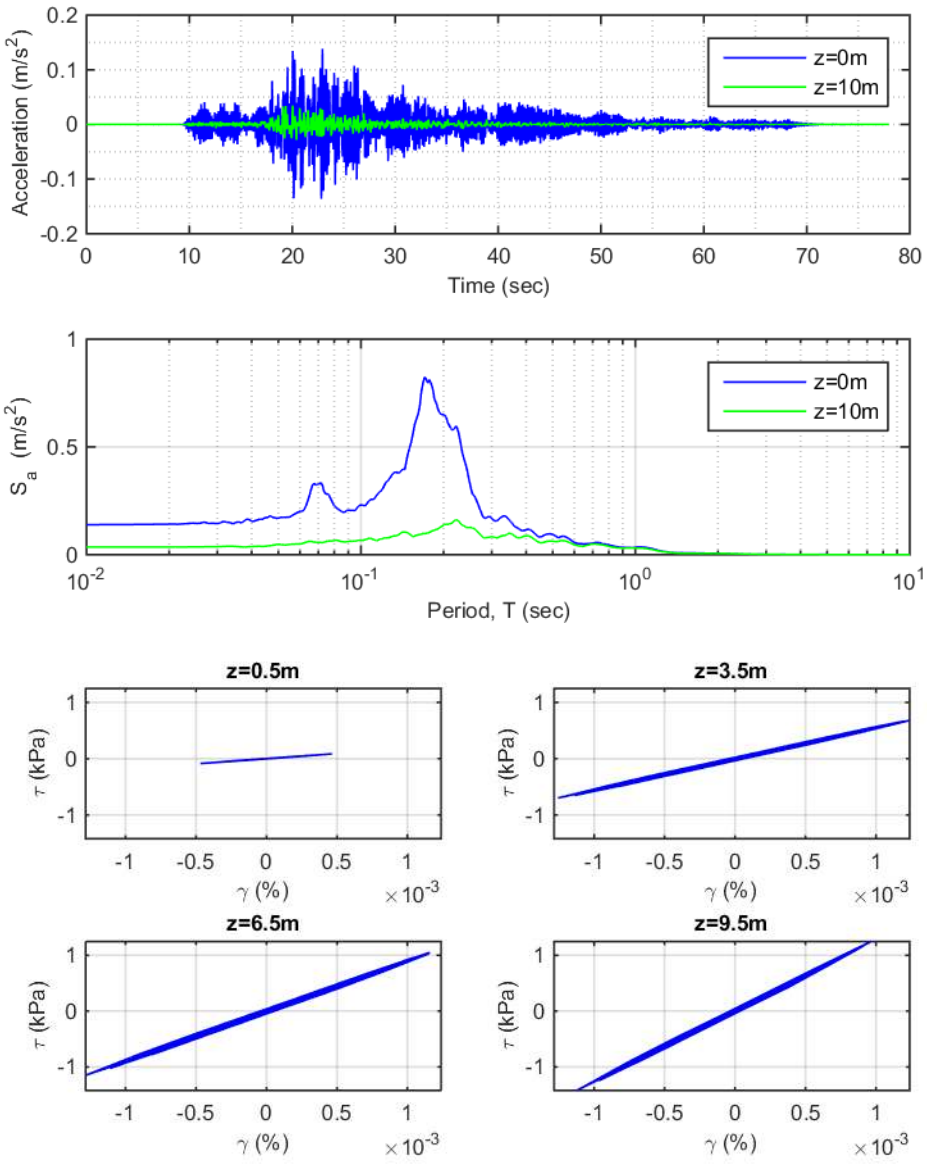

Figure 5-27: TS9 total stress acceleration time history, acceleration response spectra (5 percent damping), and stress-strain loops

5.5 Comparison of Effective and Total Stress Analyses

To compare the different horizontal PGA values simulated with the effective and total stress nonlinear seismic ground response analyses of the generic site, Figure 5-28 plots the input PGA at the base of the soil column and the computed PGA at the surface of the soil column for each of the input time series.

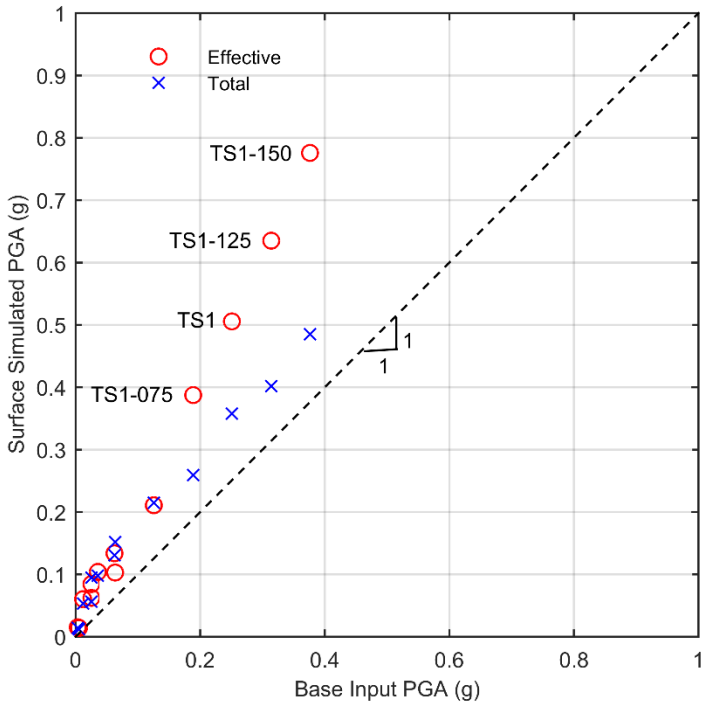

Figure 5-28: Comparison of surface horizontal PGAs computed with total and effective stress analyses

Figure 5-28 illustrates that the surface simulated PGA is similar for both the effective and total stress nonlinear seismic ground response analyses for base input PGAs less than 0.125 g (TS1-050). As the base input PGA increases past 0.125 g, the difference between the simulated horizontal surface PGA computed with the effective and total stress analyses increases. For TS1-075 (base input PGA = 0.189 g), the difference between the total and effective stress simulated PGA at the surface is 0.13 g. For TS1-150 (base input PGA = 0.376 g), the difference between the total and effective stress simulated PGA at the surface is 0.29 g.

In order to explain the difference between the horizontal surface PGA simulated with the effective and total stress analyses when the intensity of the base input motion increases, it is

insightful to compare the acceleration response spectra developed from seismic ground response analyses for different input motions. For this purpose, the total and effective stress spectral acceleration response spectra with ξ = 5% for TS1 are plotted in Figure 5-29.

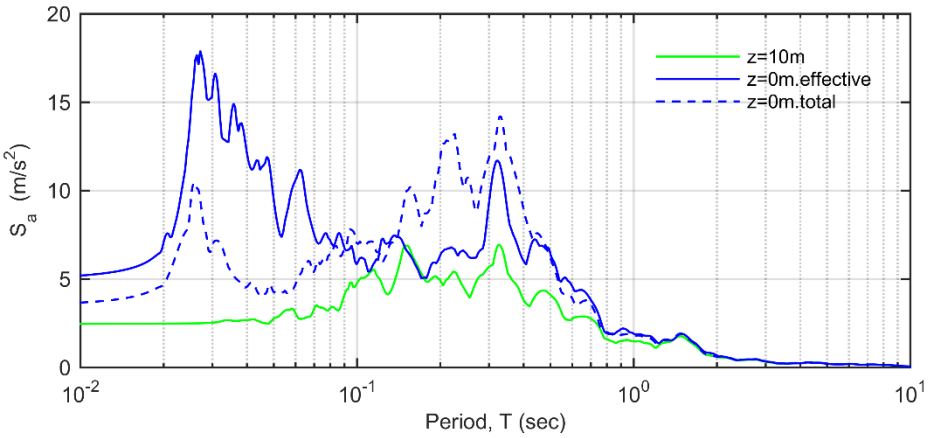

Figure 5-29: Spectral acceleration response spectra for TS1 at the base (z=10m) and surface (z=0m)

The spectral acceleration plotted in Figure 5-29 shows that the response generally changes over the period T range of interest as follows: T < 0.09 seconds (short period range) → $(S_a)_{effective} > (S_a)_{total}$ 0.09 < T < 0.5 seconds (short to intermediate period range) → $(S_a)_{effective} < (S_a)_{total}$; T > 0.5 seconds → $(S_a)_{effective} \approx (S_a)_{total}$.

For comparison with TS1 (an input motion with PGA = 0.251 g), the total and effective stress spectral acceleration response spectra with ξ = 5% for TS6 (an input motion with input PGA = 0.036 g) are plotted in Figure 5-30.

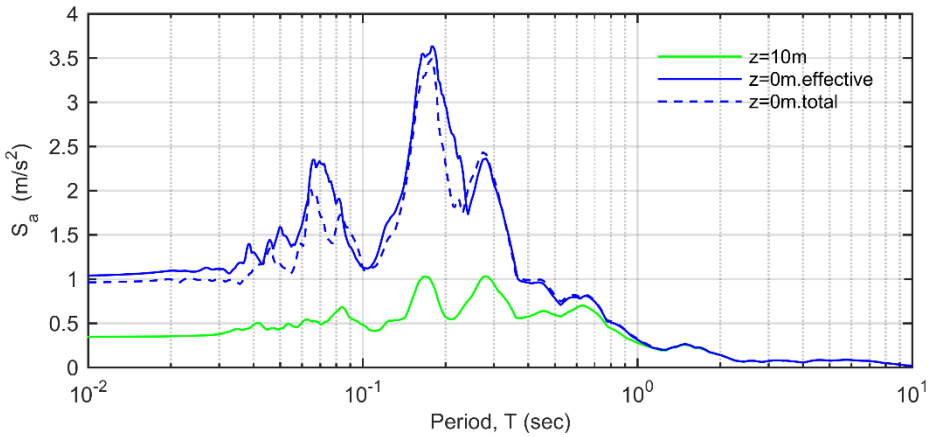

Figure 5-30: Spectral acceleration response spectra for TS6 at the base (z=10m) and surface (z=0m)

Figure 5-30 shows that the effective and total stress acceleration response spectra are very similar for TS6, explaining the similarity between the effective and total computed surface horizontal PGA at a base input of 0.036 g shown in Figure 5-28.

In order to identify the source of the difference in seismic ground response during the total and effective stress simulations of TS1, it insightful to review the acceleration and pore pressure time histories for this input motion. Particularly, it is important to note the large difference between the effective and total stress small period (high-frequency) spectral acceleration values. For the effective stress analysis, the acceleration time history in Figure 5-2 shows that starting at approximately 112 seconds, the amplitude of the input acceleration at the base of the model increases, corresponding with an approximately 37% drop in the pore pressure – relating to a drop in pore pressure from approximately 146 kPa down to approximately 92 kPa.

The spikes in the simulated acceleration time history at the surface (z = 0 m) at approximately 112 seconds are proposed to be caused by a strain stiffening shear modulus associated with a drop in pore pressure caused by soil dilatancy when the stress path begins to cross the phase transformation line identified by Ishihara (1985). This behaviour is contrary to the G/G_{max} shear modulus reduction curves often used for the calibration of soil models in seismic ground response analyses, as increased levels of strain are proposed here to result in a stiffening shear modulus as a result of soil dilatancy (Kutter and Wilson, 1999).

The simulated stress path is plotted as shear stress τ against vertical effective stress σ_v' at 9 m depth during TS1 earthquake loading in Figure 5-31.

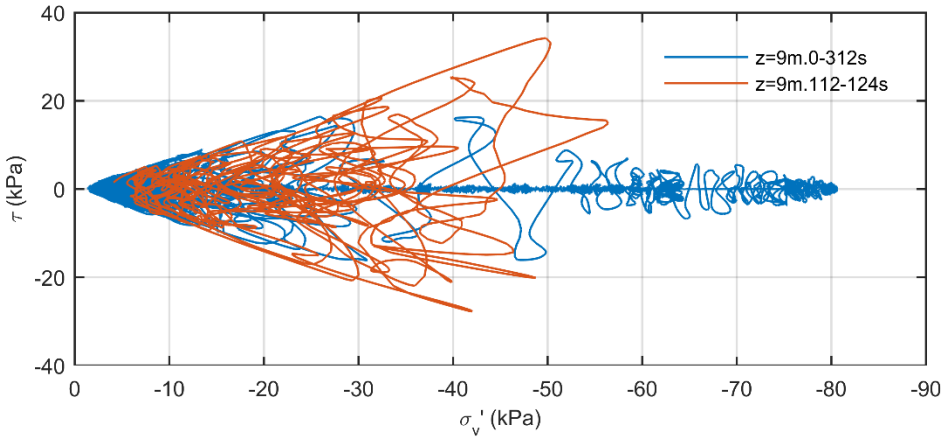

Figure 5-31: Stress path at 9 m depth during TS1 loading

The TS1 stress path is highlighted in Figure 5-31 between 112 and 124 seconds to show the stress response during the sudden drops and increases in pore water pressure as the soil changes between contractive and dilative behaviour associated with the stress path crossing the phase transformation line. The transition between contractive and dilative soil behaviour is represented by the large stress path loops which occur between 112 and 124 seconds in Figure 5-31.

Kutter and Wilson (1999) proposed the term "de-liquefaction shock waves" to describe soil stiffening due to dilatancy and identified this as a source of high-frequency acceleration pulses. Kramer et al. (2015) later referred to soil stiffening due to dilatancy as dilation pulses. To link the TS1 simulated high frequency response shown in Figure 5-29 with the dilative soil behaviour shown in Figure 5-31, the response spectra for TS1 is plotted for different periods of the time history in Figure 5-32.

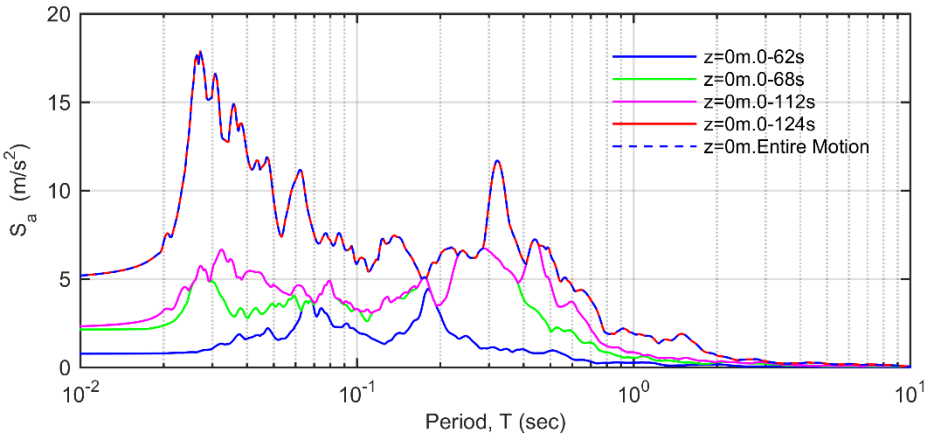

Figure 5-32: Acceleration response spectra at surface (z=0m) for TS1 at 62, 68, 112, 124s, and for the entire motion

The low period (high frequency) content of the response spectra for TS1 in Figure 5-32 is observed to increase with time up until 124 seconds, after which the response spectra for the entire motion is nearly identical to that of spectra at 124 seconds. The response spectra at 112 seconds (just before the onset of significant soil dilation) has less high frequency content than the response spectra at 124 seconds, indicating that the simulated high frequency response is primarily associated with soil dilative behaviour between 112 and 124 seconds, which is inferred from the stress path in Figure 5-31. Some less significant soil dilative behaviour, and resulting high frequency ground motion, also occurs between 62 and 68 seconds, which is observed by comparing the response spectra at these 62 and 68 seconds and the pore pressure time history in Figure 5-2.

Further evidence of high frequency acceleration pulses occurring during input motion TS1 can be observed by qualitatively evaluating the time-frequency representation of the simulated ground surface motion. Figure 5-33 shows the time-frequency spectrum for the ground motion TS1 at the surface of the site (z=0m) developed using the continuous wavelet transform time-frequency technique. The time-frequency spectrum is shown in colour scale, with the motion's frequency content qualitatively increasing from blue to red.

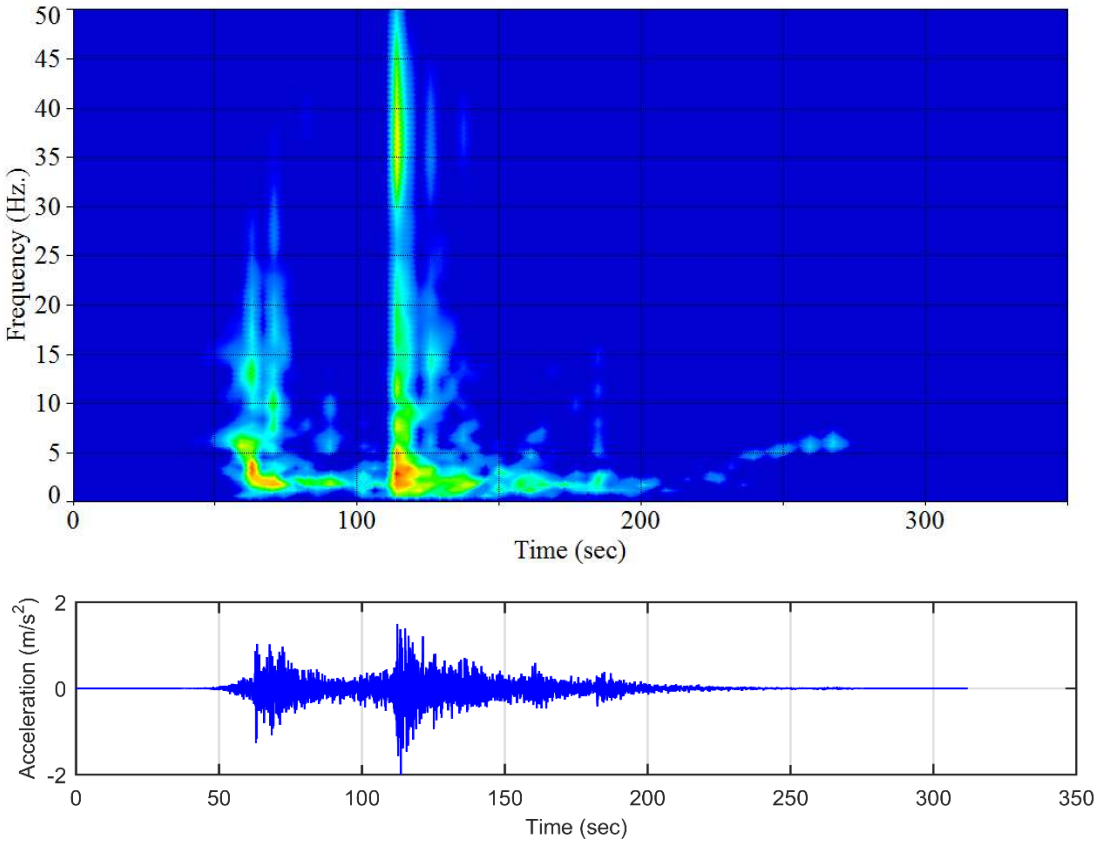

Figure 5-33: TS1 time-frequency spectrum at z=0m – frequency content increasing from blue to red

Figure 5-33 shows significant increases in high frequency motion content between 30 to 50 Hz. at approximately 110 seconds. This corresponds well with the time where high frequency response is postulated to be associated with soil dilation based on Figure 5-31 and Figure 5-32. After approximately 125 seconds, Figure 5-33 shows that the frequency content of the remaining motion is primarily within the range of approximately 1 to 5 Hz.

For comparison with the response of TS1, the time-frequency spectrum for the response of the site surface (z=0m) to input motion TS6 is plotted in Figure 5-34.

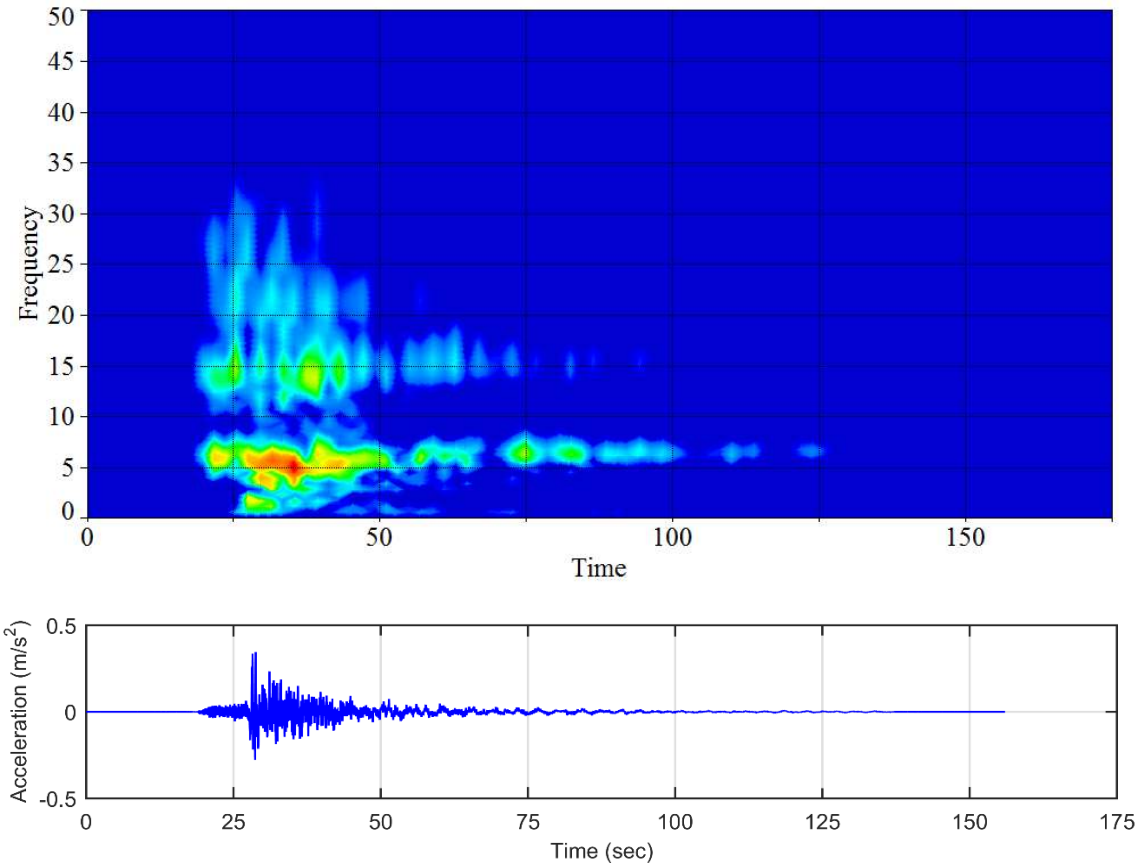

Figure 5-34: TS6 time-frequency spectrum at z=0m – frequency content increasing from blue to red

Qualitative evaluation of the time-frequency spectrum in Figure 5-34 indicates that TS6 does not exhibit the significant increases in high-frequency ground motion content that are observed for TS1. This is considered to corroborate the previous finding that the ground response when subjected to input motion TS6 does not generate high frequency pulses as a result of soil dilation and, as a result, the total and effective stress simulations for TS6 are similar.

Soil dilation was identified as the source of high frequency motion at Onahama Port near Iwaki, Japan during the 2011 Tohoku M_w 9.0 earthquake by Roten et al. (2013). High-frequency ground amplification appears to be particularly important when shallow soft surface soil layers are considered (Finn and Ruz 2015). The analyses presented here support these findings and point towards the SANISAND model as being capable of reproducing high frequency ground motion associated with soil dilation, and also highlight the potential for high frequency

motions to govern ground surface PGA when shallow sands susceptible to dilative behaviour are subject to a seismic event.

The soil-solid and pore water fluid interaction in the effective stress analyses is shown by the results presented above to be a significant factor contributing for the dynamic response of soil to earthquake motions with increasing PGA. In general, the total and effective stress analyses provided similar predictions of surface PGA at the generic site when the site was subjected to input ground motions with lower PGAs (TS2 through TS9). However, the difference between the total and effective stress computed motions became more significant as the ground motion intensity increased (TS1-050 through TS1-150). The primary cause of the different horizontal PGAs predicted by the effective and total stress analyses at the surface of the shallow generic site is proposed to be caused by dilative soil behaviour. This finding also highlights the importance of considering the depth, or natural period, of the site as deep sand sites would most likely tend to have a different effect on the earthquake motion.

Chapter 6: Conclusion and Future Research

6.1 Conclusions

Evaluating the propagation of seismic waves through local site soils and predicting the resulting ground motions is one of the most important problems encountered in geotechnical engineering. Local soil conditions change the frequency content of seismic motion and amplify or de-amplify the motion, depending on the characteristics of the site.

The equivalent linear method is often used in geotechnical engineering practice for the purpose of carrying out seismic ground response analyses. However, this technique relies on empirical or experimental G/G_{max} shear modulus reduction and damping ratio curves for a given soil type, and cannot account for important aspects of real soil behaviour such as volumetric strain, dilation and pore pressure generation. Additionally, because equivalent linear models treat the soil as a linear viscoelastic material, they cannot be used for problems involving irrecoverable strain or failure, such as the important dynamic soil phenomenon of liquefaction during a seismic event. Also, the equivalent linear method has no provision to account for the development of porewater pressures during seismic shaking, and the interaction of the pore fluid and soil skeleton cannot be simulated.

More accurate methods of representing soil behaviour during an earthquake event are based on nonlinear advanced constitutive models. However, these models historically have been less used in geotechnical engineering practice due to their perceived complexity and uncertainty regarding usage protocols. This thesis has intended to achieve the following three main objectives:

- Use the recently implemented bounding surface constitutive model SANISAND in the finite element program OpenSees to carry out and evaluate total and effective stress nonlinear ground response analyses of shallow sand sites. In doing so, provide some direction to future users of the SANISAND model on the protocols for use of the model when carrying out seismic ground response analyses.

- Carry out validation analyses to assess the ability of the SANISAND model to simulate recorded earthquake ground motions as part of the PRENOLIN project.
- Explore the ability of the SANISAND model to simulate complex seismic ground response phenomenon such as dilation pulses during a seismic event.

The continuum model for the seismic ground response analyses carried out for this research used the SANISAND constitutive model to represent the nonlinear hysteretic behaviour of sandy soils. The earthquake motions, laboratory and field data used in the seismic ground response analyses of the Sendai site presented in Chapter 4 were provided as part of PRENOLIN project.

The development of the continuum model for the seismic ground response analyses in Chapter 4 involved detailed calibration of the SANISAND model to monotonic and cyclic triaxial test data. During the calibration procedures, the significant importance of accurately capturing the SANISAND G_0 constant for the evaluation of the shear modulus at a real site was identified. It was determined that for application of calibration procedures to a real site, conventional cyclic triaxial tests cannot be used for the purpose of evaluating the SANISAND G_0 parameter, as sample disturbance and strain levels induced during conventional triaxial testing result in constant G_0 values which underestimate the in situ small-strain shear modulus in the field. To adequately capture the shear stiffness of the site, the G_0 constant of the SANISAND model used in this research had to be back-calculated to in situ shear wave velocity data. This research was unable to carry out seismic ground response analyses using a single value of G_0 based on laboratory calibration. More success with calibration of the SANISAND G_0 parameter based on laboratory data may be achieved by measuring small strain levels in the laboratory with bender elements or the resonant column test. Nonetheless, back-calculation of the G_0 parameter to in situ shear velocity measurements appears to be a viable method for determining G_0.

The SANISAND model is based on the framework of Critical State Soil Mechanics, and the model can be calibrated to a single set of laboratory data to simulate the response of a specific soil under a wide variety different conditions. The calibration procedures carried out for the

SANISAND model in this thesis showed that a single set of model constants could be selected to represent the soil conditions at a real site, based on calibration to monotonic and cyclic triaxial tests conducted by the OYO Corporation (2014). With the exception of the G_0 model constant as discussed above, a single set of model parameters was used in the seismic ground response analyses and there was no need to recalibrate the model for different confining pressures or depths. This is an advantage of the SANISAND model over other more empirical constitutive models for sands which require calibration of a new set of model constants for the same soil at different confining pressures or densities.

The continuum model configuration, element type, constitutive material behaviour, boundary conditions, loading pattern and equation solvers were evaluated by simulating the seismic response of the Sendai site during nine different earthquake motions recorded at the Sendai downhole seismograph network. The computed and recorded motions were compared in Chapter 4 to show that the SANISAND constitutive model was able to adequately simulate the nonlinear hysteretic behaviour of the soil column during seismic loading.

The continuum model was developed to compare both total and effective seismic ground response analyses using the SANISAND model. The influence of soil permeability in the effective stress analyses was shown to be influential in the dynamic response of soil to earthquake motions with increasing PGA. In general, the total and effective stress analyses provided similar predictions of horizontal surface PGA when subject to smaller input motions (TS3 through TS 9). However, the difference between the horizontal surface PGA predicted with the total and effective stress analyses became more significant as ground motion intensity increased for TS1 and TS2. Also, the effective stress analyses provided a better prediction of the spectral acceleration values for the majority of motions. Evidently, the effective stress application of the SANISAND model for the prediction of ground motions during an earthquake event is a more reliable method of carrying out seismic ground response analyses. This is particularly the case when medium to large strain accumulation is expected during a seismic event.

For the purpose of further evaluating total and effective stress seismic ground response analyses when seismic waves propagate through a shallow sand site, Chapter 5 of this thesis presented seismic ground response analyses on a generic site analyzed in OpenSees using thirteen different input earthquake motions. These analyses used the SANISAND model calibrated to Toyoura sand to represent a 10 m deep layer of medium dense sand saturated below the water table at 2 m depth, and were completed using the same element types, boundary conditions, constitutive materials, loading patterns and equation solvers described for the Sendai site in Chapter 4 of this thesis.

The Chapter 5 analyses showed that modeling the solid-pore fluid interaction during the seismic response analysis of a 10 m deep site was particularly important when medium dense sands may be subject to cyclic mobility and a strain-stiffening response during earthquake loading, resulting in soil dilation and high frequency acceleration pulses. This type of behaviour is consistent with recent observations of increased ground amplification at frequencies above 10 Hz. during the 2011 Tohoku earthquake (Roten et al. 2013). Soil dilative behaviour and a strain-stiffening response was inferred to govern the simulated PGA as ground motion intensity increased. This is in contrast to the conventional shear modulus reduction curves commonly used for the calibration of nonlinear soil models which are based on the soil shear modulus reducing with increasing levels of strain (Kutter and Wilson 1999).

The total stress analyses of Chapter 5 were unable to simulate soil dilatancy associated with the stress path crossing the phase transformation line as the generation of pore pressure during seismic shaking was not accounted for in the total stress model. As a result, the total stress analyses could not capture the high frequency motion observed during the effectives stress analyses to be caused by dilative soil behaviour. Consequently, total stress analyses can possibly underestimate the horizontal PGA at the surface of a shallow sand site.

6.2 Future Research

While the work presented in this thesis has contributed to the understanding of the application of the SANISAND constitutive model for the representation of hysteric stress-strain behaviour of soil in seismic ground response analyses, and has highlighted the ability of the SANISAND

model to predict complex dynamic soil behaviour, it has also identified a number of items which warrant additional research. These items are as follows:

- The calibration of the SANISAND model has been carried for a limited number of different soil types. The calibration work completed in this research was carried out for conventional monotonic and cyclic triaxial tests and identified these tests as being inadequate for calibration of the small-strain model response. Future calibration of the SANISAND model should be carried out for different soil types using a series of laboratory tests capable of capturing the small-strain shear response of the soil. Preferably, the laboratory testing would include cyclic triaxial tests with bender elements or resonant column tests.
- Work completed to date on the calibration of the SANISAND model has focused on laboratory triaxial tests. Research into developing correlations for the calibration of the SANISAND model should be completed based on commonly used in situ test methods in geotechnical engineering practice such as the Standard Penetration Test (SPT) and Cone Penetration Test (CPT) with shear wave velocity measurements. This may result in the SANISAND model being a more practical alternative for use in real engineering design.
- In depth research exploring liquefaction with the SANISAND model should be carried out.
- The work of this thesis considered one-dimensional seismic ground response analyses with finite elements based on a plane strain formulation. OpenSees has a variety of three-dimensional element types which are capable of carrying out effective stress analyses with the SANISAND model. Research into the application of three-dimensional seismic ground response analyses using the SANISAND model should be carried out. Such research could consider basin effects, slopes and other three-dimensional geometries.
- Stochastic analyses which explores seismic ground response using the SANISAND model to quantify the uncertainty associated with the model input parameters and to identify those parameters which contribute most significantly to the prediction of

ground motions during a seismic event should be completed. This work should quantify the statistical variability of the model parameters and the sensitivity of the seismic ground response to variations in these parameters.

Bibliography

Atkinson, J. (2000). Non-linear soil stiffness in routine design. *Geotechnique,* 50(5):487-508.

Bardet, J.P, Ichii, K., and Lin, C.H. (2000). EERA – A computer program for equivalent-linear earthquake site response analyses of layered soil deposits. Department of Civil Engineering, University of Southern Carolina.

Been, K. and Jefferies, M.G. (1985). A state parameter for sands. *Geotechnique,* 35(2):99-112.

Biot, M.A. (1941). General theory of three dimensional consolidation. *Journal of Applied Physics,* 12(2):155-164.

Biot, M.A. (1956). Theory of propagation of elastic waves in a fluid-saturated porous solid. T*he Journal of the Acoustical Society of America,* 28(2):168-178.

Biot, M.A. (1962). Mechanics of deformation and acoustic propagation in porous media. *Journal of Applied Physics* 33(4):1482–1498.

Dafalias, Y.F. and Manzari, M.T. (2004). Simple plasticity sand model accounting for fabric change effects. *Journal of Engineering Mechanics*, 36(1):65-78.

Dafalias, Y.F., Papadimitriou, A.G., and Li, X.S. (2004). Sand plasticity model accounting for inherent fabric anisotropy. *Journal of Engineering Mechanics,* 130(11):1319-1333.

Darendeli, M.B. (2001). *Development of a new family of normalized modulus reduction and material damping curves*. PhD thesis, The University of Texas at Austin.

Finn, W.D.L. and Ruz, F. (2015). Amplification effects of thin soft surface layers: a study for NBCC 2015. *Perspectives in Earthquake Geotechnical Engineering,* Springer International Publishing, 33-44.

Hardin, B.O. and Drnevich, V.P. (1970). Shear Modulus and Damping in Soils-II: Design Equations and Curves. *Technical Report No. UKY 27-70-CE3*, *Soil Mechanics Series No.2*, College of Engineering, University of Kentucky.

Howie, J.A. and Campanella, R.G. (2005). Guidelines for the use, interpretation and application of seismic piezocone test data. Geotechnical Research Group, Department of Civil Engineering, University of British Columbia.

Ishihara, K., Tatsuoka, F., and Yasuda, S. (1975). Undrained deformation and liquefaction of sand under cyclic stresses. *Soils and Foundations,* 15(1):29-44.

Ishihara, K. (1985). Stability of natural deposits during earthquakes. *Proceedings of the 11th International Conference on Soil Mechanics and Foundation Engineering,* 321-376.

Ishihara, K. (1996). *Soil behaviour in earthquake geotechnics.* Oxford University Press, New York, New York, USA.

Jaky, J. (1944). The coefficient of earth pressure at rest. *Journal of the Society of Hungarian Architects and Engineers,* 78(22):355-358.

Joyner, W.B. and Chen, A.T.F. (1975). Calculation of nonlinear ground response in earthquakes. *Bulletin of Seismological Society of America,* 65(5):1315-1336.

Kramer, S.L. (1996). *Geotechnical Earthquake Engineering.* Prentice-Hall, Upper Saddle River, New Jersey, USA.

Kramer, S.L., Asl, B.A., Ozener, P., and Sideras, S.S. (2015). Effects of liquefaction on ground surface motions. *Perspectives in Earthquake Geotechnical Engineering* (Ansal and Sakr eds.), Springer International Publishing, 285-309.

Kutter, B.L. and Wilson, D.W. (1999). De-liquefaction shock waves. *Proceedings of the 7th U.S.-Japan Workshop on Earthquake Resistant Design for Lifeline Facilities and Countermeasures Against Soil Liquefaction, Technical Report MCEER-99-0019* (O'Rourke, Bardet, and Hamada eds.), 295-310.

Li, X.S. and Dafalias, Y.F. (2011). Anisotropic critical state theory: role of fabric. *Journal of Engineering Mechanics,* 138(3):263-275.

Li, X.S. and Wang, Y. (1998). Linear representation of steady-state line for sand. *Journal of Geotechnical and Geoenvironmental Engineering,* 124(12):1215-1217.

Li, X.S. and Dafalias, Y.F. (2000). Dilatancy of cohesionless soils. *Geotechnique,* 50(4):449-460.

Lysmer, J., and Kuhlemeyer, A.M. (1969). Finite dynamic model for infinite media. *Journal of Engineering Mechanics,* ASCE, 95:859-877.

Manzari, M.T. and Dafalias, Y.F. (1997). A critical state two-surface plasticity model for sands. *Geotechnique,* 47(2):255-272.

Marot, M. (2015). *PRENOLIN – Validation Phase, Iteration 2: Sendai Input Motions.*

Mazzoni, S., McKenna, F., Scott, M.H., Fenves, G.L. (2007). *The OpenSees command language manual.* Pacific Engineering Research Center, University of California, Berkeley.

McGann, C. and Arduino, P. (2011a). *Site Response Analysis of a Layered Soil Column (Total Stress Analysis).* available from http://opensees.berkeley.edu/wiki/index.php/Site_Response_ Analysis_ of_a_Layered_Soil_Column_(Total_Stress_Analysis).

McGann, C. and Arduino, P. (2011b). *Effective Stress Response Analysis of a Layered Soil Column.*. available from http://opensees.berkeley.edu/wiki/index.php/Effective_Stress_Site_ Response_Analysis_of_a_Layered_Soil_Column.

McGann, C.R., Arduino, P., and Mackenzie-Helnwein, P. (2012). Stabilized single-point 4-node quadrilateral element for dynamic analysis of fluid saturated porous media. *Acta Geotechnica,* 7(4):297-311.

McKenna, F. and Fenves, G.L. (2001). *The OpenSees Command Language Manual, Version 1.2.* Pacific Engineering Research Center, University of California, Berkeley.

Muir Wood, D. (2000). The role of models in civil engineering. *Constitutive modelling of granular materials* (Kolymbas ed.), Springer-Verlag Berlin Heidelberg, 37-55.

Oberkampft, W.L., Trucano, T.G., and Hirsch, C. (2003). Verification, validation, and predictive capability in computational engineering and physics. *Sand Report SAND2003-3769*. Sandia National Laboratories, Albuquerque, New Mexico, USA.

OYO Corporation. (2014). *Report of Soil Investigation – Sendai District and Onahama District*.

Richart, F.E., Jr., Hall, J.R., and Woods, R.D. (1970). Vibration of soils and foundations. *International Series in Theoretical and Applied Mechanics,* Prentice-Hall, Englewood Cliffs, NJ, USA.

Roten, D., Fah, D., and Bonilla, L.F. (2013). High-frequency ground motion amplification during the 2011 Tohoku earthquake explained by soil dilatancy. *Geophysical Journal International,* 193(2):898-904.

Rowe, P.W. (1962). The stress-dilatancy relation for static equilibrium of an assembly of particles in contact. *Proceedings of the Royal Society of London, Series A,* 269:500-527.

Schnabel, P. B., Lysmer, J., and H. B. Seed. (1972). SHAKE–A computer program for response analysis of horizontally layered sites. Report No. EERC 72-12. University of California, Berkeley.

Schofield, A.N. and Wroth, C.P. (1968). *Critical State Soil Mechanics.* McGraw-Hill, New York, New York, USA.

Seed, H.B. and Idriss, I.M. (1970). Soil Moduli and Damping Factors for Dynamic Response Analyses, *Report No. EERC-70-10*, Earthquake Engineering Research Center, University of California, Berkeley.

Seismosoft. 2013. *Seismosignal*. Version 5.1.2.

Taiebat, M., 2008. *Advanced elastic-plastic constitutive and numerical modeling in geomechanics*. Ph.D. Dissertation, Department of Civil and Environmental Engineering, University of California, Davis.

Taiebat, M. and Dafalias, Y.F. (2008). SANISAND: simple anisotropic sand plasticity model. *International Journal of Numerical and Analytical Methods in Geomechanics,* 32(8):915-948.

Taiebat, M., Jeremic, B., Dafalias, Y.F., and Kaynia, A.M., and Cheng, Z. (2010). Propagation of seismic waves through liquefied soils. *Soil Dynamics and Earthquake Engineering,* 30(4):236-257.

Terzaghi, K. and Peck, R.B. (1967). *Soil Mechanics in Engineering Practice.* 2nd Ed, John Wiley and Sons, New York, New York, USA.

Tasiopoulou, P., Taiebat, M., Tafazzoli, N., and Jeremic B. (2015). Solution verification procedures for modeling and simulation of fully coupled porous media: static and dynamic behaviour. *Coupled Systems Mechanics,* 4(1):67-98.

Yamazaki, F., Towhata, I., and Ishihara, K. (1985). Numerical model for liquefaction problem under multi-directional shearing on a horizontal plane. *Proceedings of the Fifth International Conference on Numerical Methods in Geomechanics,* 399-406.

Zienkiewicz, O.C. and Shiomi, T. (1984). Dynamic behaviour of saturated porous media; the generalized Biot formulation and its numerical solution. *International Journal of Numerical Methods in Engineering,* 8(1):71-96.